

# Stability assessment of degrading permafrost rock slopes based on a temperature-dependent coupled thermo-mechanical model to assess the stability of degrading permafrost rock slopes

Philipp Mamot, Samuel Weber, Saskia Eppinger, and Michael Krautblatter

5 Chair of Landslide Research, Technical University of Munich, 80333, Germany

*Correspondence to:* Philipp Mamot (Philipp.mamot@tum.de)

**Abstract.** In the last two decades, permafrost degradation has been observed to be a major driver of enhanced rock slope instability and associated hazards in high mountains. While the thermal regime of permafrost degradation in high mountains ~~has already been intensively investigated~~ is addressed in several modelling approaches, ~~the no~~ mechanical ~~models have been~~ developed which thoroughly explain rock slope destabilisation controls in degrading permafrost ~~consequences on rock slope stability have so far not been reproduced in numerical models.~~ Meanwhile, recent ~~laboratory studies and conceptual models argue that warming and thawing decrease rock and discontinuity strength and promote deformations~~ show that degrading permafrost affects both, rock and ice-mechanical strength parameters as well as the strength of rock-ice interfaces.

10

This study presents the first general approach for a temperature-dependent numerical stability model that simulates the mechanical response of a warming and thawing permafrost rock slope. The proposed procedure is ~~applied to~~ exemplified with a rockslide at the permafrost-affected Zugspitze summit crest. Laboratory tests on frozen and unfrozen rock joint and intact rock properties provide material parameters for ~~the~~ discontinuum models developed with the Universal Distinct Element Code (UDEC). Geophysical and geotechnical field surveys ~~deliver-reveal~~ information on ~~the~~ permafrost distribution and ~~the~~ fracture network.

15

~~This model can~~ model demonstrates ~~that-how~~ warming decreases rock slope stability to a critical level, ~~while and why~~ thawing initiates failure. A ~~generalised~~ sensitivity analysis of the model with a simplified geometry and warming trajectory below 0 °C shows that progressive warming close to the melting point initiates instability above a critical slope angle of 50–62°, depending on the orientation of the fracture network. The increase in displacements intensifies for warming steps closer to zero degree. The simplified and generalised model can be applied to permafrost rock slopes (i) which warm above -4 °C, (ii), with ice-filled joints, (iii) with fractured limestone or probably most of the rock types relevant for permafrost rock slope failure, (iv) with a wide range of slope angles (30–70°) and orientations of the fracture network (consisting of three joint sets). ~~The presented model is the first~~ Here we present a benchmark model ~~one~~ capable of assessing the future destabilisation of degrading permafrost rock slopes.

20

25

## 1 Introduction

- 30 Rock slope failures in high mountain areas endanger human lives, settlements and infrastructure. The stability of alpine rock slopes can be considerably affected by the climate-induced degradation of bedrock permafrost (Fischer et al., 2006; Gruber et al., 2004; Gruber and Haerberli, 2007; Raveland and Deline, 2015). ~~In particular, the~~ Best empirical trends are provided by the well-monitored rock slope failures in the Mont Blanc Massif that have been linked to the degradation of bedrock permafrost and ice-filled joints (Raveland et al., 2010; Raveland and Deline, 2008; Raveland and Deline, 2011).
- 35 Mountain permafrost warmed globally by 0.19 °C between 2007 and 2016 (Biskaborn et al., 2019). Simulations of long-term permafrost evolution in Swiss, German or Norwegian mountain ranges show an overall warming of permafrost and thaw layer deepening up to the end of the century (Galleman et al., 2017; Hipp et al., 2012; Marmy et al., 2016). Rock slope failures influenced by permafrost degradation are expected to become more frequent as a result of the warming climate (Gobiet et al., 2014; Huggel et al., 2012).
- 40 ~~Failure tends to occur preferentially along~~ Most rock slope failures develop along discontinuities, ~~as they are planes of weakness in the much stronger, intact rock~~ whose patterns predetermine potential critical paths of failures (Wyllie, 2018). Fractures and fractured zones in mountain bedrock permafrost usually contain massive ice to depths of several tens of metres and more (Deline et al., 2015; Gruber and Haerberli, 2007). The majority of failure events in permafrost-affected rock exposed ice-filled joints as potential shear and detachment planes at different volumetric scales all over the world: ~~Some~~ The most
- 45 prominent examples are for instance, the 2003 Matterhorn block fall (0.002 Mio m<sup>3</sup>; Weber et al., 2017), the 2014 Piz Kesch rock slope failure (0.15 Mio m<sup>3</sup>; Phillips et al., 2017) and the 2017 Pizzo Cengalo failure with 8 fatalities (3–4 Mio m<sup>3</sup>; Walter et al., 2020) in Switzerland, the 1987 Val Pola debris avalanche in the Italian Alps (33 Mio m<sup>3</sup>; Dramis et al., 1995), the 2005 Mt. Steller rock-ice avalanche in Alaska (40–60 Mio m<sup>3</sup>; Huggel et al., 2010) and the 2002 Kolka/Karmadon rock-ice avalanche with 140 fatalities in the Russian Caucasus (100 Mio m<sup>3</sup>; Huggel et al., 2005).
- 50 The warming of permafrost in rock slopes ~~can reduce~~ reduces the shear resistance along rock joints by (i) reducing the fracture toughness of cohesive rock bridges, (ii) by lowering the friction along rock-rock contacts, (iii) by altering the creep of ice infillings and (iv) by reducing the fracture toughness of ice fillings and of rock-ice contacts (Krautblatter et al., 2013). Ice fillings contribute to higher rock joint shear strengths in terms of interlocking and adhesion along the rock-ice interface and ~~can~~ increase the stability of a rock slope. ~~This effect is reduced, or even lost, when the~~ The strength of ice in fractures decreases
- 55 when the temperature approaches the melting point (Davies et al., 2001; Gruber and Haerberli, 2007; Mamot et al., 2018). ~~Several So far, a huge number of~~ laboratory test series ~~have been performed on the~~ demonstrate the influence of warming or thawing on rock-ice-mechanical properties ~~to better estimate the consequent effect on rock slope stability: T~~ he ductile temperature- and stress-dependent creep of ice and ice-rich soils ~~has~~ ve been investigated by Arenson and Springman (2005) and Sanderson (1988). Whilst the ~~effect of~~ brittle failure and creep of ice-filled rock joints have been observed by Davies et al. (2000) ~~and~~ Günzel (2008), ~~and~~ Mamot et al. (2018), ~~proposed a new failure criterion model that demonstrates the loss of~~ ice friction and cohesion in rock fractures dependent on normal stress and temperature. ~~the~~ The mechanics of frozen and
- 60

unfrozen intact rock have been studied by Dwivedi et al. (2000), Inada and Yokota (1984), Kodama et al. (2013) and Mellor (1973). The friction along frozen and unfrozen rock joints was measured by Krautblatter et al. (2013). ~~Table 1~~ ~~Table 1~~ ~~summarises the~~ -temperature-dependent strength reduction ~~was able to be demonstrated~~ for all ~~these~~ ~~these~~ investigated mechanical parameters ~~(Table 1)~~.

65

**Table 1: A systematic survey of previous laboratory studies on the thawing-dependent mechanical strength reduction of rock and rock joint parameters.**

Mechanical parameter	Decrease due to warming		Temperature range tested [°C]	Type of rock / Normal stress	Reference
	% °C <sup>-1</sup>	absolute			
<b>Uniaxial compressive strength [MPa]</b>					
rock	1.5	200 to 170	-10 to 0	granite	Mellor (1973)
	4.7	95 to 50		sandstone	
	5	70 to 35		limestone	
	2	45 to 30	-20 to -5	tuff and andesite	Kodama et al. (2013)
	0.6	220 to 165	-40 to 0	granite	Inada and Yokota (1984)
polycrystalline ice	0.9	200 to 130	-40 to 0	andesite	Inada and Yokota (1984) Schulson and Duval (2009) Butkovitch (1954)
	1.5	6 to 1.5	-50 to 0	--	
	1.7	17 to 3	-50 to 0	--	
	5	4 to 2	-10 to 0	--	
<b>Uniaxial tensile strength [MPa]</b>					
rock	1.7	12 to 10	-10 to 0	granite	Mellor (1973)
	6.7	12 to 4		sandstone	
	6.7	12 to 4		limestone	
	4	5.5 to 2.5	-20 to -5	tuff and andesite	Kodama et al. (2013)
	1.1	14 to 10	-20 to 0	granodiorite	Glamheden (2001)
	0.6	12 to 9	-40 to 0	granite	Inada and Yokota (1984)
	1.1	20 to 11.5	-40 to 0	andesite	Inada and Yokota (1984) Butkovitch (1954)
polycrystalline ice	0.9	2.5 to 1.4	-50 to 0	--	
	1.3	1.5 to 1.3	-10 to 0	--	
<b>Young's modulus [GPa]</b>					
rock	0.5	42 to 39	-15 to 0	granodiorite	Glamheden (2001)
<b>Poisson's ratio</b>					
rock	0.7	0.27 to 0.24	-15 to 0	granodiorite	Glamheden (2001)
<b>Fracture toughness [MPa m<sup>0.5</sup>]</b>					
rock bridges	0.8	1.2 to 0.8	-10 to 30	limestone	Dwivedi et al. (2000)
	0.9	0.4 to 0.2		sandstone	
	0.02	1.5 to 1.5		basalt	
	0.2	1.6 to 1.4		dolerite	
polycrystalline ice	0.6	0.1 to 0.08	-50 to -2	--	Schulson and Duval (2009)
<b>P-wave velocity [km s<sup>-1</sup>]<sup>a</sup></b>					
rock	2.8	6.4 to 3.7	-15 to 0	limestone <sup>b</sup>	Draebing and Krautblatter (2012)
	0.8	6.1 to 5.4		gneiss <sup>b</sup>	
	1	6.1 to 5.2		granodiorit <sup>b</sup>	



Joint shear strength [MPa]					
concrete-ice	18.1	0.4 to 0.1	-5 to -0.5	100 kPa	Davies et al. (2000)
	16	0.8 to 0.2		1400 kPa	
	31	0.5 to 0.2	-2.5 to 0	140 kPa	Krautblatter et al. (2013)
	24	0.6 to 0.3		500 kPa	
ice-steel-ice	10.2	1.1 to 0.2	-10 to -2	--	Jellinek (1959)
rock-ice-rock	7.4	1.0 to 0.3	-10 to -0.5	limestone, 100 kPa	Mamot et al. (2018)
	8.2	1.4 to 0.3		limestone, 200 kPa	
	6.7	1.4 to 0.5		limestone, 400 kPa	
	17.2	1.0 to 0.4	-4 to -0.5	limestone, 800 kPa	
Joint friction angle [°]					
rock-rock	0.4	43.1 to 38.7	-4.5 to 22	dolomite	Krautblatter et al. (2013)
	0.6	35.5 to 30		limestone	
rock-ice-rock	10	64.5 to 27.7	-8 to -0.5	limestone, 100-400 kPa	Mamot et al. (2018)
	17	30.5 to 13.5	-4 to -0.5	limestone, 100-800 kPa	
	4	47.7 to 13.5	-18.5 to -0.5	granite	Barnes et al. (1971)
Joint cohesion [MPa]					
rock-ice-rock	11.5	0.6 to 0.1	-8 to -0.5	limestone, 100-400 kPa	Mamot et al. (2018)
	21.2	0.7 to 0.2	-4 to -0.5	limestone, 100-800 kPa	

**Note:** <sup>a</sup>The P-wave velocity of rock correlates highly to Mode I fracture toughness which correlates closely to Mode II fracture toughness (Chang et al., 2002). <sup>b</sup>P-wave velocities are parallel to cleavage/bedding.

70

The necessity to better link permafrost degradation and rock slope stability has been stated several times (Etzelmüller, 2013; Harris et al., 2009; Krautblatter et al., 2012). ~~To our knowledge,~~ ~~the~~ attempt to study the effect of warming or thawing on the mechanical response of a rock slope has been realised only once: ~~by~~ Davies et al. (2001). ~~For this, the authors~~ simulated the warming of a ~~simplified, full rock slope self-constructed in a~~ laboratory centrifuge model ~~representing a simplified, full rock slope, and estimated~~ Factors ~~factors~~ of safety ~~were estimated~~ for unfrozen and ice-filled joints at temperatures close to the melting point. ~~Included temperature dependent using~~ mechanical properties ~~were derived~~ from ~~prior~~ laboratory shear tests ~~by Davies et al. by~~ (Davies et al. (2000)).

75

~~By now, a~~ Numerical ~~modelling is an~~ ~~common and~~ established method to (i) mechanically assess rock slope stability and characterise failure, deformation and influencing factors (Stead et al., 2006), and (ii) thermally analyse the spatial distribution and evolution of permafrost in a mountain or rock slope (Haberkorn et al., 2017; Moore et al., 2011; Myhra et al., 2017; Noetzli and Gruber, 2009). However, no ~~temperature-dependent thermo-mechanically combined~~ numerical model has been developed yet which ~~considers~~ ~~implements~~ the ~~warming and thawing dependent~~ deformation and strength reduction of permafrost bedrock and ice-filled discontinuities ~~upon warming or thawing~~. ~~Nevertheless,~~ ~~to~~ anticipate failure in a warming climate, we need to understand how rock-ice mechanical components control rock slope destabilisation and how failure ~~close to melting, and at thawing, in warming permafrost rocks~~ can be mechanically expressed in models.

80

85

Discontinuum discrete-element codes simulate the deformation behaviour of fractured rock masses and consider the influence of jointing (Stead et al., 2006). Among these codes, UDEC (Universal Distinct Element Code) is one of among the most-used modelling tools used for distinct-element modelling of jointed and blocky material in 2D, ~~has so far been and has been~~ applied to ~~a number of numerous published~~ stability analyses ~~for in~~ unfrozen rock slopes (Bhasin and Kaynia, 2004; Fischer et al., 2010; Gischig et al., 2011a, 2011b, 2011c; Glamheden and Lindblom, 2002; Kveldsvik et al., 2008; Welkner et al., 2010).

In this paper, we present the first numerical ~~discontinuum~~ model that calculates the influence of warming and thawing of frozen rock and rock joints on the mechanical strength and deformation behaviour of ~~an entire~~ rock slope. The proposed model is applied to a rockslide at the permafrost-affected Zugspitze summit which is one of the highest peaks of the Northern Calcareous Alps, located in the Eastern Alps. In this context, we address the following research questions:

- 1) How can mechanical and thermal data from the field and from the laboratory be combined to develop a ~~coupled~~ numerical stability model for a warming and thawing permafrost rock slope?
- 2) Is the numerical stability model of the Zugspitze summit crest capable of simulating the warming-dependent changes in stability observed at the laboratory scale?
- 3) How is the generic stability of a warming permafrost rock slope dependent on the slope angle and the orientation of the fracture network?

~~A slowly moving rockslide at the Zugspitze summit crest (2900 m a.s.l.), Germany, with presumably degrading permafrost bedrock was chosen as a real world example for rock slope instability (Mamot et al., 2018). Rock specimens were collected close by the rockslide and used for a large number of mechanical laboratory tests on a broad spectrum of frozen and unfrozen intact rock and rock joint properties. Intact rock properties were converted to rock mass characteristics using internationally standardised mathematical equations. Electrical resistivity tomography (ERT) was applied to identify current frozen and unfrozen slope sections. These were implemented in the numerical model to spatially assign frozen or unfrozen rock mass and joint parameters to the corresponding model sections and to derive a rough spatial warming pattern.~~

~~Considering the numerous laboratory-based observations of the strength reduction of rock ice mechanical properties at warming/thawing (Table 1), we expect to model a strong effect on the slope stability. For this, we set up a discontinuum model in 2D with UDEC 7. In a first step, we modelled the numerical impact of warming and thawing on the stability of the Zugspitze summit crest with ice filled joints. In a second step, we applied the same model to a frozen rock slope with simplified geometry to study the numerical impact of rising subzero temperature on the rock slope stability for varying slope angles and orientations of the joint set configuration.~~

## 2 A general approach applied to the Zugspitze summit crest~~general thermo-mechanically coupled stability model~~

A

~~In this study, a~~ slowly moving rockslide at the Zugspitze summit crest (2900 m a.s.l.), Germany, with extensive monitoring data on kinematics and degrading permafrost bedrock was chosen to develop a close to nature rock slope instability model for degrading permafrost rock slopes (Fig. 1; see also Mamot et al., 2018). Homogeneous lithology, well known permafrost degradation history for the Zugspitze summit area and the accessibility to an ice-filled rock sliding surface (Fig. 1c) made it an ideal benchmark for the mechanical model development. ~~The model profile and the characteristics of the fracture network for the numerical model were taken from the study site.~~ Rock specimens collected closeby to the rockslide were ~~a~~ used for a unique set of ~~n~~ mechanical laboratory tests on a broad spectrum of frozen and unfrozen intact rock and rock joint properties. Intact rock properties were converted to rock mass characteristics using internationally standardised mathematical equations. Electrical resistivity tomography (ERT) was applied to identify current frozen and unfrozen slope sections. These were implemented in the numerical model to spatially assign frozen or unfrozen rock mass and joint parameters to the corresponding model sections and to derive a rough spatial warming pattern. Considering the numerous laboratory-based observations of the strength reduction of rock-ice-mechanical properties at warming/thawing (Table 1), we expect to model a ~~significant~~ ~~strong~~ effect on the slope stability. For this, we set up a discontinuum model in 2D with UDEC 7. In a first step, we modelled the numerical impact of warming and thawing on the stability of the Zugspitze summit crest with ice-filled joints. In a second step, we applied the same model to a frozen rock slope with simplified geometry to study the numerical impact of rising subzero temperature on the rock slope stability for varying slope angles and orientations of the joint set configuration.

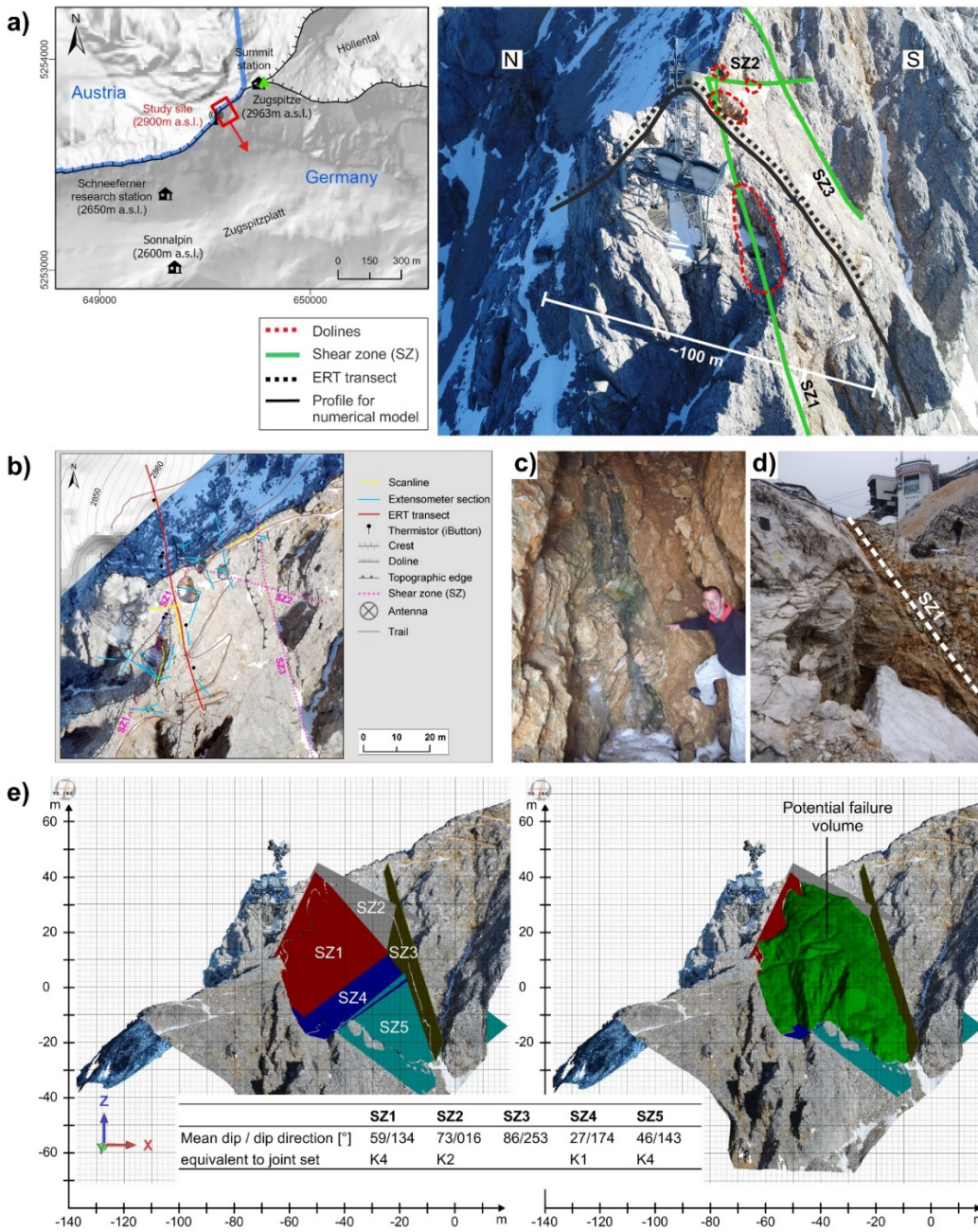


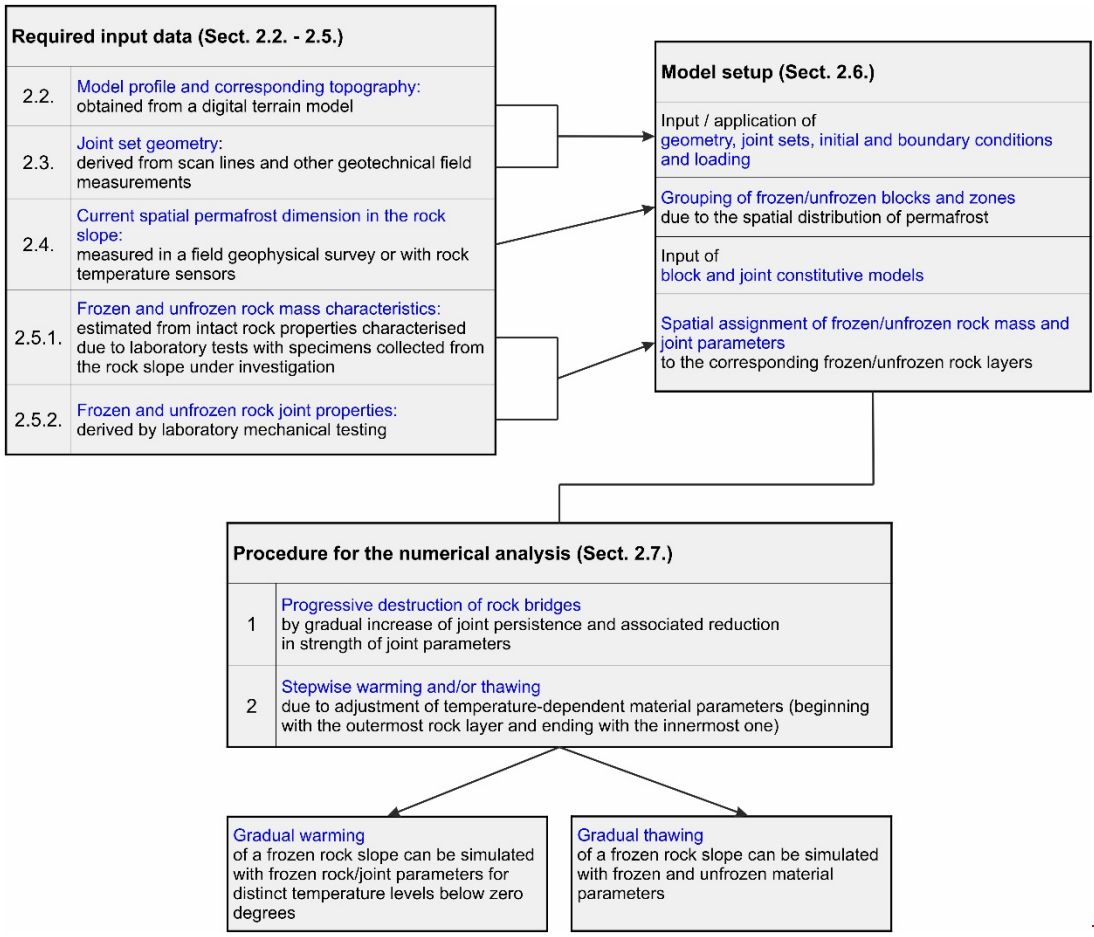
**Figure 1:** (a) Left: Location of the study site (red box) in the Zugspitze summit area, ca. 60 m below the peak (2963 m a.s.l.). The red arrow points to the sliding direction of the unstable rock mass. The hillshade is calculated from a digital elevation model with a cell size of 10 m for Austria and 5 m for Germany (Bavarian Agency for Digitisation, High-Speed Internet and Surveying, 2006). Coordinates are given in ETRS 1989 UTM Zone 32N. Right: View from above down on the study site, including dolines, the assumed main shear zones of the upper part of the rockslide, the profile used for the numerical model and the transect for the electrical resistivity survey. (b) Network of geophysical and geotechnical measurements at the study site including reference to geomorphologic and anthropogenic features. The orthofoto is derived by UAV-based photogrammetry. (c) and (d) Shear zone SZ1 filled with ice or

with fine material, exposed at the inner wall of dolines. (e) Intersecting main shear zones which delineate the unstable rock mass at the south-face of the Zugspitze summit crest: without (left) and with the potential failure volume (right).

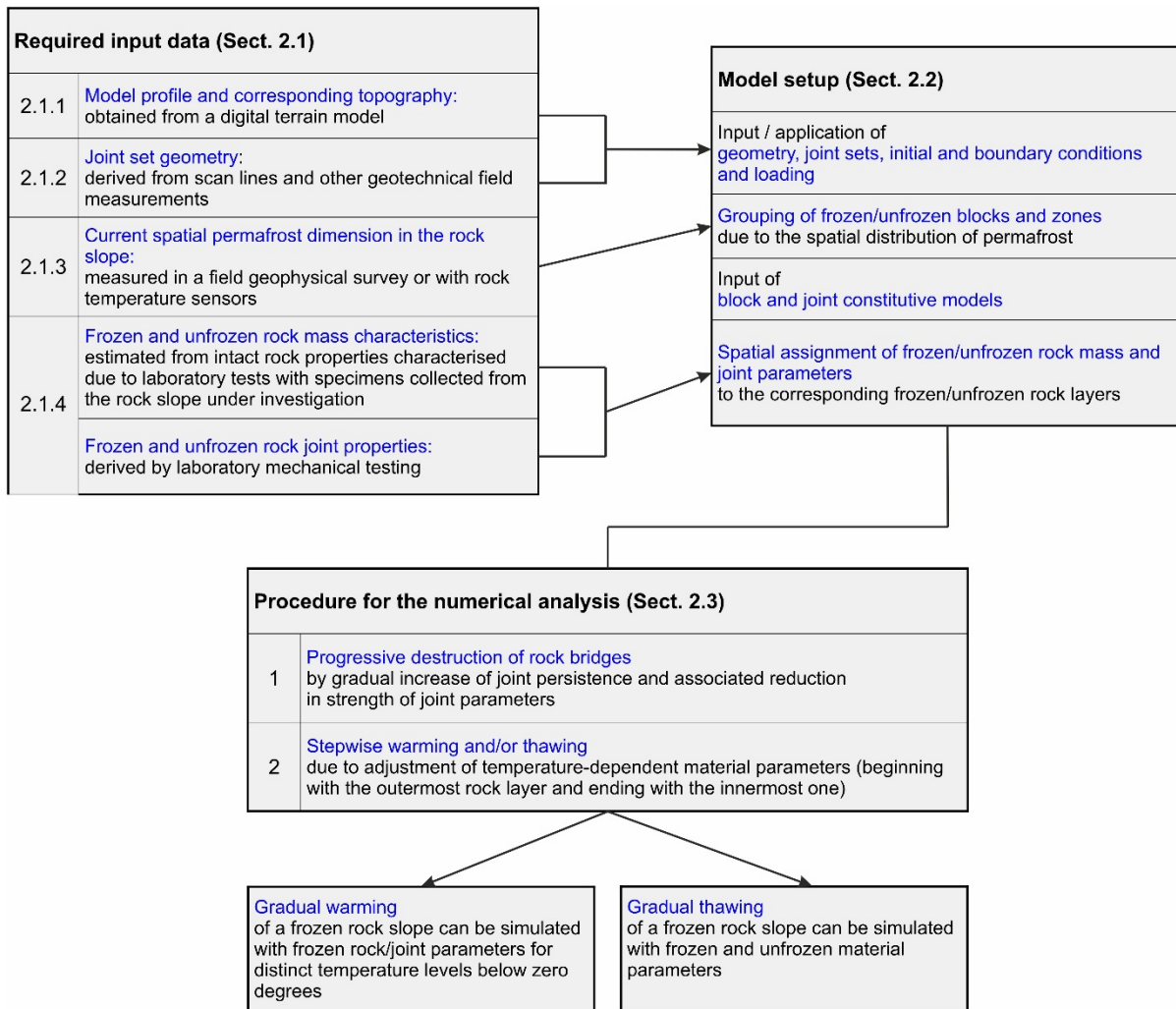
145

~~We propose the following~~[Fig. 21](#) demonstrates a general procedure to develop a numerical discontinuum model to calculate the influence of warming and thawing on the mechanical strength and deformation behaviour of a (partially) frozen rock slope (~~Fig. 1~~). Here, we present one exemplary way how to apply the set-up of the model and the modelling procedure to a real-world example of alpine rock slope instability potentially affected by permafrost degradation. For instance, the detection of bedrock permafrost can also be performed by other techniques like seismic refraction tomography; similarly, the conversion of the intact rock properties to those of the rock mass can also be done by the Q-value (and not by the GSI scheme, as presented in this article).

150







155

**Figure 2: General procedure for a ~~temperature-dependent thermo-mechanically combined~~ discontinuum model for the stability of a warming or thawing permafrost rock slope. The procedure is embedded as methodological approach in this manuscript and, hence, is linked to specific sections.**

~~und eine Positionskarte 1e~~

160

### 2.1 Application to the Zugspitze summit crest

~~(2900 m a.s.l., Fig. 2) in Germany. The presented modelling approach (Fig. 1) was applied to a real world example of alpine rock slope instability potentially affected by permafrost degradation: The topography, model profile, joint set geometry, rock samples and permafrost distribution for the numerical model were taken from a shallow rockslide at the south face of the Zugspitze summit crest (2900 m a.s.l., Fig. 2) in Germany. The unstable rock mass was assessed to a volume of approximately  $2.9 \times 10^4 \text{ m}^3$  (Fig. S2). Measured fracture displacements between 2013 and 2019 show that the rock mass creeps slowly at an~~

165

average of  $2.1 \text{ mm yr}^{-1}$ , with deformation rates reducing by 84 % when comparing summer months (June to September) with the remaining seasons (Fig. S5). Details on the volume estimation and the measurement of the crack displacements are given in the supporting material.

170 The Zugspitze is one of the highest peaks of the Northern Calcareous Alps, located in the Eastern Alps. The summit crest consists of Triassic Wetterstein limestone which has a thickness of 1000 m and constitutes the majority of the Zugspitze massif and the Wetterstein mountains (Galleman et al., 2017; Miller, 1962). The limestone is massy, fine grained and dolomised and shows little heterogeneity in terms of lithological properties (Krautblatter et al., 2010). Its porosity ranges between 1.9 % (Draebing and Krautblatter, 2012) and 4.4 % (Krautblatter et al., 2010).

## 175 **2.12 Characterisation of the mechanical and thermal setting**

### **2.1.1 Model profile**

The numerical model was set up in 2D and, thus, required a cross section of the summit crest. This profile covers a distance of 100 m, it runs from the north-face, across the crestline, to the south-face, and it crosses one of the main shear zones of the rockslide (Fig. [1a](#), [Fig. 1b2](#)).

180



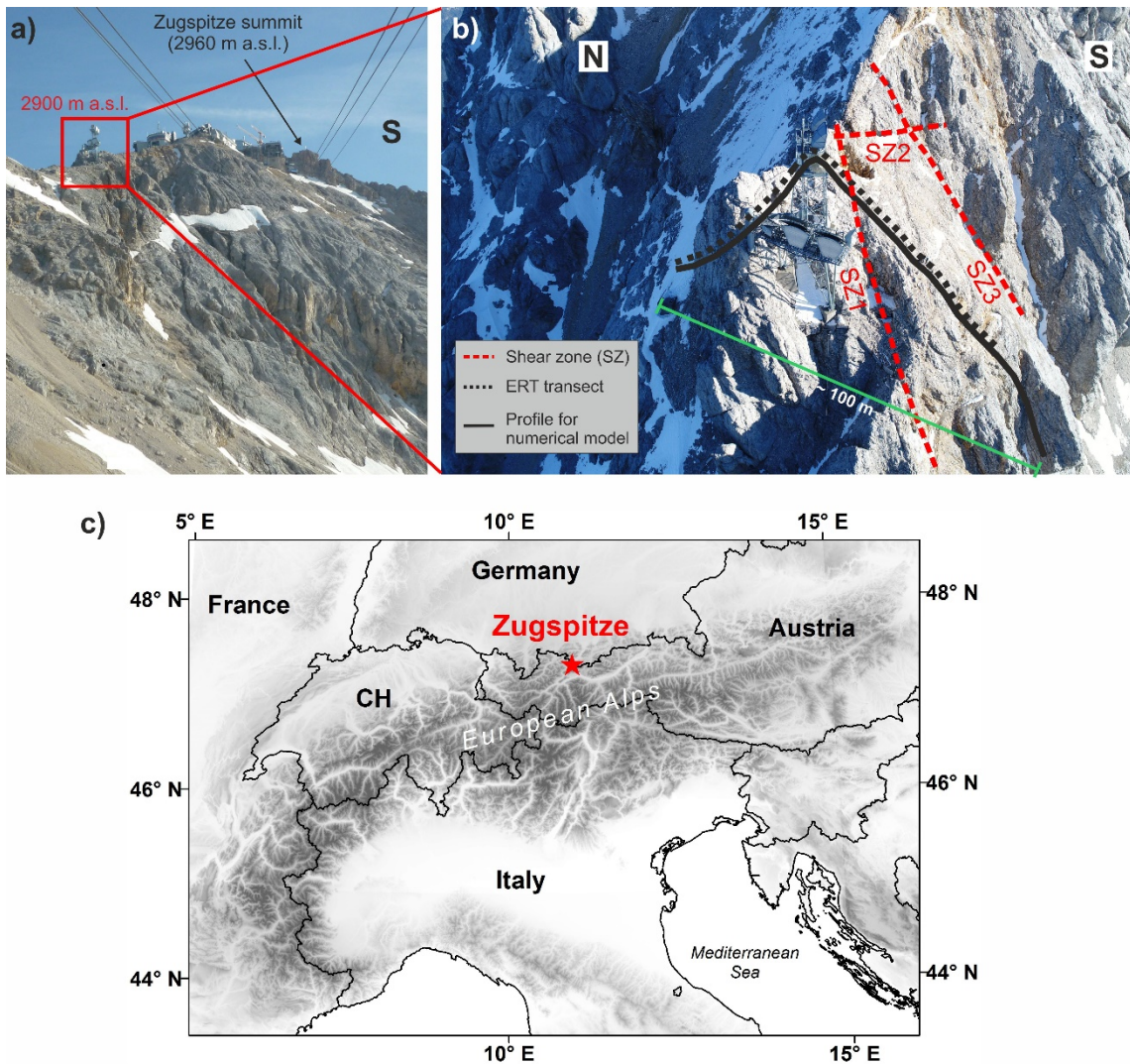


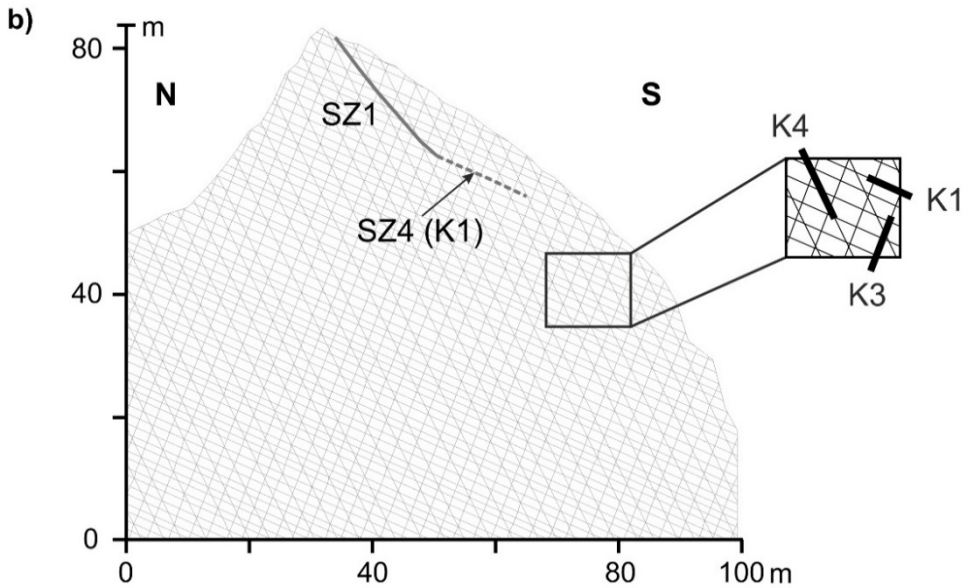
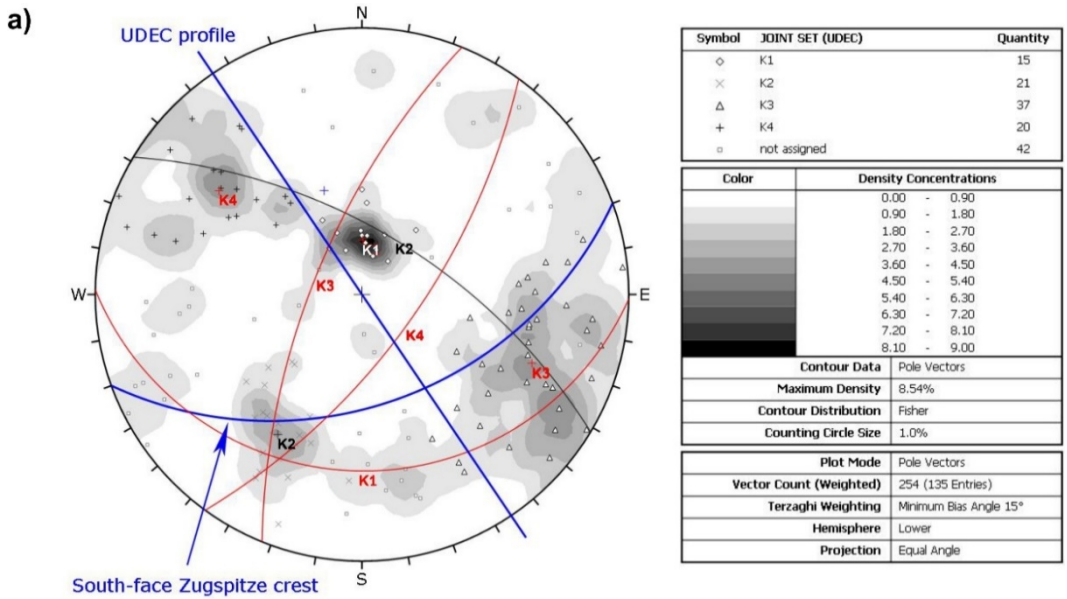
**Figure 2:** (a) Location of the Zugspitze in the context of the European Alps. The digital elevation model was developed with SRTM data from CGIAR-CSI and has a cell size of 90 m (Jarvis et al., 2008). View on the south face of the Zugspitze summit crest, Germany. The study site is located 60 m below the peak (2960 m a.s.l.), highlighted by the red box. (b) View from above down on the study site, including the assumed main shear zones of the upper part of the rockslide (red dashed lines), the profile used for the numerical model (black line) and the transect for the electrical resistivity survey (black dashed line). (c) Location of the Zugspitze in the context of the European Alps. The digital elevation model was developed with SRTM data from CGIAR-CSI and has a cell size of 90 m (Jarvis et al., 2008).

185

### 190 2.1.23 Rock joint geometry and kinematic analysis

Four discontinuity sets (K1, K2, K3, K4) were identified due to scan lines and field mapping (Fig. 3a). The trend of the profile for the mechanical model strikes at  $146^\circ$  for the UDEC mechanical model which is in the direction of the assumed

195 movement was chosen to strike at  $146^\circ$ , which is more or less and follows the dip-perpendicular to the estimated orientation of the southern slope face (45/160). Hence, K2 (33/063) had to be excluded from the numerical analysis as the dip direction deviated by  $66.5^\circ$  from the trend of the model profile. The remaining joint sets deviated by  $20\text{--}33^\circ$  and were implemented in the model as the standard deviations of their dip directions ranged between  $5\text{--}20^\circ$ , falling within the tolerable range of  $30^\circ$  deviation (Table 2). Joint set K1 represents the bedding planes and daylight in the south-face at an angle of  $24^\circ$  (Fig. 3b).



205

Figure 3: (a) Orientations of field-measured discontinuities in a stereographic projection, calculated with DIPS 7.0 (Rocscience). ~~The red great circles with red labels represent the joint sets (K) that were selected as input for implemented in the numerical model. The contours depict the Fisher concentrations (density) of the poles, and K is the Joint set.~~ (b) Fracture network, extent and topography of the 2D numerical model. Shear zones (SZ) included in the model are marked with thick grey lines. The dashed line represents the ~~uncertain assumed course prolongation~~ of the potential failure plane ~~at in the~~ lower slope sections.

**Table 2: Mapped geometric discontinuity characteristics. Standard deviations are only given for measured parameters. K1-4 = Joint sets, SZ = Shear zone. Geotechnical characteristics of the joint sets.**

Geometric parameters	K1	K3	K4	SZ1 (K4)	Input for numerical model
Dip/dip direction [°]	24/175	69/293	66/126	63/130	x
Deviation of dip direction from trend of model profile [°]	29.3	33.3	20.4	16.0	x (as below 30°, considering the standard deviation)
Standard deviation of dip direction [°]	20.2	132.6	4.5	--	x
Standard deviation of dip [°]	32.9	43.8	87.5	--	
Spacing [m]	0.27 ± 0.3	0.54 ± 0.6	0.59 ± 0.7	--	x
Aperture [mm]	7.0 ± 17.1	2.9 ± 6.8	5.3 ± 8.1	270.0	
Joint frequency [F m <sup>-1</sup> ]	3.7	1.9	1.6	--	x (simplified representation)
Joint roughness coefficient JRC <sup>a</sup>	5.5 ± 1.8	8.6	--	4.4 ± 3.3	
Number of mapped joints	15	37	19	1	

**Note:** Standard deviations are only given for measured parameters. K1-K4 = Joint sets, SZ = Shear zone. <sup>a</sup>The JRC was measured along joints not included in the scanlines. Standard deviations are only given for measured parameters. K1-4 = Joint sets, SZ = Shear zone.

The possible failure mechanism and shear zones which delimit the currently observed unstable rock mass were assessed manually, and with a 3D point cloud of the Zugspitze summit crestline derived by UAV-based (Unmanned Aerial Vehicle) photogrammetry was performed at the Zugspitze summit crest to compute a 3D point cloud of the Zugspitze summit crestline (Fig. 1e), and with a kinematic analysis, providing information on the possible failure mechanism and shear zones which delimit the currently observed unstable rock mass. In addition, a simple kinematic analysis of a potential plane and wedge failure (Fig. S1, supplementary material). The latter was conducted with DIPS 7.0 (Rocscience) involving for the southern slope-face and along the main shear zones, which were identified due to field mapping and the preceding analysis of the point cloud. A detailed description of both methods is given in the (supplement Supplementary material Material). The instability is driven by a complex combination of a plane and a wedge failure (Fig. S2, Fig. S3). Though planar sliding is the dominant kinematic failure mode which affects the major left part of the unstable rock mass (Fig. 1a, Fig. 1e, Fig. S1), we assume that the instability is driven by a complex combination of both a plane and a wedge failure. The results showed that the most likely failure mechanism is a complex combination of a plane and a wedge failure (Fig. S2, Fig. S3). Planar sliding mainly occurs along shear zone SZ1, while wedge failure supports the displacement along SZ1/SZ3 including a tension crack SZ2 (Fig. 2e) in the upper part of the slope instability. planar sliding may occur along shear zone SZ1, while wedge failure supports the displacement along SZ1/SZ3 including a tension crack SZ2. In the upper part of the slope instability, wedge failure occurs along shear zones SZ1/SZ3 including a tension crack SZ2, while local planar sliding along shear zone SZ1 may support the displacement (Fig. 2cb). At lower slope sections two further shear zones (SZ4 and

230 ~~SZ5) were determined to form the assumed downslope boundary of the unstable rock mass in the lower slope sections. Here, wedge failure may occur along shear zone SZ3 and a stepped plane constituted of shear zones SZ4 and SZ5, while planar sliding along SZ4 or SZ5 potentially enhances the failure process. Planar sliding can occur along SZ4 and SZ5, while wedge failure potentially enhances the failure process along SZ3 and the planes SZ4 and SZ5.~~

235 ~~The gTThe transects for the gGeophysical measurementstransects and the numerical model profile for the numerical model run throughalong the stepped planar failure part of the unstable rock mass (shear zones SZ1, SZ4, SZ5; left part in Fig. 1e). Shear zone SZ1 (equivalent to K4) and shear zone SZ4 (corresponds to K1) were chosen to be included in the numerical model (Fig. 3b);~~

~~The results showed that the most likely failure mechanism is a complex combination of a plane and a wedge failure (Fig. S2, Fig. S3). In the upper part of the slope instability, wedge failure occurs along shear zones SZ1/SZ3 including a tension crack SZ2, while local planar sliding along shear zone SZ1 may support the displacement (Fig. 2b). At lower slope sections, two further shear zones (SZ4 and SZ5) were determined to form the assumed downslope boundary of the unstable rock mass (Fig. S2). Here, wedge failure may occur along shear zone SZ3 and a stepped plane constituted of shear zones SZ4 and SZ5, while planar sliding along SZ4 or SZ5 potentially enhances the failure process.~~

240 ~~To allow simplification and a representation in 2D, shear zone SZ1 (equivalent to K4) and shear zone SZ4 (corresponds to K1) were chosen to be included in the numerical model (Fig. 3b).~~ We assume the slope instability to be significantly dominated by shear zone SZ1. Observed maximum displacements along the upper part of SZ1 lie in the range of decimetres and point to a high level of joint persistence. Further, three carst dolines with a depth of several metres were mapped along SZ1 and at the intersection of shear zones SZ1 with SZ2 (Fig. 1a, Fig. S2S4). SZ1 ~~has a trace length of approximately 70 m, runs in a maximum depth of 10–15 m and dips to the southeast, and corresponds to joint set K4. According to geotechnical field mapping, it has a trace length of approximately 70 m and runs in a maximum depth of 10–15 m.~~ It is highly fractured and at some places it opens to a width ~~displays joint opening~~ of several decimetres, filled with fine material which ranges from clay- to gravel-size (Fig. 1d).

245 ~~The 3D point cloud analysis was used to assess the unstable rock mass at the south-face of the summit crest to a volume of approximately  $2.9 * 10^4 \text{ m}^3$  (Fig. 1e). Measured fracture displacements between 2013 and 2019 show that the rock mass creeps slowly at an average of  $2.1 \text{ mm yr}^{-1}$  (Fig. S3). Between October and May, deformation rates are 84 % lower than in the remaining summer months. Details on the volume estimation and the measurement of the crack displacements are given in the supporting material.~~

### **2.1.34 Spatial permafrost distribution ~~within the summit crest~~**

250 In the 1960s and 1990s, ~~the occurrence of~~ permafrost at the Zugspitze summit was ~~able to be confirmed byfound in~~ deep and permanently ice-filled fractures with a maximum aperture of 0.1 m (Körner and Ulrich, 1965; Ulrich and King, 1993). ~~The Zugspitze summit area is located at the lower permafrost extension limit.~~ Current borehole temperatures at the peak of the Zugspitze average ~~-1.3-1~~ °C within the permafrost core area (20–25 m away from the rock walls). At the margin to the active

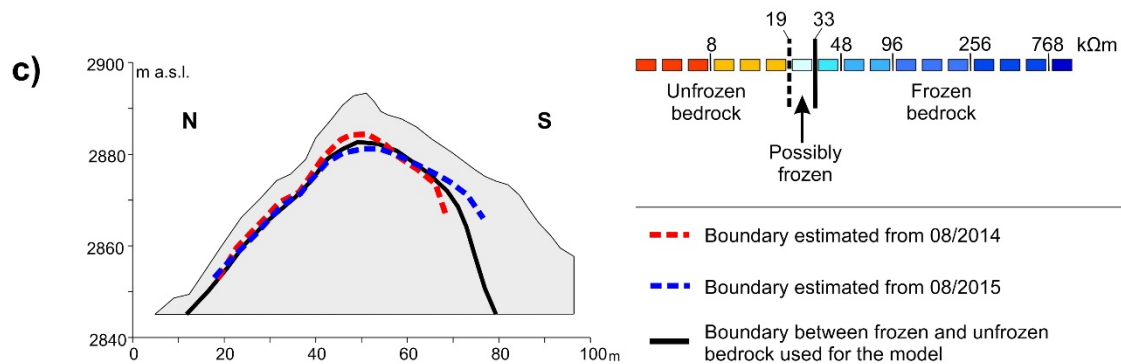
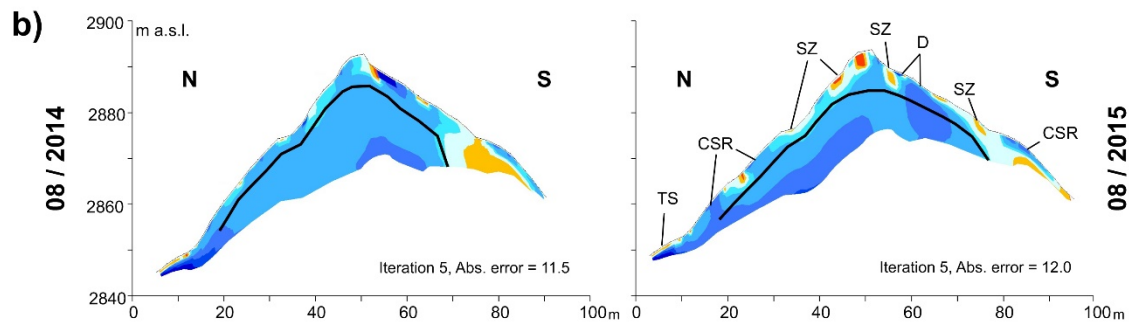
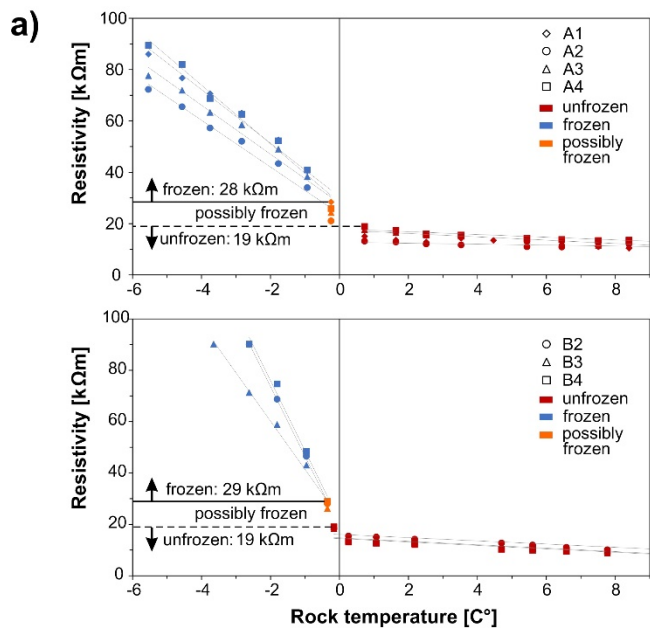


layer (ca. 5 m away from the north-face), the temperatures approach minima of -6 °C during winter (Böckli et al., 2011; Gallemann et al., 2017; Krautblatter et al., 2010; Noetzli et al., 2010). ~~The mean annual air temperature (MAAT) at the Zugspitze peak from 1991 to 2019 was 3.9 °C. It was 0.8–1.1 °C warmer than the three means of the prior 30-year reference periods between 1901 and 1990 (CDC FTP Server, Deutscher Wetterdienst). A model for the permafrost evolution at the Zugspitze peak by Gallemann et al. (2017) shows that between 1915 and 2015 the permafrost decreased by 2 m at the north-face and by 7 m at the south-face, with an increase in the permafrost temperature of approximately 1 °C.~~

~~To accurately assess the current distribution of permafrost along the model profile at the study site, we applied~~ laboratory-calibrated electrical resistivity tomography (ERT). ~~This technique has been used to~~ ~~is capable of~~ characterising and monitoring the spatial variability and evolution of mountain bedrock permafrost in steep rock walls (Keuschnig et al., 2017; Krautblatter et al., 2010; Murton et al., 2016). The outlined procedure of the measuring setup in the field was similarly applied to the Zugspitze summit crest. ~~to accurately assess the distribution of permafrost along the model profile (Fig. 2b).~~ Two surveys were conducted at the end of August 2014 and 2015, ~~which corresponds to~~ ~~when~~ the time the active layer ~~at the Zugspitze peak usually~~ reaches ~~sd~~ the maximum ~~thickness extent~~ (Gallemann et al., 2017). Data processing and inversions were performed with Res2Dinv (~~see supplement material for measuring setup, data acquisition and analysis of the field surveys~~).

To assign the measured ERT of the summit crest to frozen or unfrozen slope sections, we used the ~~characteristic laboratory ER resistivity~~ of saturated frozen and unfrozen Wetterstein limestone ~~in the laboratory~~, defined (i) by Krautblatter et al. (2010) ~~based on one rock sample in the same lithology~~, and (ii) in the context of this study based on two rock blocks from the field site. For the laboratory tests, we followed the suggested procedure by Krautblatter et al. (2010), though limited to a single cooling and subsequent freezing trajectory of the samples from 10 down to -6 °C. ~~The (See supplement material provides additional information on the laboratory tests as well as on~~ ~~for the measuring setup, data acquisition and analysis of the field surveys).~~ ~~The rock samples (both with a size of 0.02 m<sup>3</sup>) were kept in a self-built, temperature-controlled cooling box for the duration of the tests. Rock temperature was measured simultaneous to resistivity with two Pt100 sensors (Greisinger GMH3750, with a 0.03 °C precision) inserted in the rock samples (Fig. 4a). Measurements were performed along 3–4 different Wenner arrays installed parallel to each other.~~

The laboratory ER clearly showed values lower than 19 kΩm for unfrozen rock and values higher than 28–29 kΩm for frozen rock (Fig. 4a–c). The equilibrium freezing point at -0.2 ~~or to~~ -0.4 °C is indicated by a 21 ~~or a~~ to 37-fold increase of the frozen temperature-resistivity gradient. This pattern of electrical resistivity versus rock temperature is similar to the one demonstrated by Krautblatter et al. (2010): here, the ER measures 30 ± 3 kΩm at the equilibrium freezing point (-0.5 °C). Overall, we defined ER-values lower than 19 kΩm and higher than 33 kΩm to be unfrozen or frozen, ~~respectively. The~~ ~~and~~ ~~the~~ range of values ~~lain~~ in between ~~was defined to be~~ ~~as~~ possibly frozen rock.



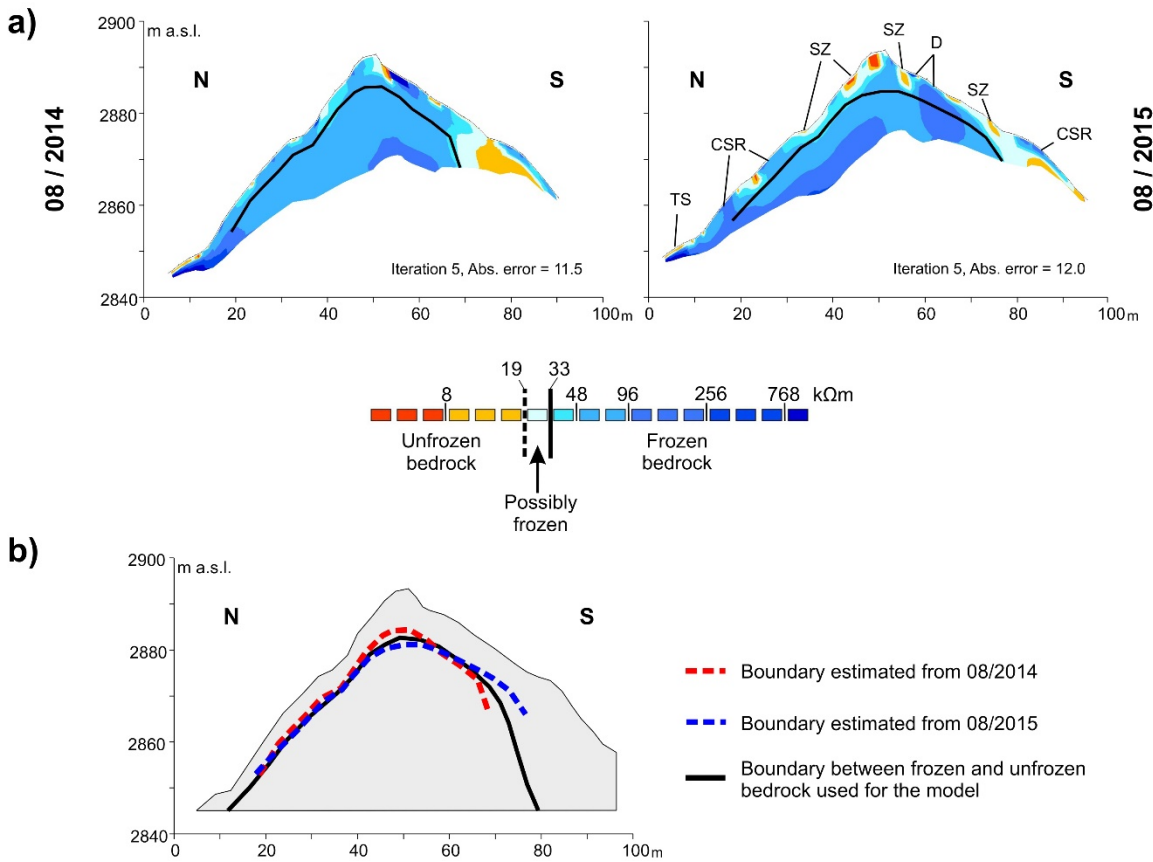


Figure 4: (a) Left: Laboratory-tested electrical resistivity of frozen and unfrozen Wetterstein limestone collected at the study site. Definition of frozen (blue symbols), unfrozen (red symbols) and possibly frozen (orange symbols) electrical resistivity based on the freezing-trajectories of two rock samples. Measurements were performed along different Wenner arrays (i.e., A1-A4 or B2-B4) installed parallel to each other. Right: Test setup in the laboratory cooling box. (b) Distribution of frozen and unfrozen bedrock in the Zugspitze summit crest derived from two ERT surveys in August 2014 and August 2015. TS = Talus slope. CSR = Compact solid unfrozen rock. SZ = Shear zone. D = Doline. The locations of these features are the same in the tomography of 2014. (c) Combination of the successive ERT campaigns used for the estimation of the current spatial extent of bedrock permafrost implemented in the numerical model (Fig. 5).

The ERT inversions results of 2014 and 2015 are interpreted as follows (Fig. 4b and Fig. 4c):

- The shallow rock layer is almost continuously unfrozen on both aspects of the crest. This assumption is confirmed by (i) borehole rock temperatures at the Zugspitze peak which show a 2–4 m thick active layer on the north-face (Gallemann et al., 2017), and (ii) thermistor-based rock temperatures measured along the ERT transect in a depth of 10–80 cm below the ground surface. The corresponding thermistors (specially modified iButtons in rods) show that the rock temperatures do not remain below zero degrees throughout the year and are positive at the moment of the ERT surveys (Fig. 1b, Fig. S4).



- ~~Due to this evidence, the current boundary to permafrost on the north-face and at the upper part of the south-face was set to a continuous depth of approximately 5 m (black line in Fig. 4b and Fig. 4c).~~

315 - ~~Most near-surface interstitial patches of resistivities  $\geq$  higher than 33 k $\Omega$ m do not represent frozen rock; instead, they point to relate to massive ice measured in the visible in the meter deep carst doline close to the crestline and surficial drying of rock usually, which is limited to the upper decimeter, or to sections of compact solid rock or to bad electrode-ground coupling (Hauck and Kneisel, 2008; Sass, 2005).~~

320 - ~~The assumption of the unfrozen near-surface rock layer is confirmed by thermistor-based rock temperatures measured in a depth of 10–80 cm below the ground surface at the same time as the ERT surveys. The corresponding thermistors (specially modified buttons in rods) were installed along the ERT transect and show that the rock temperatures do not remain below zero degrees throughout the year (Fig. S4, Fig. S4). Furthermore, borehole rock temperatures along the borehole at the Zugspitze peak show a 2–4 m thick active layer on the north face (Gallemann et al., 2017). Due to this evidence, the current boundary to permafrost on the north face and at the upper part of the south face was set to a continuous depth of approximately 5 m (black line in Fig. 4b). On the lower south-slope, the unfrozen bedrock becomes thicker with decreasing altitude and can be found down to a depth of 10 m and more indicated by resistivities  $< 19$  k $\Omega$ m.~~

325 - ~~Other individual patches of low electrical resistivity ( $< 19$  k $\Omega$ m) refer to major shear zones or to the highly porous talus slope below the northern rock wall. When fractures or the debris of the talus slope are filled with air or with unfrozen, saturated and fine material, the corresponding electrical resistivities are much lower than for ice fillings (Hauck and Kneisel, 2008; Supper et al., 2014). Zones of high conductivity can be promoted by precipitation or water from snow melt which easily infiltrate along unfrozen fine fillings or fractures. Unfrozen fine fillings permit water to infiltrate easily and can represent zones of high conductivity (Supper et al., 2014), particularly in the case of preceding precipitation or snow melt (Keuschnig et al., 2017). Having defined the boundaries between frozen and unfrozen slope sections~~

335 - ~~for T For two successive years 2014 and 2015, the resulting overall spatial extent of permafrost relates to the core of the crest and rock layers below 5 m at the north-face, while the layer of unfrozen bedrock at the south face becomes thicker with decreasing altitude (Fig. 4b).~~

-

## 2.1.45 Mechanical properties

340 ~~The Zugspitze summit crest consists of Triassic Wetterstein limestone which has a thickness of 1000 m and constitutes the majority of the Zugspitze massif and the Wetterstein mountains (Gallemann et al., 2017; Miller, 1962). The limestone is massy, fine-grained and dolomised and shows little heterogeneity in terms of lithological properties (Krautblatter et al., 2010). Its porosity ranges between 1.9 % (Draebing and Krautblatter, 2012) and 4.4 % (Krautblatter et al., 2010).~~

The distinct element method in UDEC model software enables to simulate the mechanical behaviour of a discontinuous medium: the assemblage of discrete rock blocks separated from each other by discontinuities. At slope scale, material properties of the rock mass instead of intact rock are needed. As such, the model requires material properties for both the rock blocks and discontinuities (Itasca Consulting Group, 2019). For stability analyses at the scale of a full rock slope, the appropriate rock strength to be used for model parameter input is that of the rock mass, and not of an intact rock specimen for laboratory tests. as discontinuities reduce rock mass strength and induce non-linearities and anisotropy in the stress-strain behaviour (Hoek et al., 2002; Wyllie, 2018). Hence, blocks and zones were allocated rock mass properties to account for the influence of heterogeneities, micro-fractures and other small discontinuities on the mechanical response of the bigger rock blocks. We extensively investigated frozen and unfrozen the rock and joint properties in the laboratory to assess the effect of thawing on the mechanical strength and deformability, and to determine the required material parameters for the model. we tested an extensive number of frozen and unfrozen rock and joint properties of the field site material in the laboratory. The All tests were performed with fully water saturated Wetterstein limestone samples collected at the study site. Frozen rock samples had a mean temperature of -5 °C, while unfrozen rock specimens were tested at room temperature (~22 °C). As we assume the rock mass of a real world rock slope to be usually saturated, the frozen and unfrozen rock samples were mostly tested in a fully saturated state. Detailed information on the preparation of the rock samples, the test setups and conditions can be looked up in the supporting material elements (see Sect. S6).

### **2.5.1 Frozen and unfrozen intact rock and rock mass**

The strength and deformability of the model blocks and zones within the blocks were represented by the Mohr-Coulomb plasticity constitutive model with a tension cut-off. At the slope scale, material properties of the rock mass instead of intact rock are needed as discontinuities reduce rock mass strength and induce non-linearities and anisotropy in the stress-strain behaviour (Hoek et al., 2002; Wyllie, 2018). Hence, blocks and zones were allocated rock mass properties. Assuming the blocks and zones to represent the rock mass, the constitutive law requires the following input parameters for the rock mass: the mass density  $\rho$ , the elastic bulk and shear moduli ( $K_m$  and  $G_m$ ), the cohesion  $c_m$ , the internal angle of friction  $\phi_m$  and the tension limit  $\sigma_{tm}$ .

The intact rock data were transferred to rock mass characteristics and switched to field-scale properties following the GSI (Geological Strength Index) rock mass classification system by Hoek and Brown (1997). The GSI system is directly linked to Mohr-Coulomb or Hoek-Brown strength parameters and rock mass deformation moduli (Cai et al., 2004). The deformation modulus of the rock mass  $E_m$  can be described based on a field survey of the rock mass including description and measurement of block volumes and joint characteristics (Hoek et al., 2002):

$$E_m \text{ [GPa]} = \left(1 - \frac{D}{2}\right) \sqrt{\sigma_c} / 100 * 10^{((GSI-10)/40)} \quad \text{Eq. (1)}$$

where  $GSI$  is the geological strength index for the rock mass,  $D$  is the disturbance factor and  $\sigma_c$  is the uniaxial compressive strength of the intact rock. The latter was tested in the laboratory and is a function of temperature (Table 3). Following Cai et

al (2004), a *GSI* value of 65 was derived which relates to an interlocked, mostly blocky to very blocky rock mass formed by four joint sets with a mean spacing of 56 cm (Table 2), and rough slightly weathered surfaces. The disturbance factor *D* was set to 0 as the near surroundings of the profile are not affected by significant blast damage or excavating actions.

380 Values for the elastic rock mass shear and bulk moduli  $G_m$  and  $K_m$  were derived according to the equations presented by Tipler and Mosca (2004) for intact rock:

$$G \text{ [GPa]} = \frac{E_{dyn}}{2 \cdot (1 + \nu)} \quad \text{Eq. (2)}$$

and

$$K \text{ [GPa]} = \frac{E_{dyn}}{3 \cdot (1 - 2 \cdot \nu)} \quad \text{Eq. (3)}$$

385 where the Poisson's ratio  $\nu$ , measured in this study (Table 3), describes the ratio of the transverse strain to the longitudinal strain under conditions of uniaxial stress (Jaeger et al., 2007). For  $G_m$  and  $K_m$ , the dynamic Young's modulus  $E_{dyn}$  was substituted by  $E_m$  (see Eq. (1)). ~~where the Poisson's ratio  $\nu$  describes the ratio of the transverse strain to the longitudinal strain under conditions of uniaxial stress (Jaeger et al., 2007).~~ The mass density  $\rho$  (g/cm<sup>3</sup>), ~~the Poisson's ratio  $\nu$  and the dilatational wave velocity  $V_D$  (m/s) were measured in the laboratory~~ were measured in additional tests (Table 3) and utilised ~~to calculate for calculating~~ the dynamic Young's modulus  $E_{dyn}$  for intact rock (Rentsch and Krompholz, 1961):

$$E_{dyn} \text{ [GPa]} = \rho \cdot V_D^2 \quad \text{Eq. (4)}$$

$E_{dyn}$  and  $G$  were later used to determine the joint stiffness parameters, ~~and the elastic shear and bulk moduli  $G$  and  $K$  for intact rock (Tipler and Mosca, 2004):~~

$$G \text{ [GPa]} = \frac{E_{dyn}}{2 \cdot (1 + \nu)} \quad \text{Eq. (2)}$$

395 ~~and~~

$$K \text{ [GPa]} = \frac{E_{dyn}}{3 \cdot (1 - 2 \cdot \nu)} \quad \text{Eq. (3)}$$

~~where the Poisson's ratio  $\nu$  describes the ratio of the transverse strain to the longitudinal strain under conditions of uniaxial stress (Jaeger et al., 2007).~~

400 the elastic moduli of the intact rock  $E$  (Young's modulus),  $K$  and  $G$ . These were later used to determine the joint stiffness parameters (Sect. 2.1.4.2). The lab results of the Poisson's ratio, and additional lab tests on the intact rock uniaxial compressive strength  $\sigma_c$  were used to quantify elastic moduli and the uniaxial tensile strength  $\sigma_{tnt}$  of the rock mass (see below). The mean dilatational wave velocity and the Poisson's ratio of the intact rock were derived by ultrasonic tests. Then, the dynamic Young's modulus was given by

$$E_{dyn} \text{ [GPa]} = \rho * V_D^2 \text{ Eq. (1)}$$

405 with the rock density  $\rho$  ( $\text{g/cm}^3$ ) and the dilatational wave velocity  $V_D$  ( $\text{m/s}$ ) (Rentsch and Krompholz, 1961). The elastic shear and bulk moduli for the intact rock were calculated with the following equations (Tipler and Mosca, 2004):

$$G \text{ [GPa]} = \frac{E_{dyn}}{2*(1+\nu)} \text{ Eq. (2)}$$

and

$$K \text{ [GPa]} = \frac{E_{dyn}}{3*(1-2*\nu)} \text{ Eq. (3)}$$

410 Here, the Poisson's ratio  $\nu$  describes the ratio of the transverse strain to the longitudinal strain under conditions of uniaxial stress (Jaeger et al., 2007).

~~The intact rock data were transferred to rock mass characteristics and switched to field scale properties following In the next step, the GSI (Geological Strength Index) rock mass classification system of by Hoek and Brown (1997) was used to transfer the intact rock data to rock mass characteristics and switch to field scale properties. The GSI system is directly linked to Mohr-Coulomb or Hoek-Brown strength parameters and rock mass deformation moduli (Cai et al., 2004; Hoek and Brown, 1997). It is semi-quantitative and requires a field survey of the rock mass including description and measurement of block volumes and joint characteristics. Following this scheme, tThe deformation modulus of the rock mass can be described based on a field survey of the rock mass including description and measurement of block volumes and joint characteristics (Hoek et al., 2002); was given by~~

$$420 E_m \text{ [GPa]} = \left(1 - \frac{D}{2}\right) \sqrt{\sigma_c/100} * 10^{((GSI-10)/40)} \text{ Eq. (4)}$$

where  $GSI$  is the geological strength index for the rock mass,  $D$  is the disturbance factor and  $\sigma_c$  is the uniaxial compressive strength of the intact rock (Hoek et al., 2002). The latter and is a function of temperature (Table 3). ~~Following Cai et al (2004), Aa  $GSI$  value of 65 was derived from the proposed chart by Cai et al. (2004; Fig. 7) relating to a blocky to very blocky rock mass formed by four joint sets with a mean spacing of 56 cm, a mean persistence of and rough, slightly weathered surfaces.~~

425 ~~The disturbance factor  $D$  was set to 0 as no significant blasting or excavating actions have been performed in the near surroundings of the profile. The rock mass internal friction angle  $\phi_m$  and cohesion  $c_m$  were estimated with the  $GSI$  and the Hoek-Brown constant  $m_i$  according to Cai et al. (2004). Consider, while rock mass cohesion- could be determined for both thermal conditions (as it is based on the temperature dependent uniaxial compressive strength), the unfrozen friction angle value was used for all thermal conditions (as the respective relation is not temperature dependent).~~

430 Values for the rock mass bulk and shear moduli were derived according to Eq. (2) and (3) with the respective  $E_m$  values. The rock mass internal friction angle  $\phi_m$  and cohesion  $c_m$  were estimated with the  $GSI$  and the Hoek-Brown constant  $m_i$ , following the strategy by Cai et al. (2004; Fig. 5) which is valid for  $\sigma_3 < 5$  MPa. Since the temperature dependent uniaxial compressive strength is included in the equations for the cohesion, rock mass cohesion values could be determined for both thermal states.

435 However, the frozen friction angle was set to the same value as the unfrozen one because the respective relation is not temperature dependent. The uniaxial tensile strength  $\sigma_{tm}$  was calculated with the following relation

$$\sigma_{tm} = \frac{\sigma_c}{2} (m_b - \sqrt{m_b^2 + 4s}) \quad \text{Eq. (5)}$$

where  $\sigma_c$  is the uniaxial compressive strength of the intact rock and  $m_b$  and  $s$  are constants for the rock mass (Hoek and Brown, 1997).

440 All mechanical properties of the intact rock and the rock mass, either tested in the laboratory or calculated, decrease temperature-dependently with 0.3 to 0.8 % °C<sup>-1</sup> (absolutely 8–22 %) upon thawing (see Table 3 and Table 4); this pattern corresponds with other mechanical studies (see Table 1). While the increase in deformability is more pronounced for intact rock (0.8 % °C<sup>-1</sup>; 20.4–20.5 %) than for rock mass (0.3 % °C<sup>-1</sup>; 8.3–8.9 %), the tensile strength decreases by a similar amount when comparing intact rock with rock mass. This difference can be explained by the small variation in frozen and unfrozen  $E_m$ -values caused by the similar frozen and unfrozen intact rock uniaxial compressive strength (see Eq. (1)).

445

**Table 3: Laboratory-tested strength reduction of intact dolomised Wetterstein limestone due to thawing. Standard deviations (indicated with ±) are given for measured parameters, and they were used for determination of minimum and maximum values (given in parentheses) of the calculated parameters. RMC refers to parameters that are used for rock mass characterisation.**

Mechanical parameter	Saturated	Saturated	Decrease due to		Test / equation applied	RMC
	frozen (-5 °C)	unfrozen (+22 °C)	%	% °C <sup>-1</sup>		
Density $\rho$ [g/cm <sup>3</sup> ]	--	2.7 ± 0.01	--	--	Weighing tests in water bath	x
Porosity $n$ [%]	--	0.9 ± 0.4	--	--	Weighing tests in water bath	
<u>Young's modulus <math>E</math> [GPa]</u>	<u>84.3</u> <u>(81.7/85.3)</u>	<u>67.1</u> <u>(55.7/77.6)</u>	<u>20.4</u>	<u>0.8</u>	<u>Eq. (1), after Tipler and Mosca (2004)</u>	
Shear modulus $G$ [GPa]	32.4 (31.7/32.6)	25.8 (21.9/29.2)	20.4	0.8	Eq. (2), after Tipler and Mosca (2004)	
Bulk modulus $K$ [GPa]	70.3 (64.8/74.8)	55.9 (40.4/76.0)	20.5	0.8	Eq. (3), after Tipler and Mosca (2004)	
<u>Young's modulus <math>E</math> [GPa]</u>	<u>84.3</u> <u>(81.7/85.3)</u>	<u>67.1</u> <u>(55.7/77.6)</u>	<u>20.4</u>	<u>0.8</u>	<u>Eq. (4), after Tipler and Mosca (2004)</u>	
Poisson's ratio $\nu$	0.3 ± 0.01	0.3 ± 0.03	0	0	Ultrasonic tests	x
Dilatational wave velocity $V_D$ [m/s]	5560 ± 50	4950 ± 400	11.0	0.4	Ultrasonic tests	
Uniaxial tensile strength $\sigma_t$ [MPa]	9.0 ± 1.4	7.2 ± 1.9	20.0	0.7	Brazilian tests	
Uniaxial compressive strength $\sigma_c$ [MPa]	109 ± 25	91 ± 27	16.5	0.6	Uniaxial compressive strength tests	x

450

**Table 4: Estimated and calculated strength reduction of Wetterstein limestone rock mass due to thawing, derived from the GSI scheme after Hoek and Brown (1997). Minimum and maximum values of calculated parameters are given in parentheses. These were determined with the standard deviations of the measured parameters (Table 3). IP = used as input parameter for the numerical model.**

Mechanical parameter	Saturated frozen (-5 °C)	Saturated unfrozen (+22 °C)	Decrease due to thawing %      % °C <sup>-1</sup>		Test / equation applied	IP
<del>Young's modulus <math>E_m</math> [GPa]</del>	<del>24.8 (21.7/27.5)</del>	<del>22.6 (19.0/25.8)</del>	<del>8.9</del>	<del>0.3</del>	<del>Eq. (1), after Hoek et al. (2002)</del>	
Shear modulus $G_m$ [GPa]	9.5 (8.4/10.5)	8.7 (7.5/9.7)	8.4	0.3	Eq. (2), after Tipler and Mosca (2004)	x
Bulk modulus $K_m$ [GPa]	20.6 (17.2/24.1)	18.9 (13.7/25.3)	8.3	0.3	Eq. (3), after Tipler and Mosca (2004)	x
<del>Young's modulus <math>E_m</math> [GPa]</del>	<del>24.8 (21.7/27.5)</del>	<del>22.6 (19.0/25.8)</del>	<del>8.9</del>	<del>0.3</del>	<del>Eq. (4), after Hoek et al. (2002)</del>	
Uniaxial tensile strength $\sigma_m$ [MPa]	-0.9 (0.7/-1.1)	-0.7 (-0.5/-0.9)	22.2	0.8	Eq. (5), after Hoek et al. (2002)	x
Friction angle $\phi_m$ [°]	44 <sup>a</sup>	44	0	0	estimated after Cai et al. (2004)	x
Cohesion $c_m$ [MPa]	3.9	3.3	15.4	0.6	estimated after Cai et al. (2004)	x
Parameter of the Hoek-Brown strength criterion						
$GSI$ value	--	65	--	--	estimated after Marinos and Hoek (2000)	
$m_i$	--	9	--	--	estimated after Marinos and Hoek (2000)	
$m_b$	--	2.6	--	--	calculated after Hoek et al. (2002)	
$s$	--	0.02	--	--	calculated after Hoek et al. (2002)	
Disturbance factor $D$	--	0	--	--	estimated after Hoek et al. (2002)	

455 **Note: <sup>a</sup>The frozen rock mass friction angle was not estimated. It was given the same value as for the unfrozen friction angle, resulting in a decrease in thawing of zero.**

~~All mechanical properties of intact rock and rock mass, either tested in the laboratory or calculated, Virtually all of the laboratory tested or calculated properties of the intact rock and the rock mass decrease temperature dependently between with 0.3 and to 0.8 % °C<sup>-1</sup> (absolutely 8–22 %) upon thawing (see Table 3 and, Table 4) and corresponds . Similar patterns have been observed in with other mechanical studies of (see thawing rock summarised in Table 1). While As expected, the absolute values are higher for the intact rock compared to rock mass, . The uniaxial tensile strength and the elastic moduli were determined for both the intact rock and the rock mass. Here, the tensile strength decreases by a similar amount, while and the increase in deformability is more pronounced for the intact rock (0.8 % °C<sup>-1</sup>; 20.4–20.5 %) than for the 460 rock mass (0.3 % °C<sup>-1</sup>; 8.3–8.9 %). This difference can be explained by the small variation in frozen and unfrozen  $E_m$  values caused by the similar frozen and unfrozen intact rock uniaxial compressive strength (see Eq. (4)). 465~~

### 2.5.2 Frozen and unfrozen rock joints

Rock joint parameters for ice free and ice filled joints were considered were collected in the presented for stability analyses with ice free joints and ice filled joints. In UDEC, the strength and deformability and strength of rock discontinuities were simulated by the Mohr-Coulomb area contact constitutive model, which requires the cohesion  $c$ , friction angle  $\phi$ , joint normal stiffness  $k_n$  and joint shear stiffness  $k_s$  as input parameters. Rock joint parameters for ice-free and ice-filled joints were considered in the presented stability analyses.

The deformability of the joints is described by the joint normal stiffness  $k_n$  and joint shear stiffness  $k_s$ :

$$k_n \text{ [MPa/m]} = \frac{E_m * E}{s * (E - E_m)} \quad \text{Eq. (6)}$$

and the joint shear stiffness  $k_s$ :

where  $s$  is the joint spacing (m) and  $E_m$  and  $E$  are the rock mass, and intact rock Young's moduli (GPa) respectively (Barton, 1972). Since the ratio of  $E/G$  is analogous to the  $k_n/k_s$  ratio, the joint shear stiffness is given by

$$k_s \text{ [MPa/m]} = \frac{G_m * G}{s * (G - G_m)} \quad \text{Eq. (7)}$$

where  $s$  is the joint spacing (m), and  $E_m$  and  $E$  are the Young's moduli (GPa) for rock mass, and intact rock Young's moduli (GPa) respectively (Barton, 1972) and  $G_m$  and  $G$  are the shear moduli (GPa) for rock mass and intact rock respectively (Glamheden and Lindblom, 2002; Itasca Consulting Group, 2019) Kulatilake et al., 1992). Note that, Since the ratio of  $E/G$  is analogous to the  $k_n/k_s$  ratio, the joint shear stiffness is given by

where  $G_m$  and  $G$  are the rock mass and intact rock shear moduli (GPa) respectively (Kulatilake et al., 1992). Finally,

To determine the temperature ( $T$ ) dependent cohesion  $c$

$$c \text{ [kPa]} = 104.5 - 143.8 * T \quad \text{Eq. (8)}$$

and friction  $\phi$

$$\tan [\phi] = 0.19 - 0.1 * T \quad \text{Eq. (9)}$$

of frozen ice-filled rock joints are determined based on the, we utilised the brittle failure criterion presented by Mamot et al. (2018) which is valid for temperatures ranging from -4 to -0.5 °C and normal stresses between 100 and 800 kPa.:

$$c \text{ [kPa]} = 104.5 - 143.8 * T \quad \text{Eq. (8)}$$

and

$$\tan [\phi] = 0.19 - 0.1 * T \quad \text{Eq. (9)}$$

where  $T$  is the temperature of the rock at failure (Mamot et al., 2018). Equations (8) and (9) are valid for temperatures ranging from -4 to -0.5 °C and normal stresses between 100 and 800 kPa. As such, Therefore, the cohesion and friction angle were

495 calculated for temperatures -4, -3, -2, -1 and -0.5 °C, which are currently measured in the frozen sections of the Zugspitze  
summit (Gallemann et al., 2017). The stress range of 100–800 kPa ~~resembles the~~ corresponds to the rock overburden  
represented by the model of the Zugspitze summit crest (Fig. 3b).

Values for the cohesion of frozen and unfrozen, ice-free rock joints were roughly estimated from (Krautblatter et al., 2013).  
As initial displacements lead to the destruction of asperities and smoothing of joint surfaces, ~~the~~ frictional strength of rock-  
500 rock contacts was represented by the residual friction angle  $\varphi_r$ , ~~as initial displacements lead to the destruction of asperities and  
smoothing of joint surfaces. Weathering of the surfaces sets in with the progressive destruction of rock bridges and the  
successive contact and reaction with infiltrating water from precipitation or snow melt. The residual friction angle  $\varphi_r$  was  
estimated with the suggested equation by following~~ -Barton ~~& and~~ Choubey (1977):

$$\varphi_r = (\varphi_b - 20^\circ) + 20 * \left(\frac{r}{R}\right) \quad \text{Eq. (10)}$$

505 where  $\varphi_b$  is the basic friction angle,  $r$  is the Schmidt hammer rebound value of weathered surfaces, and  $R$  is the Schmidt hammer  
rebound value of unweathered, sawn surfaces. ~~To determine~~ Rebound hardness values of weathered frozen and unfrozen  
Wetterstein limestone surfaces were collected with the Schmidt hammer (N-type) following the proposed method by Aydin et  
al. (2005) and Ulusay (2015). In contrast, the basic friction angle, was determined by tilt tests of frozen and unfrozen joint  
surfaces ~~were conducted in this study following the recommendations by Barton and Choubey (1977) and~~ as recommended by  
510 Barton (2013).

~~Rebound hardness values of weathered frozen and unfrozen Wetterstein limestone surfaces were collected with the Schmidt  
hammer (N-type) following the proposed method by Aydin et al. (2005) and Ulusay (2015). The investigated and calculated  
joint deformation and mechanical strength properties reduced absolutely by 2 to 22 % upon thawing (corresponding to a  
decrease by 0.1–0.8 % °C<sup>-1</sup>; Table 5). The small variation between in frozen and unfrozen  $E_m$ -values results in was also the  
reason for the a small differences between in the frozen and unfrozen  $k_n$  joint normal and shear stiffness  $k_s$  (0.1 % °C<sup>-1</sup>; 2.6–  
2.8 %). In contrast~~ However, the stiffness values vary more strongly ~~referring to~~ between ~~the~~ various joint sets which are  
also additionally dependent on the specific joint spacing. In general, the estimated measured unfrozen  $k_n$  and  $k_s$  joint normal and  
shear stiffness lie well within the range of values proposed by the UDEC database (Itasca Consulting Group, 2019) and  
Kulatilake et al. (1992), or measured by Barton (1972) and Bandis et al. (1983). Similarly, the measured unfrozen  $\varphi_b$  joint  
520 basic friction angle corresponds well to the values listed e.g. in Barton and Choubey (1977).



**Table 5: Laboratory-tested and calculated strength reduction of saturated Wetterstein limestone discontinuities due to warming or thawing. Standard deviations (indicated with ±) are given for measured parameters, and they were used for determination of minimum and maximum values (given in parentheses) of the calculated parameters. IP = used as input parameter for the model.**

Joint mechanical parameter	Type of joint filling	Sub-zero temperature [°C]	Frozen						Unfrozen (+22 °C)			Decrease due to thawing/warming		Reference / Equation applied	IP
			Joint set						K1	K3	K4 / shear zone	%	% °C <sup>-1</sup>		
			K1	K3	K4 / shear zone										
Normal stiffness [MPa m <sup>-1</sup> ]	ice-free/ice-filled	-5	26000	11100	13000	25300	10800	12600	2.8	0.1	Eq. (6), calculated after Barton (1972)	x			
			(21900/30000)	(9400/2900)	(11000/15000)	(21300/28600)	(9100/2200)	(10700/14300)							
Shear stiffness [MPa m <sup>-1</sup> ]	ice-free/ice-filled	-5	10000	4300	5000	9700	4200	4900	2.6	0.1	Eq. (7), calculated after Kulatilake et al. (1992)	x			
			(8500/400)	(3600/900)	(4300/5700)	(8400/10700)	(3600/600)	(4200/5400)							
Cohesion [MPa]	ice-filled	-4	0.68 (0.45/0.91)			--			74.1	21.2.	Eq. (8), calculated after Mamot et al. (2018)	x			
			-3	0.54 (0.35/0.72)			--								
				-2	0.41 (0.25/0.54)			--							
					-1	0.26 (0.15/0.35)							--		
				-0.5		0.18 (0.10/0.26)							--		
	ice-free	-4.5	0.00			0.00			0	0	estimated after Krautblatter et al. (2013)	x			
Peak friction angle [°]	ice-filled	-4	30.5 (26.1/34.6)			--			59.3	17.0	Eq. (9), calculated after Mamot et al. (2018)	x			
			-3	26.4 (22.3/29.7)			--								
				-2	22.0 (18.3/24.2)			--							
					-1	16.8 (14.0/18.3)							--		
				-0.5		13.5 (11.9/15.1)							--		
Rebound value for dry unweathered, sawn surfaces	ice-free	-5	55.0 ± 1.0			51.9 ± 1.0			1.6	0.1	Schmidt Hammer tests				
Rebound value for wet weathered surfaces	ice-free	-5	53.0 ± 2.1			52.1 ± 0.8			1.7	0.1	Schmidt Hammer tests				
Basic friction angle [°]	ice-free	-5	38.3 ± 4.4			30.0 ± 4.7			21.7	0.8	Tilt tests				

Residual friction angle [°]	ice-free	-4.5	37.6 (32.8/42.4)	30.1 (25.5/34.7)	22.1	0.8	Eq. (10), calculated after Barton and Choubey (1977)	x
-----------------------------	----------	------	---------------------	---------------------	------	-----	------------------------------------------------------------	---

---

525

~~The investigated and calculated joint deformation and mechanical strength properties reduced by 2 to 22 % upon thawing (corresponding to a decrease by 0.1–0.8 % °C<sup>-1</sup>; Table 5). The small variation in frozen and unfrozen  $E_m$  values was also the reason for the small differences in the frozen and unfrozen joint normal and shear stiffness (0.1 % °C<sup>-1</sup>; 2.6–2.8 %). However, the stiffness values vary more strongly referring to the various joint sets which are additionally dependent on the specific joint spacing. In general, the measured unfrozen joint normal and shear stiffness lie well within the range of values proposed by the UDEC database (Itasca Consulting Group, 2019) and Kulatilake et al. (1992), or measured by Barton (1972) and Bandis et al. (1983). Similarly, the measured unfrozen joint basic friction angle corresponds well to the values listed e.g. in Barton and Choubey (1977).~~

530

## 535 **2.26 Model setup**

The topography of the rock slope used in the model was derived from a digital terrain model of the Zugspitze summit area. Three fully persistent joint Joint-sets (K1, K3, K4) and the dominant shear zone were included (Fig. 3b). For simplification and shorter computation time, the joint spacing was chosen to be five times greater scaled up in the model by factor five than in reality. All joint sets were created as fully persistent. The presence of intact rock bridges was accounted for according to the approach by Jennings (1970). After this, the joint cohesion and friction angle were proportionately increased by the respective same values of the rock mass cohesion and friction angle dependent on the estimated percentages of the surface areas of rock bridges and joints within the rock slope. ~~However, the joint stiffness values were not changed for the different degrees of joint persistence.~~

540

The blocks in the model are supposed to be deformable and were subdivided into a mesh of finite-difference elements. ~~The size of the mesh was determined to be with a size of~~ 1.5 m. The stress field was initialised according to the varying density of overburden which depends on the topography of the slopes. We assumed a horizontal to vertical stress ratio of 0.5. Roller boundary conditions were implemented at the sides of the model (i.e. vertical movements were allowed), whereas vertical and horizontal displacements were suppressed along the base.

545

The combined boundary of bedrock permafrost within the summit ridge, derived from ~~ER tomographies~~ ERT measurements of 2014 and 2015 (Fig. 4b), was used to define the current frozen and unfrozen sections of the numerical model. Then, we introduced six subsurface layers to simulate a stepwise warming or thawing from the slope surface to the core of the crest by adjusting the temperature-dependent material parameters for a specific temperature level and subsequent numeric cycling. The layers are oriented parallel to the derived permafrost boundary and account for a stronger warming signal directed from the south-slope (Fig. 5). The defined current permafrost boundary and the estimated spatial pattern of layers for warming are both in accordance with modelled current and future thermal fields of arbitrary mountain ridge geometries (Noetzli et al., 2007) and, in particular, of the Zugspitze (Böckli et al., 2011; Noetzli, 2008).

555

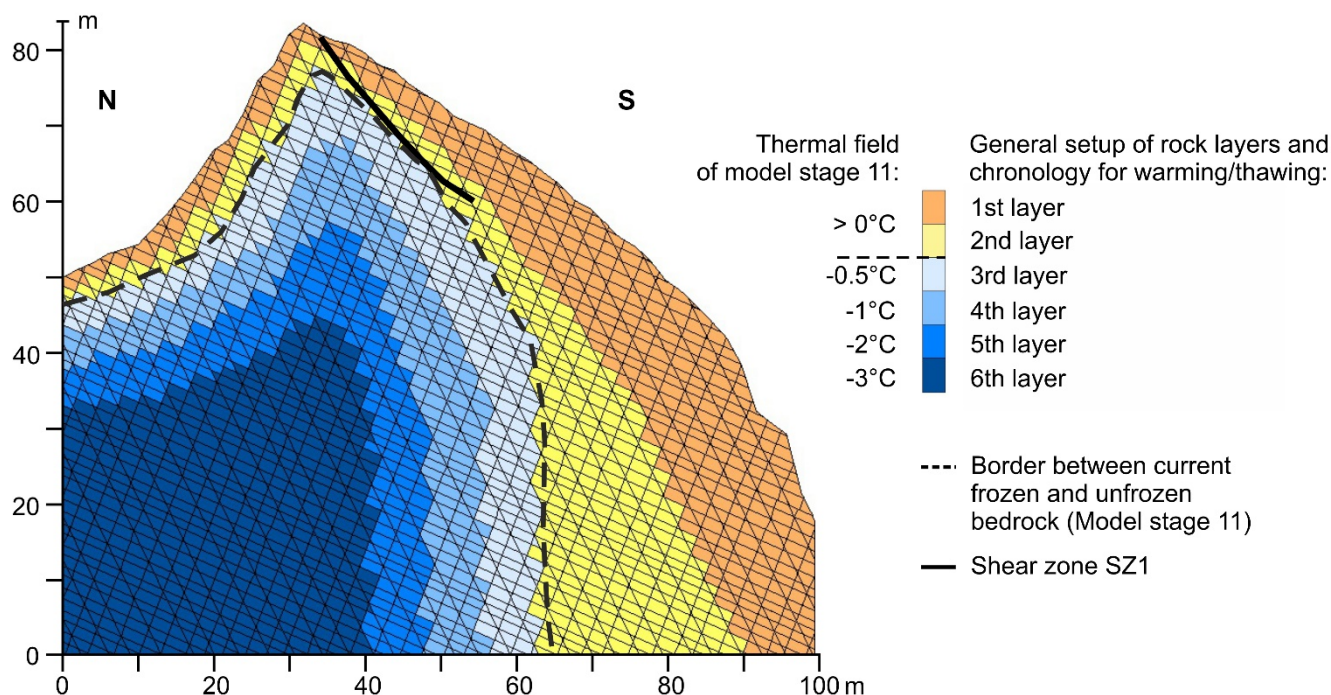


Figure 5: Spatial warming/thawing pattern for the numerical model of the Zugspitze summit crest. For each warming/thawing step, the six rock layers (coloured areas) are assigned an individual temperature with a characteristic set of mechanical parameters. Warming or thawing proceeds from the outside to the inside of the crest. The dashed black line marks the current boundary between frozen and unfrozen rock, derived in Section 2.4. The presented thermal field is estimated and refers to model stage 11 in Table 6 (current state of permafrost distribution in the crest).

### 2.7.3 Procedure for the numerical analysis

The general modelling procedure consists of four steps: the calculation of an initial equilibrium and three successive steps of potential destabilisation which include —the progressive destruction of intact rock bridges, the warming and the thawing of a permafrost rock slope:

1) Initial state: The numerical analysis was started by developing an initial equilibrium with a low joint persistence of 30 % (Model stage 1 in Table 6). The summit crest is assumed to be fully frozen representing an undefined moment in the past.

2) The progressive loss of rock bridges: The destabilisation of a permafrost-affected rock slope is initiated by the progressive destruction of cohesive intact rock bridges which prepare new shear planes along which displacement can take place (Krautblatter et al., 2013). The current overall joint persistence was assessed to 90–100 % as we observed a high trace length of the discontinuities and a displacement of several decimetres along the main shear zone indicating that most of the rock bridges are lost. The past destruction of rock bridges was simulated by a reduction of the apparent joint cohesion and friction angle in three steps which represents a progressive increase of  $e$  of the joint

persistence from 30 to 90 % ~~was implemented for the whole model by a reduction of the joint strength in three steps (Stages 1–4 in Table 6.) For this, we decreased the apparent joint cohesion and friction angle for each model stage based on the approach by Jennings (1970) (Table 7; for more details see supplement, Sect. S7).~~

~~2) This procedure simulates “step path” failure on the slope scale in a simplified way which is characterised by the interconnection of pre-existing, adjacent discontinuities through intact rock bridges (Camones et al., 2013; Eberhardt et al., 2004; Huang et al., 2015). The reduction in the shear strength involves processes of stress concentration, crack initiation, crack propagation and coalescence, slip weakening and the formation of a continuous failure plane or zone (Zhang et al., 2015), which were not numerically modelled as this would be beyond the scope of this study. The presented model of the Zugspitze ridge considers crack coalescence to occur by shear and tensile mode or a tensile-shear combination, which has been observed on the micro-scale by Zhang and Wong (2013). The resulting new connections can form coplanar or oblique to the pre-existing joints (Huang et al., 2015). At the scale of the Zugspitze ridge, we assume the joint sets K1, K3 and K4 to link in both coplanar and oblique form, leading to the formation of straight or stepped failure planes.~~

Joints may be partly filled with ice during the loss of rock bridges. ~~However, as such, joints were the assigned joint properties were those of ice-free joints as, a~~ However, according to Krautblatter et al. (2013), deformation and shear strength are mainly controlled by rock-mechanical processes at this early stage of destabilisation. As long as a certain part of intact rock bridges and asperities along joint surfaces are present, stresses are supposed to concentrate at these locations while the softer ice fillings may be squeezed away (in particular, in greater depths). ~~As such, the assigned joint properties were those of ice-free joints.~~

Following Krautblatter et al. (2013), the advanced stage of accelerated displacements in a permafrost-affected rock slope begins as soon as most of the rock bridges are broken. Then, ice mechanics (fracturing of rock-ice contacts and ice, as well as the creep of ice) will increasingly replace rock mechanics (friction of rock-rock contacts and fracture of rock bridges) in controlling displacements along discontinuities and their potential acceleration. To introduce this stage of destabilisation, the joint persistence was further increased to 100 % and ~~the frozen~~ rock joints were simulated to be ice-filled up with ice (Stage 5 in Table 6). ~~By doing this, we ensure the joint mechanical behaviour is fully controlled by ice mechanical processes.~~ For simplification and due to data availability, the joint shear resistance was solely given by the fracture of ice or rock-ice contacts, while the creep of ice was neglected.

- 3) Warming permafrost: The ~~frozen crest was next step was to~~ gradually warmed ~~the frozen crest~~ from the slope surface to the core from -4 to -0.5 °C (Stages 6–9 in Table 6). ~~The spatial pattern of~~ This warming was applied based to on the six rock layers defined in Fig. 5. Firstly, the outermost (orange) section was warmed to -3 °C, while inner sections remained at -4 °C (Stage 6). After that, the outermost section was warmed to -2 °C and the adjacent inner section (yellow layer in Fig. 5) was warmed to -3 °C, while inner sections remained unchanged (Stage 7). This procedure was continued until the outermost layer was at -0.5 °C (Stage 9). Each warming step was characterised by adjusting the temperature-dependent material parameters to the warmer temperature and by subsequent numeric cycling. The spatial

615 ~~pattern of warming was based on the six rock layers defined in Fig. 5. The simulated numerically modelled temperature range and the steps of warming were predetermined by the specific temperatures the implemented cohesion and friction angle of ice filled rock joints are valid for (Eq. (8) and (9)). of the rock mass. This temperature range is consistent with temperatures currently monitored in boreholes temperatures in permafrost rock walls across the European Alps (Gallemann et al., 2017; Noetzli et al., 2019). The warming procedure works as follows: Firstly, the outermost (orange) section was warmed to 3 °C, while inner sections remained at 4 °C (Stage 6). After that, the outermost section was warmed to 2 °C and the adjacent inner section (yellow layer in Fig. 5) was warmed to 3 °C, while inner sections remained unchanged (Stage 7). This procedure was continued until the outermost layer was at 0.5 °C (Stage 9). Each warming step was characterised by adjusting the temperature dependent material parameters to the warmer temperature and by subsequent numeric cycling.~~

- 620
- 4) Thawing from the slope surface to the core was implemented in the same way as warming (Stages 10–15 in Table 6), until all subsurface layers of the summit ridge were unfrozen. The spatial pattern of thawing is illustrated in Fig. 5.

625 To assess the level of a potential slope stability loss due to warming or thawing, we calculated the factor of safety (FS) by using the common strength reduction technique (Wyllie, 2018). Thereby, the cohesion and frictional strength of the rock mass and the joints are were reduced simultaneously and gradually by varying increasing strength reduction trial factors in a series of numerical simulations until failure occurred. A bracketing solution approach was applied to progressively reduce the bracket between stable and unstable solutions until it falls below a specified threshold (Itasca Consulting Group, 2019). The resulting FS is a single indicator of minimum stability which globally refers to the entire slope.

630

**Table 6: Modelling strategy for the Zugspitze summit crest. The model was run with varying rock mass temperature, joint persistency and filling. The temperature levels for gradual warming were: -4, -3, -2, -1 and -0.5 °C.**

Model stage	Thermal state of the rock slope	Joint persistence [%]	Type of joint filling	Principal steps of the numerical analysis
1		30		Initial equilibrium
2	All frozen (-4 to -5 °C)	50	no ice	Progressive destruction of rock bridges
3		70		
4		90		
5	All frozen (-4 °C)	100	ice-filled	
6	1st layer at -3 °C	100	ice-filled	Stepwise warming from rock surface to core in 4 steps
7	-2 °C			
8	-1 °C			
9	-0.5 °C			
10	1st layer unfrozen	100	thawed layers: no ice / frozen layers: ice-filled	Stepwise thawing from rock surface to core in 6 steps
11	2nd layer unfrozen			
12	3rd layer unfrozen			
13	4th layer unfrozen			
14	5th layer unfrozen			
15	All unfrozen			

635

~~To assess the level of a potential stability loss due to warming or thawing, we calculated the factor of safety (FS) by using the strength reduction technique. Thereby, the cohesion and frictional strength of the rock mass and the joints were reduced simultaneously by varying strength reduction factors in a series of simulations until failure occurred. A bracketing solution approach was applied to progressively reduce the bracket between stable and unstable solutions until it falls below a specified threshold (Itasca Consulting Group, 2019). The resulting FS is a single indicator of minimum stability which globally refers to the entire slope.~~

640

**Table 7: Implemented strength properties for ice-filled and frozen ice-free joints during the initial stage of rock bridge destruction, represented by a joint persistence of 30 to 90 %. The different cohesion and friction values are calculated after Jennings (1970) and depend on the estimated relative percentage of rock bridges and joints. The corresponding values at a joint persistence of 100 % are shown in Table 5.**

Joint mechanical parameter	Type of model	Type of joint filling	Joint persistence [%]			
			30	50	70	90
Apparent cohesion [MPa]	Zugspitze summit crest (Sect. 4.1.)	Ice-free	2.8	2.00	1.2	0.4
	Simplified rock slope (Sect. 4.2.)	Ice-filled	--	--	--	1.0
Apparent residual friction angle [°]	Zugspitze summit crest (Sect. 4.1.)	Ice-free	42.1	40.8	39.5	38.2
	Simplified rock slope (Sect. 4.2.)	Ice-filled	--	--	--	31.9

### 3 Sensitivity analysis for a simplified, warming permafrost rock slope

The relation between the dip of the joint sets, especially the bedding, and the slope-face is a crucial factor for rock slope stability (Cruden, 2003; Wyllie, 2018). Thus, we performed a sensitivity analysis on the numerical impact of varying (i) slope angles and (ii) orientations of the fracture network on rock slope stability. ~~For this, we transferred the Zugspitze model to a rock slope with a simplified topography and warming steps were applied to the entire model domain without spatial differentiation warming procedure without spatial differentiation. - T~~ For this, the topography of the Zugspitze south-face was modified to a straight line. In accordance with the dimensions of the crest geometry, the height of the slope and the width of the upper-face were standardised to 84 m and 32 m, respectively (Fig. 7). ~~A stepwise warming of the frozen rock and ice-filled joints (Stages 5–9) was only applied to the study of the slope angle.~~

Modelling was applied to 12 different slope angles between 30 and 69°. For inclinations of 70° and higher, no initial equilibriums could be calculated as cycling exceeded the maximum computation time. ~~Material properties and T~~ the joint set orientations were kept constant. In a first step, an initial equilibrium was calculated for a frozen rock slope with ice-filled joints and a joint persistence of 90 %. In a second step, the joint persistence was increased to 100 %, and then the ~~entire~~ rock slope was warmed in four steps from -4 to -0.5 °C (by reducing the rock joint strength equivalent to the ~~procedure at the~~ Zugspitze ~~model summit crest~~). ~~However, e~~ Each warming step to the next degree centigrade was applied to the entire rock slope and not just to a single rock layer. Reducing the complexity of the model facilitates the transferability to other frozen rock slopes.

~~WAs mentioned above, we~~ also remodelled the stability for ~~12 different varying~~ dip angles of the fracture network with reference to the slope. The positioning of the three model joint sets to each other was held constant, while rotating them counter-clockwise in steps of 15° for each of the 12 slope angles used for the first sensitivity test. ~~The analysed 13 different~~ orientations of the fracture network ~~were modelled~~ represented ~~ing~~ anaclinal and cataclinal slopes after Cruden (2003; Fig. 3). Hereafter, cataclinal slopes have a slope-face and bedding with the same dip direction whereas, for anaclinal slopes, the dips of both planes have the opposite direction. The orientation and dip of the fracture network was represented by the bedding and then applied to the scheme after Cruden (2003). ~~The simulated temperature of the rock mass was constantly at -4 °C since a~~ ~~stepwise warming of the frozen rock and ice-filled joints (Stages 5–9) was not only applied to the study of the slope angle. The~~ ~~simulated temperature was -4 °C.~~

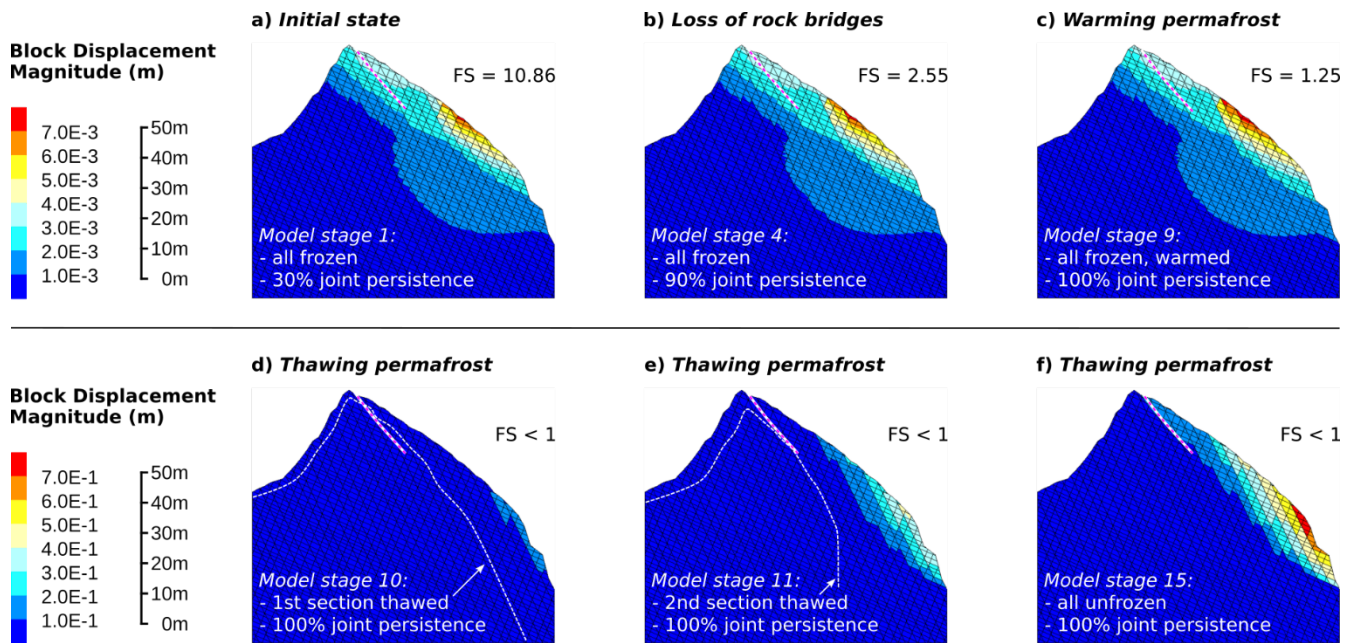
## 4 Numerical model rResults

### 4.1 SNumerical stability of the warming/thawing Zugspitze crest

Figure 6 shows the ~~Zugspitze~~ cross section of the Zugspitze summit crest with a factor of safety for different model states. ~~(color indicates the block displacement magnitude, note that a c and d f use different scales).~~ While an increase in joint



675 persistence or warming hardly leads to a rising increase in the block displacement magnitude (indicated by colours, note that  
a-c and d-f use different scales), thawing causes a drastic increase in block displacements magnitude. As soon as thawing  
starts, the south-face becomes unstable and maximum displacements increase to 0.14 m (Stage 10, Fig. 6d). Rock deformations  
rise to 0.42 m when the dimension of thawed bedrock reaches the current state (Stage 11, Fig. 6e), and measure 0.78 m for the  
whole rock slope thawed (Stage 15, Fig. 6f). The highest deformations (> 0.4 m) concentrate on the upper 5–7 m of rock in  
680 the most inclined lower part of the slope (with a mean angle of 49°). While warming brings the factor of safety close to unity,  
it lies below 1 for all Stages 10–15 which refer to thawing. At the initial state and during the stage of progressive rock bridge  
destruction (Stages 1–4 in Table 6, Fig. 6a–b), the entire rock slope is still uniformly frozen at -4 °C. Here, the maximum block  
and zone displacements are very low and do not change significantly (from 7.6 mm to 7.7 mm). The factor of safety decreases  
from 10.9 to 2.6. Filling the joints with ice and breaking the remaining rock bridges does not cause important deformation or  
685 strength reduction (Stage 5 in Table 6). The maximum block and zone displacements decrease by 0.02 mm.



690 **Figure 6:** Calculated spatial distribution and magnitude of displacements for the Zugspitze summit ridge. (a)–(c) Factors of safety (FS) are given for Stages 1, 4 and 9 which refer to the loss of rock bridges and warming. (d)–(f) Stages 10, 11 and 15 correspond to thawing with FS below 1. The prominent shear zone is marked by a white-red dashed line. The permafrost boundary in (d) and (e) is highlighted by a white dashed line.

The stage of stepwise warming was simulated by following the procedure outlined in Sect. 2.3, until the outermost rock layer was at -0.5 °C and the two inner layers still remained at -4 °C (Stages 6–9 in Table 6). Stepwise warming was applied to the  
695 rock layers defined in Fig. 5. Changes in the maximum displacements are very low and increase by 0.5 mm (from 7.7 to

8.2 mm, Fig. 6e). The spatial pattern of rock mass deformation does not change either. The factor of safety approaches unity (FS = 1.25) but still remains above it.

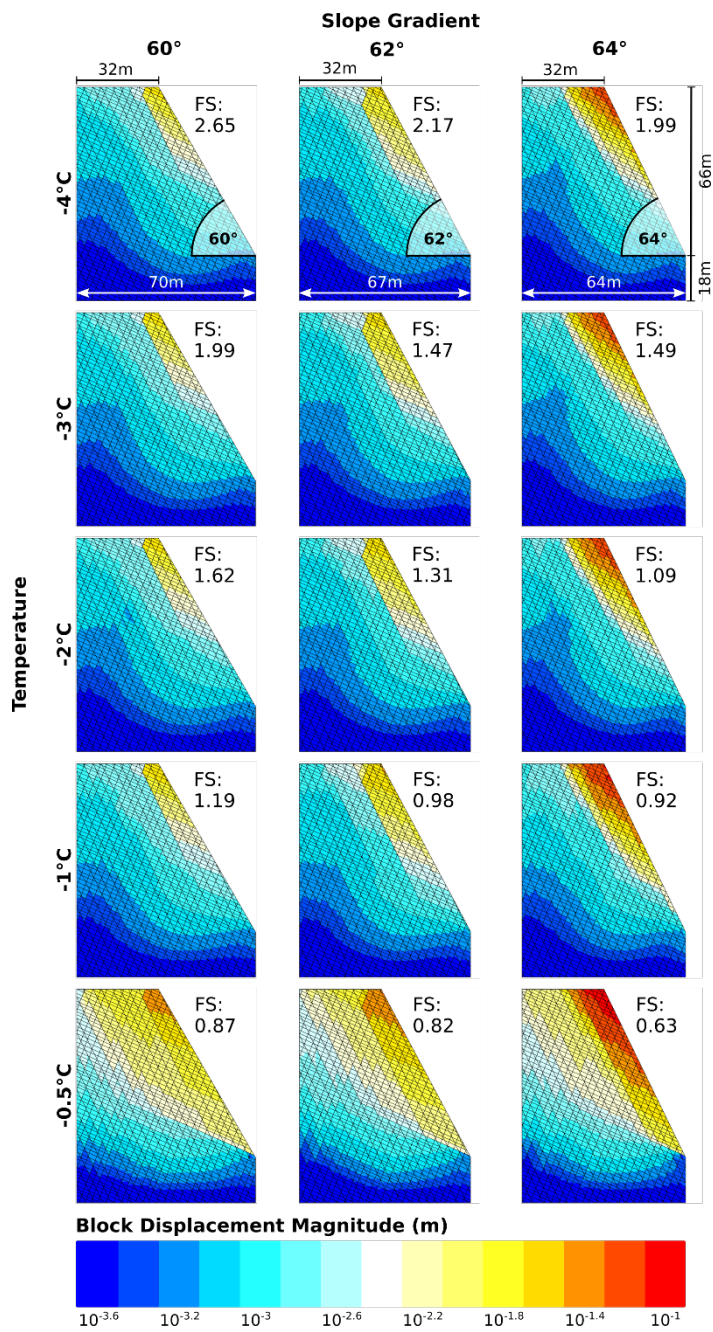
Thawing firstly affects the surficial rock layer. As soon as thawing starts, the south face becomes unstable and maximum displacements increase to 141.1 mm (Stage 10, Fig. 6d). Rock deformations rise to 419.5 mm when the dimension of thawed bedrock reaches the current state (Stage 11, Fig. 6e), and measure 776.3 mm for the whole rock slope thawed (Stage 15, Fig. 6f). The highest deformations (> 400 mm) concentrate on the upper 5–7 m of rock in the most inclined lower part of the slope (with a mean angle of 49°). The factor of safety lies below 1 for all Stages 10–15 which refer to thawing.

## 4.2 Stability of a sensitivity analysis for a simplified permafrost rock slope with rising temperature

Results of the studied numerical influence of a varying slope angle or orientation of the fracture network are presented in Sect. 4.2.1 and 4.2.2, respectively. The model domain is a rock slope with simplified topography. Warming steps are applied to the entire model domain without spatial differentiation.

### 4.2.1 Sensitivity to The influence of the slope angle on the numerical stability

The Figure 7 presents model results for exemplary slope inclinations between 60–64° are shown in Figure 7. Here, the block displacements increase and the related factors of safetyFS decrease with higher slope angles and temperatures below the melting point. When a rock slope with a slope angle of 62° or more is warmed up, the factor of safety falls below unity at temperatures above  $\geq -1$  °C when a rock slope with a slope angle of 62° or more is warmed up. A 60° steep rock slope becomes unstable at temperatures above  $\geq -0.5$  °C.



715

**Figure 7: Numerically calculated block displacements (on the log scale) for a simplified rock slope geometry with exemplary inclinations of 60°, 62° and 64°, and five temperatures between -4 and -0.5 °C.**

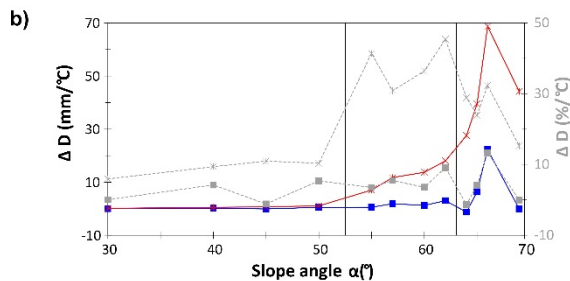
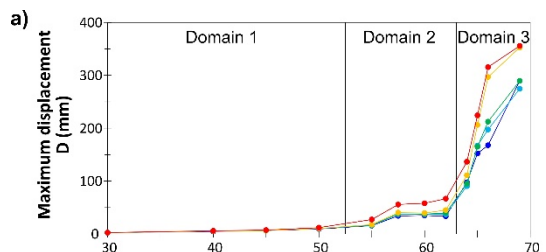
The ~~interaction relation~~ between slope gradient, maximum displacements and temperature can be separated into three domains (Fig. 8a):

- 1) Domain 1 (30 to 50°): The maximum displacements increase slightly by 0.4 mm per degree slope angle. The correlations for all temperatures are significant with p-values  $\leq 0.044\%$ .
- 2) Domain 2 (55 to 62°): Slope destabilisation sets in for rock slopes at -0.5 °C and above an inclination-slope angle of 50°. This becomes obvious due to the abrupt increase in displacements and the p-value  $> 0.055\%$ . For rock slopes at -1 °C and below, the onset of instability is visible above an inclination of 55°. Note that ~~a~~All displacements are one magnitude higher than in Domain 1.
- 3) Domain 3 (64 to 69°): The displacements increase suddenly ~~for all rock temperatures~~ with a further increase in higher-the p-values and a corresponding decrease in the R<sup>2</sup>-value for a slope angle of 64° and- for all rock temperatures. This points to a second stage of accelerating slope destabilisation. The displacements are one magnitude higher than in Domain 2.

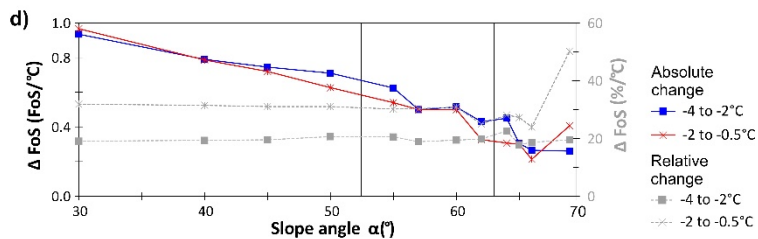
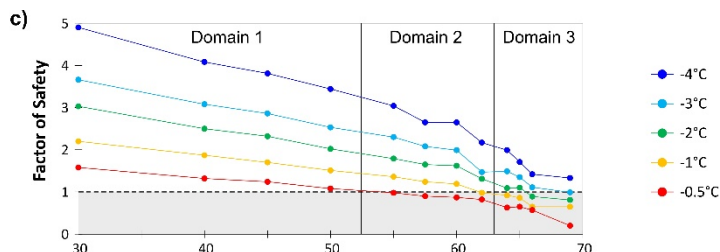
The displacements are sensitive to the sub-zero temperatures at all slope gradients. However, the intensity of rock slope destabilisation is increased by higher rock temperatures close to the melting point (Fig. 8b): A warming from -4 to -2 °C leads to an increase in absolute displacements, being low in Domain 1 (0.2 mm °C<sup>-1</sup>), but high in Domain 3 (7 mm °C<sup>-1</sup>). A respective warming from -2 to -0.5 °C shows also an increasing trend with higher slope gradients, but is more pronounced with a massive increase from Domain 1 (0.6 mm °C<sup>-1</sup>) to Domain 3 (45 mm °C<sup>-1</sup>). Nevertheless, the highest temperature-dependent relative increase in displacements is observed in Domain 2 (Fig. 8b): Values increase from 9.2 % °C<sup>-1</sup> (Domain 1) to 38.5 % °C<sup>-1</sup> (Domain 2) and fall to 25 % °C<sup>-1</sup> for slopes steeper than 62° (Domain 3), which is valid for a warming from -2 to -0.5 °C. Again, the same pattern is less pronounced for a warming from -4 to -2 °C.

Comparatively to the displacements, the factor of safety also depends on the slope angle and the temperature (Fig. 8c): For a rising steepness from 30 to 69°, the calculated FS decreases inversely and is always lower for higher temperatures. Warming from -4 to -0.5 °C reduces the FS of a permafrost rock slope by a mean factor of 3.3. The pattern of domains in Fig. 8a can be easily applied to the relation between FS, temperature and slope angle (Fig. 8c): The mean relative reduction of the FS per degree of the slope angle is low in Domain 1 (-1.8 % ± 0.4) and becomes higher over Domain 2 (-4.5 % ± 3.3), until it reaches a maximum in Domain 3 (-9.8 % ± 8.3). Correspondingly, rock slopes are stable for all modelled temperatures in Domain 1. When shifting to Domain 2, the FS falls below unity at -0.5 °C and at -1 °C which coincides with an abrupt increase in displacements. Rock slopes at -4 °C keep stable over the whole range of slope gradients.

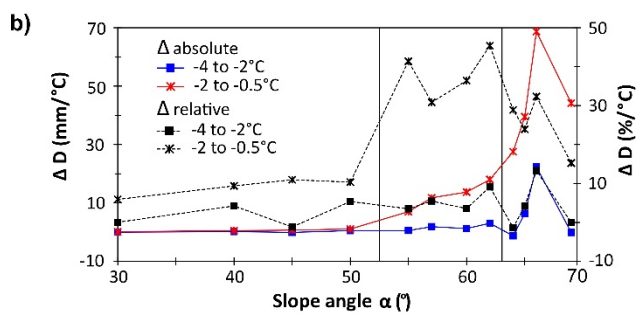
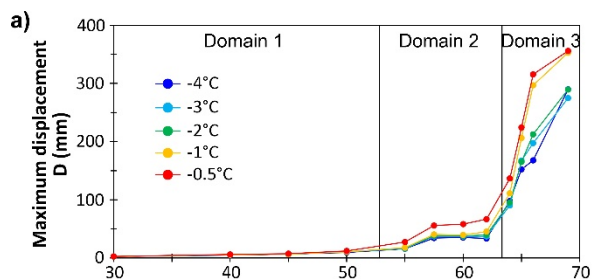
As we did for the maximum block displacements, we tested if warming closer to the melting point led to a distinct diminishing pattern of the FS (Fig. 8d): The absolute decrease is very similar for both warming steps from -4 to -2 °C and from -2 to -0.5 °C. However, the relative decrease from -4 to -2 °C is always lower than the one at higher temperatures.



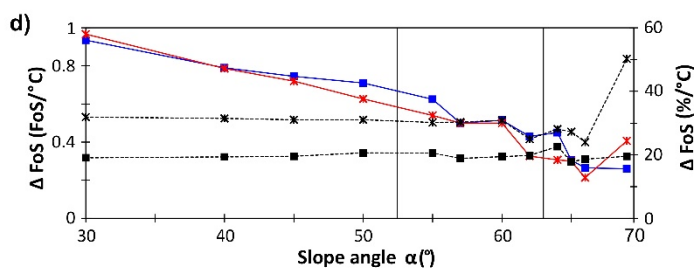
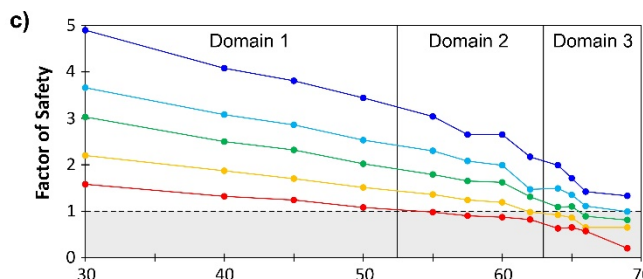
Domain	Relative change (% °C <sup>-1</sup> )		Absolute change (mm °C <sup>-1</sup> )	
	-2 to -0.5°C	-4 to -2°C	-2 to -0.5°C	-4 to -2°C
1	9.16	2.13	0.61	0.16
2	38.50	5.41	12.62	1.69
3	25.10	4.03	44.98	6.82



Domain	Relative change (% °C <sup>-1</sup> )		Absolute change (FoS °C <sup>-1</sup> )	
	-2 to -0.5°C	-4 to -2°C	-2 to -0.5°C	-4 to -2°C
1	31.36	19.66	0.78	0.80
2	29.07	19.67	0.47	0.52
3	32.40	19.67	0.31	0.32



Domain	Relative change (% °C <sup>-1</sup> )		Absolute change (mm °C <sup>-1</sup> )	
	-2 to -0.5°C	-4 to -2°C	-2 to -0.5°C	-4 to -2°C
1	9.2	2.1	0.6	0.2
2	38.5	5.4	12.6	1.7
3	25.1	4.0	45.0	6.8



Domain	Relative change (% °C <sup>-1</sup> )		Absolute change (FoS °C <sup>-1</sup> )	
	-2 to -0.5°C	-4 to -2°C	-2 to -0.5°C	-4 to -2°C
1	31.4	19.7	0.7	0.8
2	29.1	19.7	0.5	0.5
3	32.4	19.7	0.3	0.3



755 Figure 8 provides critical slope angles and rock temperatures beyond which instability is introduced. (a) Calculated maximum displacements against slope angle for temperatures between -4 and -0.5 °C. The curves are assigned to three distinct domains dependent on the slope gradient: Above 50°, and a second time above 62°, the curves show a sudden onset of instability. (b) Absolute and relative increase in displacements versus slope angle for a warming from -4 to -2 °C and from -2 to -0.5 °C. (c) Calculated factor of safety (FS) against slope angle for different sub-zero temperatures. (d) Absolute and relative decrease in FS versus slope angle for a warming from -4 to -2 °C and from -2 to -0.5 °C.

760

~~As could be demonstrated for the displacements, the factor of safety also depends on the slope angle and the temperature (Fig. 8e): For a rising steepness from 30 to 69°, the calculated FS decreases inversely and is always lower for higher temperatures. Warming from -4 to -0.5 °C reduces the FS of a permafrost rock slope by a mean factor of 3.3. The pattern of domains in Fig. 8a can be easily applied to the relation between FS, temperature and slope angle (Fig. 8c): The mean relative reduction of the FS per degree of the slope angle is low in Domain 1 (1.8 % ± 0.4) and becomes higher over Domain 2 (4.5 % ± 3.3), until it reaches a maximum in Domain 3 (9.8 % ± 8.3). Correspondingly, rock slopes are stable for all modelled temperatures in Domain 1. When shifting to Domain 2, the FS falls below unity at -0.5 °C and at -1 °C which coincides with an abrupt increase in displacements. Rock slopes at -4 °C keep stable over the whole range of slope gradients.~~

765

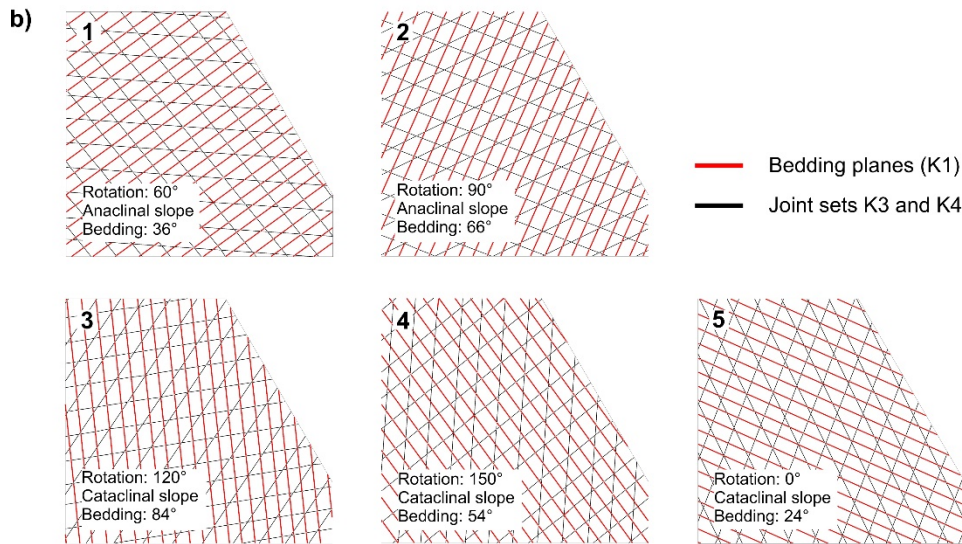
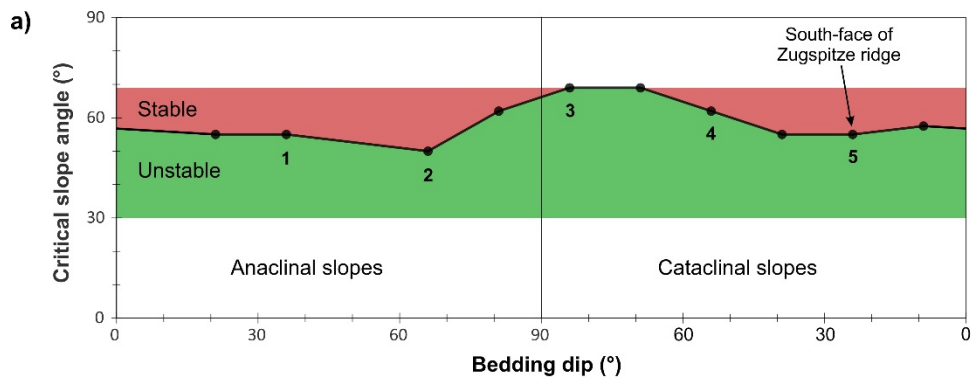
~~As we did for the maximum block displacements, we tested if warming closer to the melting point led to a distinct diminishing pattern of the FS (Fig. 8d): The absolute decrease is very similar for both warming steps from -4 to -2 °C and from -2 to -0.5 °C. However, the relative decrease from -4 to -2 °C is always lower than the one at higher temperatures.~~

770

#### 4.2.2 Sensitivity to ~~The influence of t~~ **the fracture network orientation on the numerical stability**

Modelling resulted in eight-8 out of 12 orientations of the fracture network that show a significant displacement acceleration and initiating slope instability above a critical slope inclination (Fig. 9a): For anaclinal slopes, the critical angles range between 50–62° and, for cataclinal slopes, they range between 55–62°. Cataclinal rock slopes with a bedding dip of 84 and 69° do not indicate a significant knickpoint in the displacement curves. As such, the corresponding critical slope angles were set to the maximum of the investigated values (69°). Fracture networks rotated counter-clockwise by 30° and 75° from the joint set of the Zugspitze summit crest showed very noisy model data and were not used for the analysis.

775



780

**Figure 9: (a) A rule-of-thumb for critical slope gradients and fracture network orientations of anacinal and cataclinal permafrost rock slopes. For cataclinal slopes, both the slope-face and the bedding have the same dip direction, but for anacinal slopes, the dips of both are oriented oppositely (Cruden, 2003). The green area refers to stable rock slopes while the red area refers to unstable ones. For simplification, the fracture network is represented by the bedding dip. The coloured areas indicate the studied range of slope angles. (b) Five exemplary joint set constellations for cataclinal and anacinal slopes with an inclination of 60°. The numbers of the rock slopes correspond to the numbers in (a). The joint spacing is ten-times bigger than in reality and is only applied for illustration. Example 5 refers to the Zugspitze summit crest.**

785

## 5 Discussion

790

This study successfully simulated the mechanical response of a warming and thawing permafrost rock slope using a temperature-dependent numerical model. The suggested modelling approach aims at supporting scientists and engineers in performing more accurate and realistic mechanical stability analyses by using temperature-corrected mechanical parameters



with a temperature-dependent spatial assignment. It can be used for any permafrost-affected rock slope across the globe which is subjected to climatic warming.

795 The numerical model for the Zugspitze summit ridge successfully simulates the strength reduction at warming and thawing which was able to be demonstrated in the laboratory tests of this and of previous studies (Table 1). Warming of ice-filled joints from  $-4$  to  $-0.5$  °C takes the slope close to a critical level of stability ( $FS = 1.25$ ). As soon as thawing sets in, the south face becomes massively destabilised as the displacements increase by two orders of magnitude and the factor of safety falls below 1. While the warming of ice-filled joints below  $-0.5$  °C does not initiate instability in the model, the ice loss at  $0$  °C can do it.  
800 Destabilisation is triggered by a slight reduction of the joint cohesion from  $0.18$  MPa (at  $-0.5$  °C) to  $0$  MPa (Table 5), even though the joint friction angle is increased from  $13.5$  to  $29.3$ °.

Further, we show that destabilisation of a permafrost rock slope with ice-filled joints, a fracture network and rock/joint properties similar to the Zugspitze south face can be initiated at a slope gradient  $> 50$  or  $55$ ° (Domain 2 in Fig. 8: “First onset of instability”) and significantly favoured above a gradient  $> 62$ ° (Domain 3 in Fig. 8: “Accelerating slope destabilisation”).  
805 The transition from Domain 1 (Fig. 8: “Displacements increase slightly with the slope angle”) to Domain 2 seems to be the most critical in terms of slope destabilisation, as it is characterised by the highest relative increase in displacements per degree of the slope angle. Interestingly, this could be confirmed by the study of the critical slope angle for varying orientations of the fracture network (Fig. 9):  $50$  % of the studied orientations have a critical slope angle of  $50$  or  $55$ °, which corresponds to the transition from Domain 1 to Domain 2.  $30$  % of the orientations lead to instability with angles of between  $57.5$ – $62$ °, and  $20$  %  
810 remain stable within the studied range of slope gradients.

The proposed procedure and the derived critical thresholds present useful tools to assess the stability of degrading permafrost rock slopes potentially endangering human life and mountain infrastructure. The critical stability thresholds regarding the slope angle, fracture network orientation and bedrock temperature can be used to detect high mountain rock slopes which are susceptible to fail in the future. However, a prerequisite is to have data on the fracture network and the thermal field of the  
815 rock slope under investigation. Even more a detailed stability assessment requires a number of site-specific input data, which is not realisable for a quick analysis of a current failure event.

The following sections ~~provide a discussions on the~~discusses show the general limitations of the presented models (Sect. 5.1) and critically discuss ~~on the numerical results of the~~ site specific model (Sect. 5.2.1) and ~~the model of the simplified generalised permafrost rock slope (Sect. 5.3.2) and its transferability to other high mountain conditions. Finally After that, we~~ discuss if the limitations of the presented models (Sect 5.3) and if they can be transferred to other field sites in the Alps (Sect. 5.4).

## 5.13 Limitations and potential error sources

### 5.13.1 Material parameters

Mechanical models are often sensitive to material parameters. However, the availability of these parameters and the technical opportunities to establish them are limited. Therefore, the presented mechanical model of the Zugspitze summit crest bases on a few ~~two main~~ simplifications. First, ~~Potential effects upon freezing, which can~~ Freezing effects that act to increase the rock mass strength, are mostly ignored in the GSI rock mass classification system. ~~On the one hand,~~ it is crucial to consider the temperature dependency of the material parameters as freezing ~~effects for example~~ can increase rock mass strength ~~(add ref)~~. However, the influence of freezing effects is mostly ignored in the GSI rock mass classification system (see also Gambino and Harrison, 2017). In our model, ~~t~~For instance, the suggested determination of ~~t~~The friction angle after Cai et al. (2004; Fig. 5) is based on ~~applies~~ the temperature-independent Hoek-Brown constant  $m_i$  and the GSI value, which could only be defined for the unfrozen rock mass currently exposed at the surface of the rock slope. As such, the unfrozen internal friction value had to be assigned to both the frozen and the unfrozen rock mass. ~~To our knowledge, the friction angle of a frozen rock mass and its change due to thawing is hardly investigated and not yet described by a general law. Model test runs with very low to unrealistically high values of the mechanical rock mass properties demonstrated that the displacements in the rock slope mostly remained within the same order of magnitude (Fig. S9). Therefore, the rock mass internal friction angle was derived due to the GSI scheme, and its unfrozen value was assigned to both the frozen and the unfrozen rock mass. This assumption ... Erläutern~~ ~~weshalb dies ok ist!~~ Second, ~~On the other hand,~~ the knowledge of the subsurface structure (i.e. joint spacing and joint persistence) is limited, and has to be estimated due to inspection of the rock surface. Third, mechanical parameters were not determined for the specific ~~j~~Further, ~~j~~Joint sets. Only specific parameters were not available for the Zugspitze summit crest, except for the joint normal and shear stiffness varied between the joint sets due to ~~, which varied due to their~~ different joint spacing (Eq. (6) and Eq. (7)).

~~To our knowledge, a~~Fourth~~urthermore,~~ a standardised recommendation of how to set for the disturbance factor  $D$  for an unstable rock slope (without blast damage) does not exist; such a recommendation should be validated numerically and include a classification of various degrees of instability. Therefore,  $D$  was ~~s~~et to 0, ~~as any other value seemed to be arbitrary. However,~~ but the potential influence of a higher  $D$  on the slope stability was analysed due to additional model runs with the geometry of the Zugspitze crest (Fig. S69); ~~a modified the model results showed that setting~~  $D$  ~~t~~approaching 1 leads to higher displacements but the factor of safety remains unchanged.

We acknowledge that the presented model of the Zugspitze summit crest is simplified and limited by the knowledge of the subsurface structure (i.e. joint spacing and joint persistence) and exact permafrost dimension. Especially the ~~and~~ material parameters of the rock mass had to be ~~were~~ estimated on basis of laboratory results. Even if the neglect ~~K2~~ is in accordance with present standard routines. For future models, we recommend developing studies in future ~~3D models could also to account for the missing joint set K2 and to provide a would even better impression of~~ represent the kinematic behaviour of the rock

855 slope. Further, we suggest to perform a detailed sensitivity analysis of the implemented material parameters in the future, which is beyond the scope of this paper.

### 5.13.2 Numerical model

Furthermore, the implementation of the numerical model implies a few limitations which are addressed with the following approaches:

860 - When implementing non-persistent joints, UDEC discards those which do not split a block. An irregular joint and block pattern may be formed which does not correspond to reality. Therefore, discontinuities were constructed fully persistent, but the joint strength parameters were increased according to the first model stages (following Jennings (-1970) to omit the potential result of favoured higher displacements and velocities along persistent joints. This approach enables to implement non-persistent joints as UDEC discards those which do not split a block

865 - The size of the Zugspitze model domain was constrained to a local section of the rock slope ending in a steep part at the south-face. By this, the model domain fully incorporates the unstable rock mass under investigation, and thereby perfectly accounts for the simulated spatial conditions of the rock-ice-mechanical processes we want to simulate. However, a cross section ending with a flatter slope angle can potentially lead to different model results. To account for this, we rerun the model with a bigger domain size ending in a flatter section of the south-slope (Fig. S69): the results demonstrated that a change in the size of the model domain does not significantly change the overall stability of the slope.

870 — The initial temperature of the frozen rock slope does not affect the displacement magnitudes and the general pattern of dependency between maximum displacements and slope inclination. The potential effect influence of a lower strength on the calculation of the

875 initial strength-equilibrium and on the resulting on the maximum displacement values was proven by reiterating the generalised model with an initial temperatures at -4 °C and -2 °C and comparing it with the original -4 °C (Fig. S7). All model runs for the sensitivity analysis were started with a frozen rock slope at a temperature of -4 °C. However, if the warming of ice-filled joints is started at a temperature higher than -4 °C, model results may be different as material parameters with a lower strength have been assigned for the calculation of the initial equilibrium. To test this potential effect, we reiterated the same model and started warming at -2 °C. However, the same general pattern of dependency between maximum displacements and slope inclination could be identified (Fig. S10). Furthermore, the displacement magnitudes for both model options did not differ either.

880 — We acknowledge that the spatial warming pattern for the Zugspitze model is simplified and based on a static temperature field derived from ERT, rock thermistors and published thermal models (Böckli et al., 2011; Noetzli et al., 2007; Noetzli, 2008). For the future, we recommend developing a heat flow model of the crest for different time

885

steps to better assess the warming pattern for the coupled model. However, this is clearly beyond the scope of this article.

- Warming to the next degree centigrade was, by default, calculated with 3000 cycles which was a compromise between a representative number of cycles for potentially reaching a numerical equilibrium (for stable rock slopes), and a reasonable, not too time-consuming calculation. The number of calculated cycles for each warming step influences the available time for the rock slope to react to a change in stress-strain due to a modification of material parameters. The warming to the next degree centigrade was, by default, calculated with 3000 cycles. This was a compromise between a representative number of cycles for potentially reaching a numerical equilibrium (for stable rock slopes), and a reasonable, not too time-consuming calculation. Computations for low/intermediate slope angles and temperatures reached an equilibrium prior to 3000 cycles, whereas calculations for higher slope angles and temperatures mostly failed to reach an equilibrium (for unstable rock slopes) or scarcely they required > more than 3000 cycles. Hence, the numerical calculation was repeated with warming steps with 6000 cycles (To prevent a potential cut-off effect of cycles required for the rock slope to react to a change in stress-strain due to a modification of material parameters that are relevant for a realistic stability analysis, all the calculation steps were repeated with a higher number of 6000 cycles. However, the results coincide well with the The corresponding results show a very similar pattern as for the model runs with 3000 cycles since (Fig. S11): (i) A significant acceleration of displacements significantly accelerate above slope angles above of 5-50° and above 62°, and (ii) higher displacements they are higher for temperatures closer to the melting point. (Fig. S8). The test confirms the reliability of the chosen number of cycles for each warming step.

The spacing was set five times greater than in reality (Table 2) due to computational limits defined by UDEC. By doing this, reasonable computation times were achieved and the model still reproduced slope conditions close to reality. Nevertheless, we expect displacements to increase slightly as was shown by Gischig et al. (2011a), and which is an obvious effect due to a reduced rock mass strength (Cai et al., 2004; Fig. 7). Though, the comparability among all calculated model stages was not affected by the larger joint spacing as it was kept constant for all calculations.

The discontinuities were constructed fully persistent, although block displacements may have been favoured and velocities augmented along persistent joints. However, when implementing non-persistent joints, UDEC discards those which do not split a block. An irregular joint and block pattern may be formed which does not correspond to reality. To omit the potential result of favoured higher displacements and velocities, the joint strength parameters were increased in the first model stages following Jennings (1970).

To keep this first version of a thermo-mechanically coupled model as simple as possible, the numerical representation of the advanced stage of rock slope destabilisation was reduced to (i) the fracturing of ice and rock-ice contacts along frozen joints and (ii) the frictional strength of rock-rock contacts along thawed joints. Future model codes should also include the preceding creep of ice at lower displacement rates.

920 **5.21 The stability-Stability assessment of the warming/thawing Zugspitze summit crest based on the Factor of Safety**

~~The numerical model for the Zugspitze summit ridge successfully-simulates the strength reduction at warming and thawing which was able to be demonstrated in the based on laboratory tests of this and of previous studies (Table 1). Warming of ice-filled joints takes the slope close to a critical level of stability (FS = 1.3), but it does not initiate instability. As soon as thawing sets in and the ice is lost, the south-face becomes massively destabilised as displacements increase by two orders of magnitude~~

925 ~~and the factor of safety falls below unity. Destabilisation is triggered by a slight reduction of the joint cohesion from 0.18 MPa (at -0.5 °C) to 0 MPa (Table 5), even though the joint friction angle is increased from 13.5 to 29.3°.~~

~~Davies et al. (2001) postulate that the FS factor of safety of a permafrost affected rock slope is higher for unfrozen joints than for ice-filled joints between approximately -1.5 °C and zero degrees. In contrast to that, our numerical analysis of the thawing Zugspitze summit crest shows that many ice-filled fractures reach a minimum stability only upon thaw. This is indicated by~~

930 ~~the sudden and massive increase in displacements and the factor of safety falling below unity. The reduction in joint stability is significantly influenced by a related loss of the joint cohesion. The differing observations on the stability upon thaw may be explained as follows: (i) Our model assumes a lower joint roughness and uses the residual friction angle which is lower than the peak friction angle taken for the centrifuge model. We suppose that the simulated rock slope has already been moving for~~

935 ~~a long time and joint surfaces are flattened due to the progressive destruction of asperities along joints. In contrast, the sliding surface in the centrifuge model is not affected by any previous displacements. (ii) The calculated FS by Davies et al. (2001) corresponds to an independent moment in time, while the FS in the Zugspitze model is path-dependent and affected by the history of the previous numerical calculations.~~

~~The mean annual air temperature (MAAT) at the Zugspitze peak from 1991 to 2019 was -3.9 °C. It was 0.8-1.1 °C warmer than the three means of the prior 30 year reference periods between 1901 and 1990 (CDC FTP Server, Deutscher~~

940 ~~Wetterdienst). A model for the permafrost evolution at the Zugspitze peak by Galleman et al. (2017) shows that between 1915 and 2015 the permafrost decreased by 2 m at the north face and by 7 m at the south face, with an increase in the permafrost temperature of approximately 1 °C. The permafrost evolution model by Galleman et al. (2017) predicts permafrost~~

~~at the Zugspitze peak to be lost within the second half of the 21<sup>st</sup> century which may result in an elevated occurrence of rock slope instability. This scenario is related to a projected increase in~~

945 ~~Until the end of this century, the mean air temperature at the Zugspitze peak is projected to increase by 3.2 °C until the end of the century. Stages 11 to 15 of the mechanical model represent the same time period (current state until second half of the century) and simulate, which can result in a total loss of~~

~~permafrost at the Zugspitze summit (and the field site of this study) within the second half of the century (Galleman et al., 2017). The corresponding scenario is represented by progressive thawing of the summit crest that leads to the continuation of~~

950 ~~increasing displacements and the preparation of final slope failure the last model stage 15 (Fig. 6f). Promoted by progressive thawing of the summit crest between the current state (Stage 11) and the second half of the century (Stage 15), the thermo-mechanical model predicts an ongoing increase in displacements which can prepare final slope failure.~~

The factors of safety for all stages with one or more thawed rock layers, including the current extent of permafrost (Stage 11, Fig. 6e), lie below unity which indicates slope instability. This is consistent with the observations of the current displacements and characteristics of the main shear zone at the field site. However, the high values calculated by the model are not comparable with the measured displacement rates at the field site ( $52.0\text{--}1\text{ mm y}^{-1}$ ) for the following reasons: (i) The numerically calculated displacements are maximum values and refer to local sections in the model. (ii) Cycling in UDEC was not linked to specific time-steps. As such, we could not assign specific periods of time to the distinct, non-linear steps of warming or thawing. This did not permit us to estimate the approximate time period required for the calculated displacements to occur. (iii) Absolute displacements are path-dependent and affected by the history of calculations, including input and alteration of parameters as well as the stress-strain behaviour in the system.

~~Davies et al. (2001) postulate that the factor of safety of a permafrost affected rock slope is higher for unfrozen joints than for ice filled joints between approximately  $1.5\text{ }^{\circ}\text{C}$  and zero degrees. In contrast to that, our numerical analysis of the thawing Zugspitze summit crest shows that many ice filled fractures reach a minimum stability only upon thaw. This is indicated by the sudden and massive increase in displacements and the factor of safety falling below unity. The reduction in joint stability is significantly influenced by a related loss of the joint cohesion. The differing observations on the stability upon thaw may be explained as follows: (i) Our model assumes a lower joint roughness and uses the residual friction angle which is lower than the peak friction angle taken for the centrifuge model. We suppose that the simulated rock slope has already been moving for a long time and joint surfaces are flattened due to the progressive destruction of asperities along joints. In contrast, the sliding surface in the centrifuge model is not affected by any previous displacements. (ii) The calculated FS by Davies et al. (2001) corresponds to an independent moment in time, while the FS in the Zugspitze model is path dependent and affected by the history of the previous numerical calculations. This procedure simulates “step path” failure on the slope scale in a simplified way which is characterised by the interconnection of pre existing, adjacent discontinuities through intact rock bridges (Camones et al., 2013; Eberhardt et al., 2004; Huang et al., 2015). The reduction in the shear strength involves processes of stress concentration, crack initiation, crack propagation and coalescence, slip weakening and the formation of a continuous failure plane or zone (Zhang et al., 2015), which were not numerically modelled as this would be beyond the scope of this study. The presented model of the Zugspitze ridge considers crack coalescence to occur by shear and tensile mode or a tensile-shear combination, which has been observed on the micro scale by Zhang and Wong (2013). The resulting new connections can form coplanar or oblique to the pre-existing joints (Huang et al., 2015). At the scale of the Zugspitze ridge, we assume the joint sets K1, K3 and K4 to link in both coplanar and oblique form, leading to the formation of straight or stepped failure planes.~~

Based on the 3D kinematic analysis (Sect. 2.1.23), we postulate that the most likely mechanism controlling the slope instability is a combination of a plane and a wedge failure. However, for the 2D numerical model and at the scale of the failure plane, we consider various possible complex mechanisms: (i) Sliding of several rock blocks along a polygonal shear zone SZ1/SZ4 that is constituted by joint sets K1, K3 and K4. This complex type of failure is provided by antithetic fractures which enable shear

displacements between the moving blocks (Eberhardt et al., 2004; Poisel ~~and~~ Preh, 2004). (ii) Shear or tensile failure along joint sets K3 or K4 may favour shear displacements along K1 by supplying additional stress onto the blocks and inducing “step-path” failure (Huang et al., 2015; Mejía Camones Camones et al., 2013; Huang et al., 2015). (iii) Failure at the scale of single blocks can be induced by forward block toppling with K1 and K3 or backward block toppling with K1 and K4 (Itasca Consulting Group, 2019). Both options will only work for higher columns subdivided by surfaces of K1 which stick together due to locally higher frictional or cohesive strength. (iv)

The two joint sets K1 and K4, ~~which daylight in the south face,~~ favour the displacements to concentrate on the south-face. Its slope aspect. However, the highest deformations concentrate on the lower slope section with a mean gradient of 49°, but they are not coupled to the prominent shear zone. ~~Instead they concentrate on the lower slope section with a mean gradient of 49°.~~ This can be the result of (i) the dominating influence of the slope angle on the stability of the system and (ii) the lack of variation in the joint properties of the shear zone and the remaining joint sets (Table 5).

### **5.32 The stability of a simplified permafrost rock slope with rising temperature**

The destabilisation of a permafrost rock slope with ice-filled joints and a fracture network and rock/joint properties similar to the Zugspitze south-face can be initiated at a slope gradient > 50 or 55° (Domain 2 in Fig. 8: “First onset of instability”) and significantly favoured above a gradient > 62° (Domain 3 in Fig. 8: “Accelerating slope destabilisation”). The transition from Domain 1 (Fig. 8: “Displacements increase slightly with the slope angle”) to Domain 2 seems to be the most critical in terms of slope destabilisation, as it is characterised by the highest relative increase in displacements per degree of the slope angle. Interestingly, this could be confirmed by the study of the critical slope angle for varying orientations of the fracture network (Fig. 9): 50 % of the studied orientations have a critical slope angle of 50 or 55°, which corresponds to the transition from Domain 1 to Domain 2. 30 % of the orientations lead to instability with angles of between 57.5–62°, and 20 % remain stable within the studied range of slope gradients.

The relevance of slope angles at the described transition from Domain 1 to Domain 2 (Fig. 8), identified by the numerical model, is in accordance with documented rock slope failures in the Swiss Alps, adjacent areas in France and Italy (Fischer et al., 2012) and in the Mont Blanc Massif (Ravel et al., 2010), which are mostly attributed to the degradation of bedrock permafrost: The mean slope gradient of the detachment zones in the Mont Blanc Massif was 54°, while the highest percentage of detachment zones in the Swiss Alps and adjacent areas had slope angles of between 40–60°, leading to a postulated lower slope gradient threshold of 40–45° for rock slope failures.

We further demonstrate that the factor of safety falls below 1 when a rock slope with a gradient  $\geq 50^\circ$  is warmed from  $-4^\circ\text{C}$  to a temperature between  $-3$  and  $-0.5^\circ\text{C}$ . This sensitive temperature range corresponds well to (i) the temperatures currently monitored in boreholes in permafrost rock walls in the European Alps (Gallemann et al., 2017; Noetzli et al., 2019) and (ii) the temperatures which are characteristic for warm permafrost areas or the lower permafrost boundary ( $-5$  to  $0^\circ\text{C}$ ). The latter posed the release zones for most of the rock slope failure events documented by Fischer et al. (2012) and Ravel et al. (2010).



1020 The model results also demonstrate that the increase in displacements becomes more pronounced when approaching the melting point which indicates a non-linear relation (Fig. 8b): the relative and the absolute increase are always higher for a warming from -2 to -0.5 °C than for a warming from -4 to -2 °C. The relation between rising subzero temperature and reduced stability was also observed by Davies et al. (2000, 2001). However, on the basis of our model results, we propose to complement the conclusions by Davies et al. (2001) in the following way: (i) The temperature of critical stability is highly dependent on the inclination of the main fractures versus the slope angle. (ii) It is of crucial importance to consider the stress conditions in a rock slope when extrapolating the results from the laboratory scale to the field scale. (iii) The use of rock instead of concrete samples for the laboratory determination of joint parameters results in a closer reproduction of the real conditions along rock joints in the field.

### ~~5.3 Limitations and potential error sources~~

#### ~~5.3.1 Material parameters~~

1030 ~~Potential effects upon freezing, which can increase the rock mass strength, are mostly ignored in the GSI rock mass classification system. For instance, the suggested determination of the friction angle after Cai et al. (2004; Fig. 5) is based on the temperature independent Hoek-Brown constant  $m$ , and the GSI value, which could only be defined for the unfrozen rock mass currently exposed at the surface of the rock slope. As such, the unfrozen internal friction value had to be assigned to both the frozen and the unfrozen rock mass. Further, joint set specific parameters were not available, except for the joint normal and shear stiffness, which varied due to the different joint spacing (Eq. (6) and Eq. (7)).~~

1035 ~~We acknowledge that the presented model of the Zugspitze summit crest is simplified and limited by the knowledge of the subsurface structure (i.e. joint spacing and joint persistence) and exact permafrost dimension. Especially the material parameters of the rock mass had to be estimated. For future models, we recommend developing studies in 3D to account for the missing joint set K2 and to provide a better impression of the kinematic behaviour of the rock slope. Further, we suggest to perform a detailed sensitivity analysis of the implemented material parameters in the future, which is beyond the scope of this paper.~~

#### ~~5.3.2 Numerical model~~

1040 ~~All model runs for the sensitivity analysis were started with a frozen rock slope at a temperature of -4 °C. However, if the warming of ice-filled joints is started at a temperature higher than -4 °C, model results may be different as material parameters with a lower strength have been assigned for the calculation of the initial equilibrium. To test this potential effect, we reiterated the same model and started warming at -2 °C. However, the same general pattern of dependency between maximum displacements and slope inclination could be identified (Fig. S9). Furthermore, the displacement magnitudes for both model options did not differ either.~~

~~We acknowledge that the spatial warming pattern for the Zugspitze model is simplified and based on a static temperature field derived from ERT, rock thermistors and published thermal models (Böckli et al., 2011; Noetzli et al., 2007; Noetzli, 2008). For the future, we recommend developing a heat flow model of the crest for different time steps to better assess the warming pattern for the coupled model. However, this is clearly beyond the scope of this article.~~

~~The number of calculated cycles for each warming step influences the available time for the rock slope to react to a change in stress-strain due to a modification of material parameters. The warming to the next degree centigrade was, by default, calculated with 3000 cycles. This was a compromise between a representative number of cycles for potentially reaching a numerical equilibrium (for stable rock slopes), and a reasonable, not too time-consuming calculation. Computations for low/intermediate slope angles and temperatures reached an equilibrium prior to 3000 cycles, whereas calculations for higher slope angles and temperatures mostly failed to reach an equilibrium (for unstable rock slopes) or scarcely they required more than 3000 cycles. To prevent a potential cut off effect of cycles that are relevant for a realistic stability analysis, all the calculation steps were repeated with a higher number of 6000 cycles. The corresponding results show a very similar pattern as for the model runs with 3000 cycles (Fig. S10): (i) A significant acceleration of displacements above 50 and above 62° and (ii) higher displacements for temperatures closer to the melting point. The test confirms the reliability of the chosen number of cycles for each warming step.~~

~~The spacing was set five times greater than in reality (Table 2) due to computational limits defined by UDEC. By doing this, reasonable computation times were achieved and the model still reproduced slope conditions close to reality. Nevertheless, we expect displacements to increase slightly as was shown by Gischig et al. (2011a), and which is an obvious effect due to a reduced rock mass strength (Cai et al., 2004; Fig. 7). Though, the comparability among all calculated model stages was not affected by the larger joint spacing as it was kept constant for all calculations.~~

~~The discontinuities were constructed fully persistent, although block displacements may have been favoured and velocities augmented along persistent joints. However, when implementing non persistent joints, UDEC discards those which do not split a block. An irregular joint and block pattern may be formed which does not correspond to reality. To omit the potential result of favoured higher displacements and velocities, the joint strength parameters were increased in the first model stages following Jennings (1970).~~

~~To keep this first version of a thermo-mechanically coupled model as simple as possible, the numerical representation of the advanced stage of rock slope destabilisation was reduced to (i) the fracturing of ice and rock-ice contacts along frozen joints and (ii) the frictional strength of rock-rock contacts along thawed joints. Future model codes should also include the preceding creep of ice at lower displacement rates.~~

#### 5.4 Transferability and implications for other field sites

The general procedure for a ~~temperature-dependent combined thermo-~~mechanical stability model (Fig. 1) can be applied to any warming or thawing permafrost rock slope. However, the results of the sensitivity analysis with input data from the Zugspitze summit ridge (Sect. 4.2) are valid for rock slopes with increasing subzero temperatures, consisting of fractured

limestone, with strength and deformability similar to the Wetterstein limestone tested in this study. A transfer to permafrost rock slopes with a different lithology is possible, but it requires more laboratory calibration tests and modelling. A provisional transfer may be possible with the following justification:

Mamot et al. (2018, 2020) studied the shear strength of ice-filled permafrost rock joints and developed a resilient temperature- and stress-dependent failure criterion. ~~They postulate that it can be transferred which is valid to~~ for the majority of the rocks that are relevant for observed permafrost rock slope failures in the Alps. Since this failure criterion was used to calculate the cohesion and the friction of the ice-filled joints in the presented model, the numerical description of them may be applied to other lithologies, too. However, the joint stiffness and the mechanical parameters of the rock mass still vary among different rock types and may lead to different model results. To get a first impression of this potential effect, we performed a couple of model test runs with varying values for the mechanical properties of the rock mass ranging from very low to unrealistically high. As the displacements remained within the same order of magnitude (Fig. S12S9), we infer that the model results will not be significantly influenced by other rock types with distinct properties of strength and deformability. Nevertheless, we strongly recommend to verify the effect of different rock types by thorough modelling in the future.

~~The transferability of the numerical results is also limited. Hence, the results can only be applied to rock slopes with a similar joint set configuration as in this article. since FurtherNote, it is important to consider that the rule-of-thumb for critical slope angles and fracture network orientations results in~~ (Fig. 9) ~~is~~ valid for a specific constellation of three joint sets and not only for the bedding, as presented by Cruden (2003). ~~Hence, the results can only be applied to rock slopes with a similar joint set configuration as in this article.~~

Considering the constraints above, the simplified model, developed by the sensitivity analysis (Sect. 4.2), can be transferred to warming permafrost rock slopes with ice-filled discontinuities and slope gradients smaller than 70°. In addition, these rock slopes consist of limestone (and probably mostly all rock types relevant for permafrost rock slope failures in the Alps), and they contain three joint sets separated from each other by an angle of 45°.

## 6 Conclusion

~~This study presents. The warming climate in high mountains is expected to lead to a higher number of rock slope failures influenced by progressive permafrost loss (Gobiet et al., 2014; Huggel et al., 2012). To tackle the challenge of assessing the stability of degrading permafrost rock slopes in a warming climate, we need to understand how rock ice mechanical components control rock slope destabilisation and how failure close to melting, and at thawing, can be mechanically expressed in models. For this, we have developed~~ the first numerical model which is capable of supporting scientists and engineers in performing more accurate and realistic performing a comprehensive mechanical stability analyses of degrading warming or thawing permafrost rock slopes.

In this context, we provide (i) a universal procedure for the input of thermal and mechanical data, the model setup and the modelling strategy, (ii) a numerical benchmark application to a specific test site at the Zugspitze peak, and (iii) the first numerically derived critical stability thresholds related to the slope angle, rock mass temperature, slope angle and orientation of the fracture network. The related main findings are summarised as follows:

(i) The proposed approach instruction for the set up of a temperature-dependent coupled thermo-mechanical stability model (Figure 6.1) can be used for any permafrost-affected rock slope across the globe which is subjected to climatic warming.

(ii) Laboratory tests and field reconnaissance of the However, it requires a number of various input data which are to be collected in the field and in the laboratory. The numerical modelling approach was successfully applied to the permafrost affected benchmark site Zugspitze summit ridge : we used rock specimens picked from the provided exemplify thermal, geometrical and mechanical input data for the numerical model.

Frozen and unfrozen bedrock material properties were assigned to specific sections in the model and changed due to warming/thawing. Zugspitze summit area and performed a large number of mechanical laboratory tests on various frozen and unfrozen intact rock and rock joint properties. Intact rock properties were converted to rock mass characteristics using internationally standardised mathematical equations. The topography of the crest, the dimensions of the unstable rock mass, the potential failure mechanism, large scale shear zones and the geometrical properties of the fracture network, fracture displacements as well as mechanical rock mass and rock joint properties were determined due to geotechnical methods (mapping of the fracture network, Schmidt hammer, Barton comb, digital tape extensometer) and UAV-based photogrammetry. ERT and logging of near surface rock temperatures were applied to identify current frozen and unfrozen slope sections, to assign frozen or unfrozen rock mass and joint parameters to the corresponding model sections and to derive a rough spatial warming pattern. The modelling procedure was divided into three principal stages: rock bridge destruction, warming with ice-filled joints, and thawing. Since process-specific and temperature-dependent input parameters were modified when switching from one stage to the next, the Mohr-Coulomb plasticity constitutive model is capable of accounting for all processes which act during destabilisation.

(iii)

The Zugspitze model demonstrates that the The Zugspitze model demonstrates a stability factor of safety decreases decrease towards to a critical level of stability when as a result of (a) rock bridge break destruction and (b) gradual warming thermal degradation of frozen rock and ice-filled joints s gradually war mechanical properties from -4 to -0.5 °C.

Surficial Rock slope failure is introduced upon starts coincident to thawing of the outermost rock layer as the factor of safety falls below 1.

1145 (iv) Upon full thaw of the summit crest, expected within the next five5 decades, ~~t~~The Zugspitze model predicts an increase in displacements which upon full thaw of the summit crest potentially leading to final slope failure. This thermal scenario Permafrost at the Zugspitze summit is expected projected for the Zugspitze summit within to be completely lost within the second half of the century as a result of climatic warming (Galleman et al., 2017). ~~The Zugspitze model predicts an increase in displacements upon full thaw of the summit crest potentially leading to final slope failure.~~

1150 (v) We developed a framework to generalise and upscale the Zugspitze model: (iii) ~~C~~The critical stability thresholds were calculated in the context of a sensitivity analysis of the Zugspitze model with a simplified geometry and warming pattern.

1155 (vi) The dependence between instability and the slope angle can be classified into a stable first domain ( $\leq 50^\circ$ ), a second domain with a first onset of instability ( $55\text{--}62^\circ$ ), and a third domain characterised by an accelerated slope destabilisation ( $\geq 64^\circ$ ). The greatest relative increase in displacements is observed in the second domain.

— Warming from  $-4^\circ\text{C}$  to a temperature between  $-3$  and  $-0.5^\circ\text{C}$  initiates instability for rock slopes  $\geq 50^\circ$ .

1160 (vii) ~~The simplified model demonstrates that the displacements increase with the slope angle and the factor of safety decreases inversely. Rock slope failure is initiated at slope angles of greater than  $50^\circ$  and is even more intense above a slope gradient of  $62^\circ$ . Destabilisation is more pronounced for warming closer to the melting point (from  $-2$  to  $-0.5^\circ\text{C}$ ) than for warming from  $-4$  to  $-2^\circ\text{C}$ . This difference becomes greatest in the second domain.~~

— For anacinal slopes, the critical slope angles range between  $50\text{--}62^\circ$ , and for cataclinal slopes, they range between  $55\text{--}62^\circ$ .

(viii)

1165 (ix) ~~The critical slope angle varies between  $50$  and  $62^\circ$  depending on the orientation of the fracture network versus the slope face. Further, the generalised model shows that warming from  $-4^\circ\text{C}$  to a temperature between  $-3$  and  $-0.5^\circ\text{C}$  initiates rock slope instability for rock slopes  $\geq 50^\circ$ . The increase in displacements intensifies closer to the melting point. These calculated critical slope angles and rock mass temperatures results correspond well to the characteristics of documented rock slope failures in permafrost areas in the European Alps, which often showed large amounts of residual ice in their scars.~~

— ~~inventories of rock slope failures in permafrost areas in the European Alps.~~

1170 ~~Further, the generalised model shows that warming from  $-4^\circ\text{C}$  to a temperature between  $-3$  and  $-0.5^\circ\text{C}$  initiates rock slope instability for rock slopes  $\geq 50^\circ$ . The increase in displacements intensifies closer to the melting point. The identified sensitive temperature range between  $-3$  and  $-0.5^\circ\text{C}$  is consistent with the one currently measured in boreholes in permafrost rock walls across the European Alps; further, it is characteristic for warm permafrost areas which involve the release zones for most of the failure events documented in the Swiss, Italian and French Alps.~~

1175 — ~~The derived critical thresholds can be applied to warming permafrost rock slopes with (a) ice-filled joints, (b) limestone equivalent to Wetterstein limestone, or probably most of the rock types relevant for permafrost rock slope~~

180 failure in the Alps, (c) slope angles smaller than 70° and (d) various orientations of the fracture network consisting of three joint sets.

(x) \_\_\_\_\_

185 (xi) The critical thresholds can be used to detect rock slopes which are susceptible to fail in the future and potentially endanger human life and mountain infrastructure. For this, it is a prerequisite to have data on the fracture network, lithology, geometry and the thermal field of the investigated rock slopes. In contrast, a detailed stability assessment of a single rock slope requires a number of further site-specific input data.

190 We are at the beginning of developing numerical models for the mechanical response of a rock mass to warming/thawing. Therefore, there is a huge potential for improvements. For instance, more mechanical laboratory tests are necessary to improve process understanding and to extend the number of frozen and unfrozen material parameters for modelling. Future numerical models should be based on further sensitivity analyses, or include water pressure or the creep of ice at lower displacement rates within the advanced stage of rock slope destabilisation. Time-dependent cycling is not yet implemented in most of the numerical models, neither it is in the presented ones. Hence, they are not suited to forecast a precise time of rock slope failure. Further, the spatial warming pattern for the Zugspitze model is simplified and based on a static temperature field derived from ERT, rock thermistors and published thermal models. For a more accurate characterisation of the warming pattern, future mechanical models should include a subsurface temperature field based on a combination of geophysics and a heat flow model for different time steps.

195 Further modelling and laboratory tests are required to complete this first approximation of an application to other field sites. Considering the constraints above, the critical stability thresholds in terms of the slope angle, fracture network orientation and bedrock temperature can be used to detect high mountain rock slopes which are susceptible to fail in the future. The proposed procedure and the derived critical thresholds present useful tools to assess the stability of degrading permafrost rock slopes potentially endangering human life and mountain infrastructure. The critical stability thresholds regarding the slope angle, fracture network orientation and bedrock temperature can be used to detect high mountain rock slopes which are susceptible to fail in the future. However, a prerequisite is to have data on the fracture network and the thermal field of the rock slope under investigation. Even more a detailed stability assessment requires a number of site specific input data, which is not realisable for a quick analysis of a current failure event. Since we are still at the beginning of developing numerical models for the mechanical response of a rock mass to warming/thawing, there is a huge potential for improvements. For instance, time dependent cycling is not yet implemented in most of the numerical models, neither it is in the presented models. Hence, they cannot be used to forecast a precise time of rock slope failure. The time of the final accelerated slope failure is coupled to the onset of thawing bedrock permafrost, which varies among field sites and has to be estimated by a separate thermal model.

200

205

210





Code/Data availability. All obtained data from the model, laboratory tests, geotechnical and geophysical surveys in the field as well as the numerical code will be freely accessible in the public data repository <https://zenodo.org/>. Data archiving is underway and will be finished within a short time. In the meantime, the data is available via the enclosed zipped folder enclosed in the supporting information.

Author contribution. Philipp Mamot (PM), Samuel Weber (SW) and Michael Krautblatter (MK) developed the general modelling approach. PM performed the geotechnical and geophysical surveys at the study site and analysed the related data. The setup and the procedure of the laboratory experiments was designed by PM and MK. The rock samples were prepared by Saskia Eppinger (SE) who also executed the laboratory tests and analysed the data, supported by PM. PM developed the numerical discontinuum code with UDEC and performed modelling. The modelling strategy was designed by PM, MK and SW. Analysis of the model results was done by PM and SW. The manuscript was prepared by PM, with a substantial contribution from SW and MK.

Competing interests. The authors declare that they have no conflict of interest.

Acknowledgements. The work for this article was funded by the Technical University of Munich. The authors thank the colleagues of the Chairs of Landslide Research and Engineering Geology of the Technical University of Munich as well as all motivated students who either supported the realisation of the laboratory campaigns or helped to perform the field surveys at the Zugspitze. However, the authors are particularly grateful for the valuable contribution of their colleagues Benjamin Jacobs, Andreas Dietrich, Riccardo Scandroglio, Bettina and Florian Menschik, who helped to collect and to analyse the data. Finally, a thanks goes to the Fritz and Lotte Schmidler Foundation for financing the TUFF fellowship that was held by Samuel Weber.

## References

- Arenson, L. U. and Springman, S. M.: Triaxial constant stress and constant strain rate tests on ice-rich permafrost samples, *Can. Geotech. J.*, 42, 412–430, <https://doi.org/10.1139/t04-111>, 2005.
- Aydin, A., and Basu, A.: The Schmidt hammer in rock material characterization, *Eng. Geol.*, 81, 1–14, 2005.
- ~~Baer, P., Huggel, C., McArdell, B. W. and Frank, F.: Changing debris flow activity after sudden sediment input: a case study from the Swiss Alps, *Geology Today*, 33, 216–223, <https://doi.org/10.1111/gto.12211>, 2017.~~
- Bandis, S. C., Lumsden, A. C. and Barton, N. R.: Fundamentals of rock joint deformation, *Int. J. Rock Mech. Min.*, 20, 249–268, 1983.
- Barnes, P., Tabor, D. and Walker, J. C. F.: The friction and creep of polycrystalline ice, *Proc. Roy. Soc. London. Series A*, 127–155, 1971.

- 1245 Barton, N. R.: A model study of rock-joint deformation, *Int. J. Rock Mech. Min.*, 9, 579–582, [https://doi.org/10.1016/0148-9062\(72\)90010-1](https://doi.org/10.1016/0148-9062(72)90010-1), 1972.
- Barton, N. R.: Shear strength criteria for rock, rock joints, rockfill and rock masses: Problems and some solutions, *J. Rock Mech. Geotech. Eng.*, 5, 249–261, <https://doi.org/10.1016/j.jrmge.2013.05.008>, 2013.
- Barton, N. R. and Choubey, V.: The shear strength of rock joints in theory and practice, *Rock Mech.*, 10, 1–54, 1977.
- 1250 Bhasin, R., and Kaynia, A. M.: Static and dynamic simulation of a 700-m high rock slope in western Norway. *Eng. Geol.*, 71(3), 213–226, [https://doi.org/10.1016/S0013-7952\(03\)00135-2](https://doi.org/10.1016/S0013-7952(03)00135-2), 2004.
- Biskaborn, B. K., Smith, S. L., Noetzli, J., Matthes, H., Vieira, G., Streletskiy, D. A., Schoeneich, P., Romanovsky, V. E., Lewkowicz, A. G., Abramov, A., Allard, M., Boike, J., Cable, W. L., Christiansen, H. H., Delaloye, R., Diekmann, B., Drozdov, D., Etzelmüller, B., Grosse, G., Guglielmin, M., Ingeman-Nielsen, T., Isaksen, K., Ishikawa, M., Johansson, M., Johannsson, H., Joo, A., Kaverin, D., Kholodov, A., Konstantinov, P., Kröger, T., Lambiel, C., Lanckman, J.-P., Luo, D., Malkova, G., Meiklejohn, I., Moskalenko, N., Oliva, M., Phillips, M., Ramos, M., Sannel, A. Britta K., Sergeev, D., Seybold, C., Skryabin, P., Vasiliev, A., Wu, Q., Yoshikawa, K., Zheleznyak, M. and Lantuit, H.: Permafrost is warming at a global scale, *Nat. Commun.*, 10, 264, <https://doi.org/10.1038/s41467-018-08240-4>, 2019.
- 1255 Böckli, L., Nötzli, J. and Gruber, S.: PermaNET-BY: Untersuchung des Permafrosts in den Bayerischen Alpen. Teilprojekt PermaNET (EU Alpine Space Interreg IVb), Zürich, 60 pp., 2011.
- Butkovitch, T. R.: The ultimate strength of ice, *US Snow, Ice and Permafrost Research Establishment Res. paper*, 15, 1954.
- Cai, M., Kaiser, P. K., Uno, H., Tasaka, Y. and Minami, M.: Estimation of rock mass deformation modulus and strength of jointed hard rock masses using the GSI system, *Int. J. Rock Mech. Min.*, 41, 3–19, [https://doi.org/10.1016/S1365-1609\(03\)00025-X](https://doi.org/10.1016/S1365-1609(03)00025-X), 2004.
- 1265 Chang, S.-H., Lee, C.-I. and Jeon, S.: Measurement of rock fracture toughness under modes I and II and mixed-mode conditions by using disc-type specimens, *Eng. Geol.*, 66, 79–97, [https://doi.org/10.1016/S0013-7952\(02\)00033-9](https://doi.org/10.1016/S0013-7952(02)00033-9), 2002.
- Cruden, D. M.: The shapes of cold, high mountains in sedimentary rocks, *Geomorphology*, 55, 249–261, [https://doi.org/10.1016/S0169-555X\(03\)00143-0](https://doi.org/10.1016/S0169-555X(03)00143-0), 2003.
- Davies, M. C.R., Hamza, O., Lumsden, B. W. and Harris, C.: Laboratory measurement of the shear strength of ice-filled rock joints, *Ann. Glaciol.*, 31, 463–467, <https://doi.org/10.3189/172756400781819897>, 2000.
- 1270 Davies, M. C.R., Hamza, O. and Harris, C.: The effect of rise in mean annual temperature on the stability of rock slopes containing ice-filled discontinuities, *Permafrost Periglac.*, 12, 137–144, <https://doi.org/10.1002/ppp378>, 2001.
- Deline, P., Gruber, S., Delaloye, R., Fischer, L., Geertsema, M., Giardino, M., Hasler, A., Kirkbride, M., Krautblatter, M., Magnin, F., McColl, S., Ravelin, L. and Schoeneich, P.: Ice Loss and Slope Stability in High-Mountain Regions, in: *Snow and Ice-Related Hazards, Risks and Disasters*, Academic Press, Boston, 521–561, 2015.

~~Deutscher Wetterdienst: Climate observations Germany. Climate Data Center.  
[https://opendata.dwd.de/climate\\_environment/CDC/](https://opendata.dwd.de/climate_environment/CDC/), last access: 27 November 2019 and 9 May 2020.~~

- Draebing, D. and Krautblatter, M.: P-wave velocity changes in freezing hard low-porosity rocks. A laboratory-based time-average model, *The Cryosphere*, 6, 1163–1174, <https://doi.org/10.5194/tc-6-1163-2012>, 2012.
- 1280 Dramis, F., Govi, M., Guglielmin, M. and Mortara, G.: Mountain permafrost and slope instability in the Italian Alps. The Val Pola Landslide, *Permafrost Periglac.*, 6, 73–81, <https://doi.org/10.1002/ppp.3430060108>, 1995.
- Dwivedi, R. D., Soni, A. K., Goel, R. K. and Dube, A. K.: Fracture toughness of rocks under sub-zero temperature conditions, *Int. J. Rock Mech. Min.*, 37, 1267–1275, 2000.
- Eberhardt, E., Stead, D. and Coggan, J. S.: Numerical analysis of initiation and progressive failure in natural rock slopes—the 1285 1991 Randa rockslide, *Int. J. Rock Mech. Min.*, 41, 69–87, [https://doi.org/10.1016/S1365-1609\(03\)00076-5](https://doi.org/10.1016/S1365-1609(03)00076-5), 2004.
- Etzelmüller, B.: Recent Advances in Mountain Permafrost Research, *Permafrost Periglac.*, 24, 99–107, <https://doi.org/10.1002/ppp.1772>, 2013.
- Fischer, L., Käab, A., Huggel, C. and Noetzi, J.: Geology, glacier retreat and permafrost degradation as controlling factors of slope instabilities in a high-mountain rock wall. The Monte Rosa east face, *Nat. Hazard. Earth Sys.*, 6, 761–772, 1290 <https://doi.org/10.5194/nhess-6-761-2006>, 2006.
- Fischer, L., Amann, F., Moore, J. R. and Huggel, C.: Assessment of periglacial slope stability for the 1988 Tschierwa rock avalanche (Piz Morteratsch, Switzerland), *Eng. Geol.*, 116, 32–43, <https://doi.org/10.1016/j.enggeo.2010.07.005>, 2010.
- Fischer, L., Purves, R. S., Huggel, C., Noetzi, J. and Haerberli, W.: On the influence of topographic, geological and cryospheric factors on rock avalanches and rockfalls in high-mountain areas, *Nat. Hazard. Earth Sys.*, 12, 241–254, 2012.
- 1295 Gallemann, T., Haas, U., Teipel, U., Poschinger, A. von, Wagner, B., Mahr, M. and Bäse, F.: Permafrost-Messstation am Zugspitzgipfel: Ergebnisse und Modellberechnungen, *Geologica Bavarica*, 115, 1–77, 2017.
- [Gambino, G. F. and Harrison, J. P.: Rock Engineering Design in Frozen and Thawing Rock. Current Approaches and Future Directions, \*Procedia Engineering\*, 191, 656–665, doi: 10.1016/j.proeng.2017.05.229, 2017.](#)
- Gischig, V., Amann, F., Moore, J. R., Loew, S., Eisenbeiss, H. and Stempfhuber, W.: Composite rock slope kinematics at the 1300 current Randa instability, Switzerland, based on remote sensing and numerical modeling, *Eng. Geol.*, 118, 37–53, <https://doi.org/10.1016/j.enggeo.2010.11.006>, 2011a.
- Gischig, V. S., Moore, J. R., Evans, K. F., Amann, F. and Loew, S.: Thermomechanical forcing of deep rock slope deformation. 1. Conceptual study of a simplified slope, *J. Geophys. Res.: Earth Surface*, 116, <https://doi.org/10.1029/2011JF002006>, 2011b.
- 1305 Gischig, V. S., Moore, J. R., Keith, F. E., Amann, F. and Loew, S.: Thermomechanical forcing of deep rock slope deformation: 2. The Randa rock slope instability, *J. Geophys. Res.*, 116, F04011, <https://doi.org/10.1029/2011JF002007>, 2011c.
- Glamheden, R.: Thermo-mechanical behaviour of refrigerated caverns in hard rock, Göteborg, 2001.
- Glamheden, R. and Lindblom, U.: Thermal and mechanical behaviour of refrigerated caverns in hard rock, *Tunn. Undergr. Sp. Tech.*, 17, 341–353, 2002.
- 1310 Gobiet, A., Kotlarski, S., Beniston, M., Heinrich, G., Rajczak, J. and Stoffel, M.: 21st century climate change in the European Alps-A review, *Sci. Total Environ.*, 493, 1138–1151, <https://doi.org/10.1016/j.scitotenv.2013.07.050>, 2014.

- Gruber, S. and Haeberli, W.: Permafrost in steep bedrock slopes and its temperature-related destabilization following climate change, *J. Geophys. Res.*, 112, 1–10, <https://doi.org/10.1029/2006JF000547>, 2007.
- 1315 Gruber, S., Hoelzle, M. and Haeberli, W.: Permafrost thaw and destabilization of Alpine rock walls in the hot summer of 2003, *Geophys. Res. Lett.*, 31, L13504, <https://doi.org/10.1029/2004GL020051>, 2004.
- Günzel, F. K.: Shear strength of ice-filled rock joints, 9th International Conference on Permafrost, Fairbanks, Alaska, 28 June – 3 July 2008, 2008.
- Haberkorn, A., Wever, N., Hoelzle, M., Phillips, M., Kenner, R., Bavay, M. and Lehning, M.: Distributed snow and rock temperature modelling in steep rock walls using Alpine3D, *The Cryosphere*, 11, 585–607, [https://doi.org/10.5194/tc-11-](https://doi.org/10.5194/tc-11-585-2017)  
1320 585-2017, 2017.
- Harris, C., Arenson, L. U., Christiansen, H. H., Etzelmüller, B., Frauenfelder, R., Gruber, S., Haeberli, W., Hauck, C., Hölzle, M., Humlum, O., Isaksen, K., Kääh, A., Kern-Lütschg, M. A., Lehning, M., Matsuoka, N., Murton, J. B., Nötzli, J., Phillips, M., Ross, N., Seppälä, M., Springman, S. M. and Mühl, D. Vonder: Permafrost and climate in Europe. Monitoring and modelling thermal, geomorphological and geotechnical responses, *Earth-Science Reviews*, 92, 117–171,  
1325 <https://doi.org/10.1016/j.earscirev.2008.12.002>, 2009.
- ~~Hauck, C.: New Concepts in Geophysical Surveying and Data Interpretation for Permafrost Terrain, *Permafrost Periglac.*, 24, 131–137, <https://doi.org/10.1002/ppp.1774>, 2013.~~
- Hauck, C. and Kneisel, C. (Eds.): *Applied Geophysics in Periglacial Environments*, Cambridge University Press, Cambridge, 2008.
- 1330 Hipp, T., Etzelmüller, B., Farbro, H., Schuler, T. V. and Westermann, S.: Modelling borehole temperatures in Southern Norway – insights into permafrost dynamics during the 20th and 21st century, *The Cryosphere*, 6, 553–571, <https://doi.org/10.5194/tc-6-553-2012>, 2012.
- Hoek, E. and Brown, E. T.: Practical estimates of rock mass strength, *Int. J. Rock Mech. Min.*, 34, 1165–1186, [https://doi.org/10.1016/S1365-1609\(97\)80069-X](https://doi.org/10.1016/S1365-1609(97)80069-X), 1997.
- 1335 Hoek, E., Carranza-Torres, C. and Corkum, B.: *Hoek-Brown failure criterion - 2002 Edition*, Toronto, Canada, 2002.
- Huang, D., Cen, D., Ma, G. and Huang, R.: Step-path failure of rock slopes with intermittent joints, *Landslides*, 12, 911–926, <https://doi.org/10.1007/s10346-014-0517-6>, 2015.
- Huggel, C., Zraggen-Oswald, S., Haeberli, W., Kääh, A. and Polkvoj, A.: The 2002 rock/ice avalanche at Kolka/Karmadon, Russian Caucasus: assessment of extraordinary avalanche formation and mobility, and application of QuickBird satellite  
1340 imagery, *Nat. Hazard. Earth Sys.*, 5, 173–187, 2005.
- Huggel, C., Salzmann, N., Allen, S., Caplan-Auerbach, J., Fischer, L., Haeberli, W., Larsen, C., Schneider, D. and Wessels, R.: Recent and future warm extreme events and high-mountain slope stability, *Philos. T. Roy. Soc. A*, 368, 2435–2459, <https://doi.org/10.1098/rsta.2010.0078>, 2010.
- Huggel, C., Allen, S., Deline, P., Fischer, L., Noetzli, J. and Ravanel, L.: Ice thawing, mountains falling - are alpine rock slope  
1345 failures increasing?, *Geology Today*, 28, 98–104, <https://doi.org/10.1111/j.1365-2451.2012.00836.x>, 2012.

- Inada, Y. and Yokota, K.: Some studies of low temperature rock strength, *Int. J. Rock Mech. Min.*, 21, 145–153, [https://doi.org/10.1016/0148-9062\(84\)91532-8](https://doi.org/10.1016/0148-9062(84)91532-8), 1984.
- Itasca Consulting Group, I.: UDEC - Universal Distinct Element Code. User's Manual, Minneapolis, 2019.
- Jaeger, J. C., Cook, N. G. and Zimmerman, R. W.: *Fundamentals of rock mechanics*, Blackwell Publishing Ltd, 2007.
- 1350 ~~Jarvis, A., Reuter, H. I., Nelson, A. and Guevara, E.: Hole filled seamless SRTM data V4: available from <http://srtm.esi.egi-ar.org>.~~
- Jellinek, H. H. G.: Adhesive properties of ice, *J. Coll. Sci.*, 14, 268–280, 1959.
- Jennings, J.: A mathematical theory for the calculation of the stability of open cast mines, Johannesburg, Republic of South Africa, 1970.
- 1355 Keuschnig, M., Krautblatter, M., Hartmeyer, I., Fuss, C. and Schrott, L.: Automated Electrical Resistivity Tomography Testing for Early Warning in Unstable Permafrost Rock Walls Around Alpine Infrastructure, *Permafrost Periglac.*, 28, 158–171, <https://doi.org/10.1002/ppp.1916>, 2017.
- Kodama, J., Goto, T., Fujii, Y. and Hagan P.: The effects of water content, temperature and loading rate on strength and failure process of frozen rocks, *Int. J. Rock Mech. Min.*, 62, 1–13, 2013.
- 1360 Körner, H. and Ulrich, R.: Geologische und felsmechanische Untersuchungen für die Gipfelstation der Seilbahn Eibsee-Zugspitze, *Geologica Bavarica*, 55, 404–421, 1965.
- Krautblatter, M., Verleysdonk, S., Flores-Orozco, A. and Kemna, A.: Temperature-calibrated imaging of seasonal changes in permafrost rock walls by quantitative electrical resistivity tomography (Zugspitze, German/Austrian Alps), *J. Geophys. Res. - Earth Surface*, 115, 1–15, 2010.
- 1365 Krautblatter, M., Huggel, C., Deline, P. and Hasler, A.: Research Perspectives on Unstable High-alpine Bedrock Permafrost. Measurement, Modelling and Process Understanding, *Permafrost Periglac.*, 23, 80–88, <https://doi.org/10.1002/ppp.740>, 2012.
- Krautblatter, M., Funk, D. and Günzel, F. K.: Why permafrost rocks become unstable: a rock-ice-mechanical model in time and space, *Earth Surf. Proc. Land.*, 38, 876–887, 2013.
- 1370 Kulatilake, P. H. S. W., Ucpirti, H., Wang, S., Radberg, G. and Stephansson, O.: Use of the distinct element method to perform stress analysis in rock with non-persistent joints and to study the effect of joint geometry parameters on the strength and deformability of rock masses, *Rock Mech. Rock Eng.*, 25, 253–274, <https://doi.org/10.1007/BF01041807>, 1992.
- Kveldsvik, V., Einstein, H. H., Nilsen, B. and Blikra, L. H.: Numerical Analysis of the 650,000 m<sup>2</sup> Åknes Rock Slope based on Measured Displacements and Geotechnical Data, *Rock Mech. Rock Eng.*, 42, 689, <https://doi.org/10.1007/s00603-008-0005-1>, 2008.
- 1375 Mamot, P., Weber, S., Schröder, T. and Krautblatter, M.: A temperature- and stress-controlled failure criterion for ice-filled permafrost rock joints, *The Cryosphere*, 12, 3333–3353, <https://doi.org/10.5194/tc-12-3333-2018>, 2018.
- Mamot, P., Weber, S., Lanz, M. and Krautblatter, M.: Brief communication: The influence of mica-rich rocks on the shear strength of ice-filled discontinuities, *The Cryosphere*, 14, 1849–1855, <https://doi.org/10.5194/tc-14-1849-2020>, 2020.

- 1380 Marinos, P. and Hoek, E.: Gsi: A Geologically Friendly Tool for Rock Mass Strength Estimation. ISRM International Symposium, Int. Soc. Rock Mech. Rock Eng., Melbourne, Australia, 2000.
- Marmy, A., Rajczak, J., Delaloye, R., Hilbich, C., Hoelzle, M., Kotlarski, S., Lambiel, C., Noetzi, J., Phillips, M., Salzmann, N., Staub, B. and Hauck, C.: Semi-automated calibration method for modelling of mountain permafrost evolution in Switzerland, *The Cryosphere*, 10, 2693–2719, <https://doi.org/10.5194/tc-10-2693-2016>, 2016.
- 1385 Mejía Camones, L. A., Vargas, E. d. A., Figueiredo, R. P. de and Velloso, R. Q.: Application of the discrete element method for modeling of rock crack propagation and coalescence in the step-path failure mechanism, *Eng. Geol.*, 153, 80–94, <https://doi.org/10.1016/j.enggeo.2012.11.013>, 2013.
- Mellor, M.: Mechanical properties of rocks at low temperatures, 2nd International Conference on Permafrost, Yakutsk, Siberia, 13-28 July 1973, 1973.
- 1390 Miller, H.: Der Bau des westlichen Wettersteingebirges, *Zeitschrift deutsche geologische Gesellschaft*, 113, 409–425, 1962.
- Moore, J. R., Gischig, V., Katterbach, M. and Loew, S.: Air circulation in deep fractures and the temperature field of an alpine rock slope, *Earth Surf. Proc. Land.*, 36, 1985–1996, <https://doi.org/10.1002/esp.2217>, 2011.
- Murton, J., Kuras, O., Krautblatter, M., Cane, T., Tschofen, D., Uhlemann, S., Schober, S. and Watson, P.: Monitoring rock freezing and thawing by novel geoelectrical and acoustic techniques, *J. Geophys. Res. - Earth Surface*, 121, 2309–2332, <https://doi.org/10.1002/2016JF003948>, 2016.
- 1395 Myhra, K. S., Westermann, S. and Etzelmüller, B.: Modelled Distribution and Temporal Evolution of Permafrost in Steep Rock Walls Along a Latitudinal Transect in Norway by CryoGrid 2D, *Permafrost Periglac.*, 28, 172–182, <https://doi.org/10.1002/ppp.1884>, 2017.
- Noetzi, J.: Modeling transient three-dimensional temperature fields in mountain permafrost, Dissertation, University of Zurich, Zurich, 2008.
- 1400 Noetzi, J. and Gruber, S.: Transient thermal effects in Alpine permafrost, *The Cryosphere*, 3, 85–99, <https://doi.org/10.5194/tc-3-85-2009>, 2009.
- Noetzi, J., Gruber, S., Kohl, T., Salzmann, N. and Haerberli, W.: Three-dimensional distribution and evolution of permafrost temperatures in idealized high-mountain topography, *J. Geophys. Res.: Earth Surface*, 112, <https://doi.org/10.1029/2006JF000545>, 2007.
- 1405 Noetzi, J., Gruber, S. and Poschinger, A. von: Modellierung und Messung von Permafrosttemperaturen im Gipfelgrat der Zugspitze, Deutschland, *Geographica Helvetica*, 65, 113–123, 2010.
- Noetzi, J., Pellet, C. and Staub, B.: PERMOS 2019. Permafrost in Switzerland 2014/2015 to 2017/2018. Glaciological Report (Permafrost) No. 16-19, 104 pp., 2019.
- 1410 Phillips, M., Wolter, A., Lüthi, R., Amann, F., Kenner, R. and Bühler, Y.: Rock slope failure in a recently deglaciated permafrost rock wall at Piz Kesch (Eastern Swiss Alps), February 2014, *Earth Surf. Proc. Land.*, 42, 426–438, <https://doi.org/10.1002/esp.3992>, 2017.

- 1415 ~~Pogliotti, P., Guglielmin, M., Cremonese, E., Di Morra Cella, U., Filippa, G., Pellet, C. and Hauck, C.: Warming permafrost and active layer variability at Cime Bianche, Western European Alps, *The Cryosphere*, 9, 647–661, <https://doi.org/10.5194/te-9-647-2015>, 2015.~~
- Poisel, R. and Preh, A.: Rock slope initial failure mechanisms and their mechanical models, *Felsbau*, 22, 40–45, 2004.
- Raveland, L. and Deline, P.: La face ouest des Drus (massif du Mont-Blanc): évolution de l'instabilité d'une paroi rocheuse dans la haute montagne alpine depuis la fin du petit âge glaciaire, *Géomorphologie*, 4, 261–272, 2008.
- 1420 Raveland, L. and Deline, P.: Climate influence on rockfalls in high-Alpine steep rockwalls. The north side of the Aiguilles de Chamonix (Mont Blanc massif) since the end of the 'Little Ice Age', *Holocene*, 21, 357–365, <https://doi.org/10.1177/0959683610374887>, 2011.
- Raveland, L. and Deline, P.: Rockfall Hazard in the Mont Blanc Massif Increased by the Current Atmospheric Warming, in: *Engineering Geology for Society and Territory - Volume 1: Climate Change and Engineering Geology*, Springer International Publishing, Cham, 425–428, 2015.
- 1425 Raveland, L., Allignol, F., Deline, P., Gruber, S. and Ravello, M.: Rock falls in the Mont Blanc Massif in 2007 and 2008, *Landslides*, 7, 493–501, 2010.
- Rentsch, W. and Krompholz, G.: Zur Bestimmung elastischer Konstanten durch Schallgeschwindigkeitsmessungen, *Bergakademie - Zeitschrift für Bergbau, Hüttenwesen und verwandte Wissenschaften*, 13, 492–504, 1961.
- Sanderson, T. J. O.: *Ice Mechanics. Risks to offshore structures*, Graham & Trotman, 1988.
- 1430 ~~Sass, O.: *Rock moisture measurements. Techniques, results, and implications for weathering*, *Earth Surf. Proc. Land.*, 30, 3, 359–374, <https://doi.org/10.1002/esp.1214>, 2005.~~
- Schulson, E. M. and Duval, P.: *Creep and Fracture of Ice*, Cambridge University Press, 2009.
- Stead, D., Eberhardt, E. and Coggan, J. S.: Developments in the characterization of complex rock slope deformation and failure using numerical modelling techniques, *Eng. Geol.*, 83, 217–235, <https://doi.org/10.1016/j.enggeo.2005.06.033>, 2006.
- 1435 Supper, R., Ottowitz, D., Jochum, B., Römer, A., Pfeiler, S., Kauer, S., Keuschnig, M. and Ita, A.: Geoelectrical monitoring of frozen ground and permafrost in alpine areas. Field studies and considerations towards an improved measuring technology, *Near Surface Geophysics*, 12, 93–115, <https://doi.org/10.3997/1873-0604.2013057>, 2014.
- ~~SRTM DEM Digital Elevation Database: <http://srtm.csi.cgiar.org/>, last access: 14 February 2020.~~
- Tipler, P. A. and Mosca, G.: *Physics for Scientists and Engineers*, W. H. Freeman and Company, New York, 2004.
- 1440 Ulrich, R. and King, L.: Influence of mountain permafrost on construction in the Zugspitze mountains, Bavarian Alps, Germany, Beijing, China, July 5-9, 1993.
- Ulusay, R.: *The ISRM Suggested Methods for Rock Characterization, Testing and Monitoring: 2007-2014*, Springer International Publishing, 2015.
- 1445 Walter, F., Amann, F., Kos, A., Kenner, R., Phillips, M., Preux, A. de, Huss, M., Tognacca, C., Clinton, J., Diehl, T. and Bonanomi, Y.: Direct observations of a three million cubic meter rock-slope collapse with almost immediate initiation of ensuing debris flows, *Geomorphology*, 351, 106933, <https://doi.org/10.1016/j.geomorph.2019.106933>, 2020.



- Weber, S., Beutel, J., Faillettaz, J., Hasler, A., Krautblatter, M. and Vieli, A.: Quantifying irreversible movement in steep, fractured bedrock permafrost on Matterhorn (CH), *The Cryosphere*, 11, 567–583, <https://doi.org/10.5194/tc-11-567-2017>, 2017.
- 1450 Welkner, D., Eberhardt, E. and Hermanns, R. L.: Hazard investigation of the Portillo Rock Avalanche site, central Andes, Chile, using an integrated field mapping and numerical modelling approach, *Eng. Geol.*, 114, 278–297, <https://doi.org/10.1016/j.enggeo.2010.05.007>, 2010.
- Wyllie, D. C.: *Rock slope engineering. Civil applications*, Taylor & Francis Group, Boca Raton, 2018.
- ~~Zhang, X. P. and Wong, L. Ngai Yuen: Crack Initiation, Propagation and Coalescence in Rock-Like Material Containing Two~~
- 1455 ~~Flaws. A Numerical Study Based on Bonded Particle Model Approach, *Rock Mech. Rock Eng.*, 46, 1001–1021, <https://doi.org/10.1007/s00603-012-0323-1>, 2013.~~
- ~~Zhang, K., Cao, P., Meng, J., Li, K. and Fan, W.: Modeling the Progressive Failure of Jointed Rock Slope Using Fracture Mechanics and the Strength Reduction Method, *Rock Mech. Rock Eng.*, 48, 771–785, <https://doi.org/10.1007/s00603-014-0605-x>, 2015.~~



## Supplement of

# Stability assessment of degrading permafrost rock slopes based on a coupled thermo-mechanical model

Philipp Mamot, Samuel Weber, Saskia Eppinger, and Michael Krautblatter

5 Chair of Landslide Research, Technical University of Munich, 80333, Germany

Correspondence to: Philipp Mamot (Philipp.mamot@tum.de)

The supplementary material gives additional information to:

- 10 1. Kinematic analysis and estimation of the potential failure volume  
~~+2.~~ Characterisation of the fracture network  
~~2.1. Kinematic analysis and estimation of the potential failure volume~~
- 15 3. Fracture displacements ~~at the study site~~  
4. Measuring setup and data acquisition of electrical resistivities ~~in the laboratory and~~ at the study site  
5. Near-surface rock temperature measurements ~~at the study site~~  
6. Rock-mechanical laboratory tests  
6.1 Intact rock  
6.2 Rock joints
- 20 7. Numerical stability analysis  
7.1 Further assumptions for the procedure of the numerical analysis  
~~7.2 Additional sensitivity analyses of the numerical models for a simplified permafrost rock slope with rising temperature~~

25 The following figures and tables are included in the text:

- Figure S1. Kinematic analysis of the unstable south-face of the Zugspitze summit crest for a potential plane or wedge failure. ~~Major structural features at the study site.~~
- Figure S2. Intersecting main shear zones delineating the unstable rock mass with and without the potential failure volume. ~~structural features at the study site.~~

- 30 • ~~Figure S3. Kinematic analysis of the unstable south face of the Zugspitze summit crest for a potential plane or wedge failure.~~
- ~~Figure S4. Network of thermal and mechanical measurements at the study site with reference to geomorphic and anthropogenic features.~~
- Figure S35. Near-surface fracture displacements at the study site between 09/2013 and 07/2019.
- 35 • ~~Figure S6. Laboratory tested electrical resistivity of frozen and unfrozen Wetterstein limestone~~
- Table S1. Metadata on the instrumented temperature sensors at the Zugspitze summit ridge.
- Figure S47. Near-surface rock temperatures at the Zugspitze summit crest between 08/2015 and 08/2019.
- Figure S58. Warming behaviour of frozen dummy rock samples during simulated uniaxial compression, Brazil and ultrasonic tests.
- 40 • Figure S6: Influence of a bigger model domain and a higher disturbance factor D on the slope stability.
- Figure S79. Maximum model displacements versus slope angle for a warming rock slope above -2 °C.
- Figure S840. Maximum model displacements versus slope angle for a warming permafrost rock slope and the twofold amount of numerical cycles for each warming step.
- Figure S944. Maximum model displacements against slope angle for a warming permafrost rock slope with different
- 45 levels of rock mass strength and deformability.

The following data sets are provided (as \*.xlsx or \*.txt files) in the zipped folder “Suppl. Material”:

- Dataset S1. Geometrical joint properties
- 50 • Dataset S2. Crack displacements at the field site
- Dataset S3. Raw data of the electrical resistivity tomography in the field
- Dataset S4: Laboratory electrical resistivity
- Dataset S5. Topography of the Zugspitze summit crest (for the ERT)
- Dataset S6. Near-surface rock temperature at the north-face and the south-face of the Zugspitze summit ridge
- 55 • Dataset S7. Laboratory dilatational wave and Poisson’s ratio
- Dataset S8. Laboratory uniaxial compressive strength
- Dataset S9. Laboratory uniaxial tensile strength
- Dataset S10. Laboratory joint wall compressive strength and joint basic friction angle
- Dataset S11. Roughness coefficient of joints at the field site
- 60 • Dataset S12. Size of samples for testing of intact rock properties
- Dataset S13. Warming pattern of frozen dummy rock cylinders / discs during simulated uniaxial compression testing / Brazil tests.

- Dataset S14. Results of the numerical model: Maximum displacements and factors of safety
- Dataset S15. Numerical codes for UDEC
- Dataset S16. Material parameters for different disturbance factors D

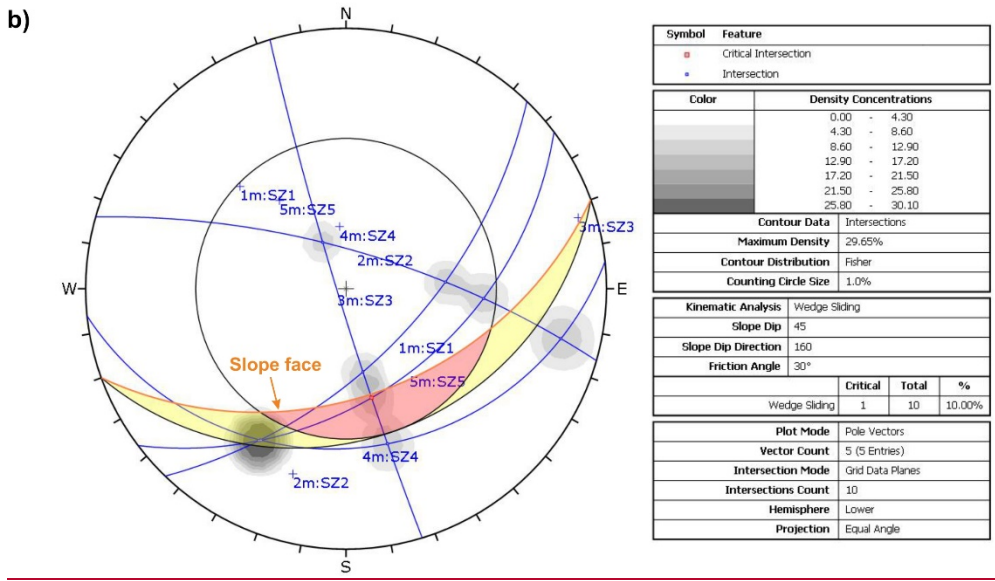
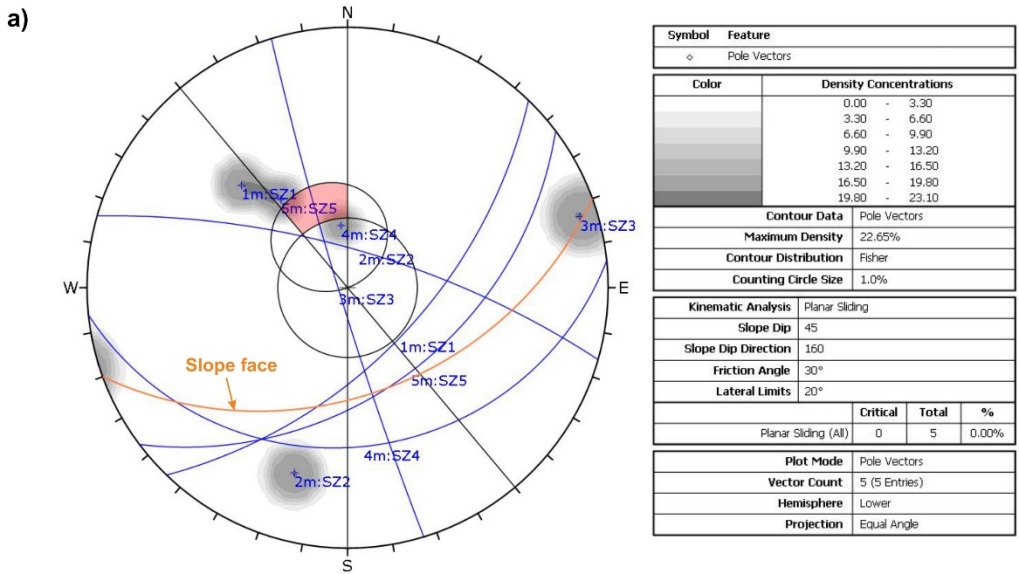
## 1 Kinematic analysis and estimation of the potential failure volume

70 UAV-based photogrammetry was performed at the Zugspitze summit crest to compute a 3D point cloud providing information on the possible (i) shear zones delimiting the unstable rock mass, (ii) type of failure and (iii) failure volume. Data were acquired with the drone Phantom 4 Pro (DJI). Red, green and blue images are captured simultaneously and with different viewing angles. The included camera is equipped with a 1"CMOS sensor with 20 MP. The 3D point cloud was generated with Agisoft Photoscan v.1.4.5 and analysed with RISCAN PRO 2.7.1 64 bit. It has a total number of 21 Mio points with a resolution of ca. 5 cm, and rgb information for identifying geological features.

75 Shear zones SZ1, SZ2 and SZ3, which were identified as potential failure planes in the field (Fig. 1e), were recognised in the 3D point cloud by manually defining sections of points which lie on a common plane. These sections were extrapolated to mean failure planes and intersect with each other and the slope face. A fourth and fifth shear zone (SZ4 and SZ5) were determined to form the possible downslope boundary of the unstable rock mass (Fig. 1e). The approximate total volume of the potentially failing rock mass was estimated to be  $2.9 * 10^4$  m<sup>3</sup>. This was done by calculating the difference between the intersected failure planes and the terrain surface, both related to a lower reference plane.

80 A kinematic analysis of a potential plane and wedge failure was conducted with DIPS 7.0 including the southern slope-face (45/160) and the main shear zones, which were identified due to field mapping and the preceding analysis of the point cloud. The lateral limit for critical dip directions of the failure plane was set to the default of 20°. The friction angle was set to 30°, based on direct shear tests of frozen and unfrozen Wetterstein limestone by Krautblatter et al. (2013).

85 The results showed that pure plane failure can occur for those sections of SZ1, SZ4 or SZ5 for which the dip is lower than the inclination of the slope-face (45°) and higher than the friction angle of the rock joints (30°) (Fig. S1a). Pure wedge failure is possible for intersections of SZ3/SZ5, and marginally for SZ3/SZ4 or SZ3/SZ1 (Fig. S1b). Though planar sliding is the dominant kinematic failure mode which affects the major left part of the unstable rock mass, we assume that the instability is driven by a complex combination of both a plane and a wedge failure (Fig. 1e, Fig. S1). Neither pure planar sliding nor pure wedge sliding are likely to be the controlling failure mechanism. In the upper part of the rock slope, planar sliding may occur  
90 along SZ1, while wedge failure supports the displacement along SZ1/SZ3 including a tension crack SZ2. At lower slope sections, planar sliding can occur along SZ4 and SZ5, while wedge failure potentially enhances the failure process along SZ3 and a stepped plane constituted of SZ4 and SZ5.



95 **Figure S1: Kinematic analysis of the unstable south-face of the Zugspitze summit crest for a potential plane or wedge failure. (a) Plane failure can occur for those shear zones whose poles lie within the critical red window. This is valid for SZ4 and SZ5, and marginally for SZ1. The friction cone in the centre has an angle of 30°. The lateral limit of the critical window is set to 20°. (b) Wedge failure is possible for intersections of planes which lie within the critical red window. This is the case for intersections of SZ3/SZ5, and marginally for SZ3/SZ4 or SZ3/SZ1. Sliding along SZ4 can occur for wedges constituted of SZ1/SZ4 or SZ5/SZ4 (yellow area). The friction cone at the margin has an angle of 30°.**

100



## 2.1 Characterisation of the fracture network

The fracture network was mapped systematically along five distinct scanlines distributed over the south-slope and at the top of the summit crest (Fig. 1b) as working at the north-face requires rope safeguarding (Fig. S4). The studied joint characteristics involved dip and dip direction, spacing, aperture, joint frequency and joint roughness (Table 2). The entire data set contains 129 discontinuities.

The mean dip and dip direction of the joint sets were calculated with DIPS 7.0 (RocScience) defining main joint sets in pole density plots. Geometrical Terzaghi weighting was applied to correct potential bias which is introduced in favour of discontinuities perpendicular to the direction of the scanline.

The joint roughness was recorded with a Barton comb / profilometer along 14 profiles not included in the five scanlines. Each profile consisted of between three and seven subsections of 26 cm. Data acquisition and analysis were performed according to Tse and Cruden (1979). The coefficient  $Z_2$  was determined by

$$Z_2 = \left[ \frac{1}{M(\Delta x)^2} \sum_{i=1}^M (y_i + 1 - y_i)^2 \right]^{1/2} \quad (\text{S1})$$

where  $y_i$  is the distance between the rock surface and a fixed reference line,  $x$  is a specified equal record interval and  $M$  is the number of measured intervals along the profile. The applied sampling interval  $x$  at the field site was 5 mm. To calculate the JRC, the following formula proposed by Yang et al. (2001) was used:

$$JRC = 32.69 + 32.98 \log_{10} Z_2 \quad (\text{S2})$$

As  $Z_2$  is only valid for the range of 0.1 to 0.42, values  $< 0.1$  were assigned a zero JRC.

A very prominent and persistent shear zone was detected at the south-slope (SZ1 in Fig. 1). According to geotechnical field mapping, SZ1 has a trace length of approximately 70 m and runs in a maximum depth of 10–15 m. At some places it opens to a decimetre wide, highly fractured zone filled with fine material ranging from clay-size to gravel-size. This type of infilling is observed in most of the bigger shear zones at the summit region (Fig. S2c). Four dolines develop along the major shear zones SZ1 and SZ2 (Fig. 1a): Two of them form along SZ1, while the third one develops along SZ2. The fourth doline is located at the point of intersection between SZ1 and SZ2 (Fig. S2a and Fig. S2b).

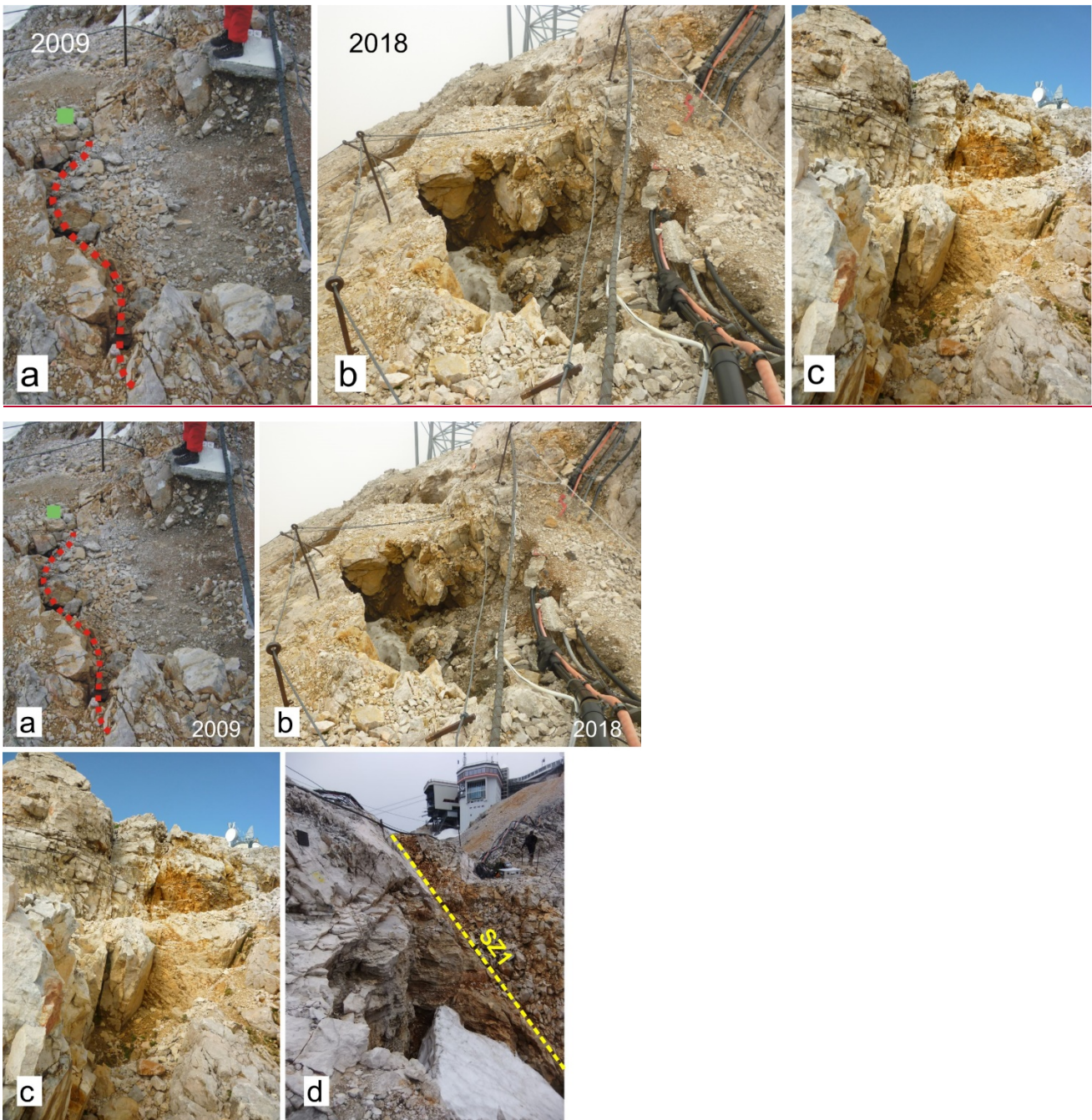


**Figure S21: Growing doline and prominent shear zones (SZ) filled with fine material at the crestline of the Zugspitze summit area. (a) and (b) Doline at the intersection of SZ1 and SZ2 (Fig. 2b) (a) in 2009 and (b) in 2018. (c) Shear zone filled with fine material. (d) Shear zone SZ1, visible at the inner wall of a doline.**



135

A very prominent and persistent shear zone was detected at the south-slope (SZ1 in Fig. 2b and Fig. S1d). According to geotechnical field mapping, SZ1 has a trace length of approximately 70 m and runs in a maximum depth of 10–15 m. At some places it opens to a decimetre wide, highly fractured zone filled with fine material ranging from clay size to gravel size. This type of infilling is observed in most of the bigger shear zones at the summit region (Fig. S1e). Four dolines develop along the major shear zones SZ1 and SZ2 (Fig. S4): Two of them form along SZ1, while the third one develops along SZ2. The fourth doline is located at the point of intersection between SZ1 and SZ2 (Fig. S1a and Fig. S1b).

## 2 Kinematic analysis and estimation of the potential failure volume

140

UAV-based photogrammetry was performed at the Zugspitze summit crest to compute a 3D point cloud providing information on the possible (i) shear zones delimiting the unstable rock mass, (ii) type of failure and (iii) failure volume. Data were acquired with the drone Phantom 4 Pro (DJI). Red, green and blue images are captured simultaneously and with different viewing angles. The included camera is equipped with a 1" CMOS sensor with 20 MP. The 3D point cloud was generated with Agisoft Photoscan v.1.4.5 and analysed with RISCAN PRO 2.7.1 64 bit. It has a total number of 21 Mio points with a resolution of ca. 5 cm, and rgb information for identifying geological features.

145

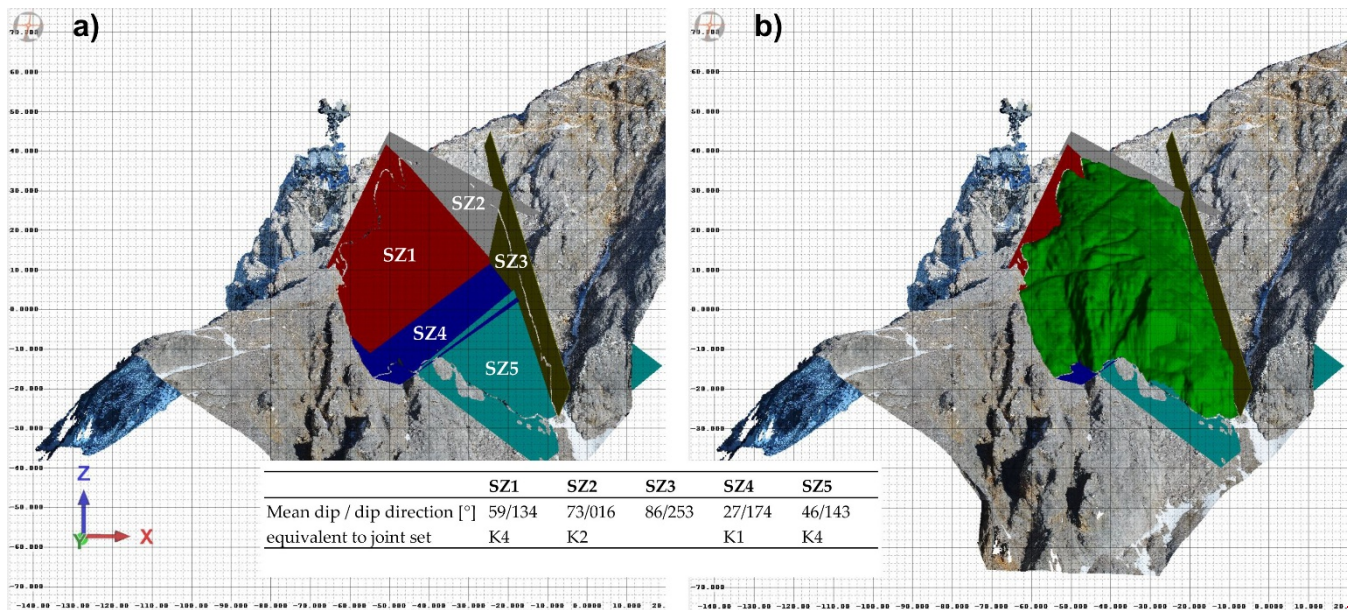


**Figure S2: Intersecting main shear zones (SZ) which delineate the unstable rock mass at the south face of the Zugspitze summit crest: (a) without and (b) with the potential failure volume.**

150

Shear zones SZ1, SZ2 and SZ3, which were identified as potential failure planes in the field (Fig. S2), were recognised in the 3D point cloud by manually defining sections of points which lie on a common plane. These sections were extrapolated to

mean failure planes and intersect with each other and the slope face. A fourth and fifth shear zone (SZ4 and SZ5) were determined to form the possible downslope boundary of the unstable rock mass (Fig. S2). The approximate total volume of the potentially failing rock mass was estimated to be  $2.9 \times 10^4 \text{ m}^3$ . This was done by calculating the difference between the intersected failure planes and the terrain surface, both related to a lower reference plane.

A simple kinematic analysis of a potential plane and wedge failure was conducted with DIPS 7.0 including the southern slope face (45/160) and the main shear zones, which were identified due to field mapping and the preceding analysis of the point cloud. The lateral limit for critical dip directions of the failure plane was set to the default of  $20^\circ$ . The friction angle was set to  $30^\circ$ , based on direct shear tests of frozen and unfrozen Wetterstein limestone by Krautblatter et al. (2013).

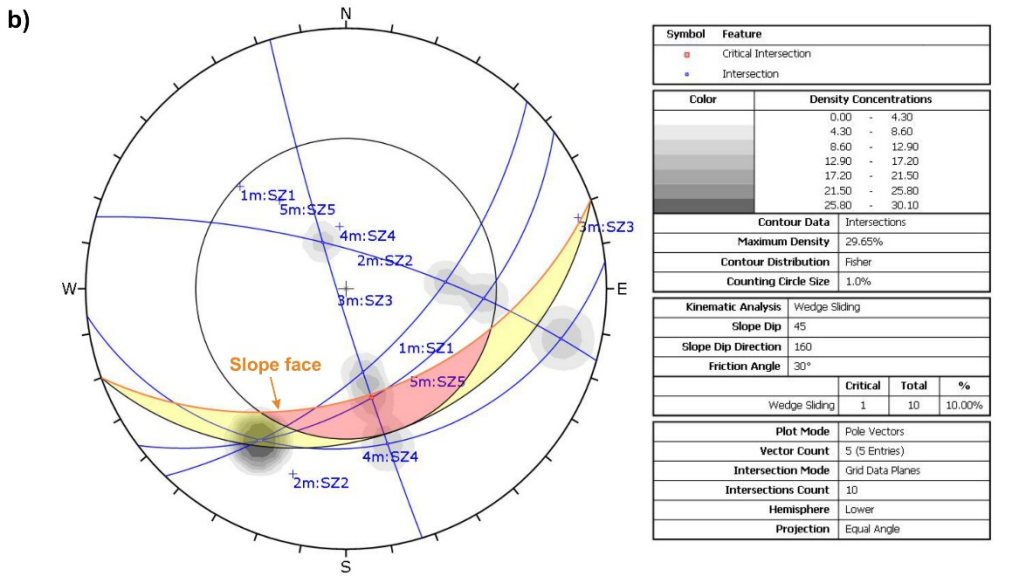
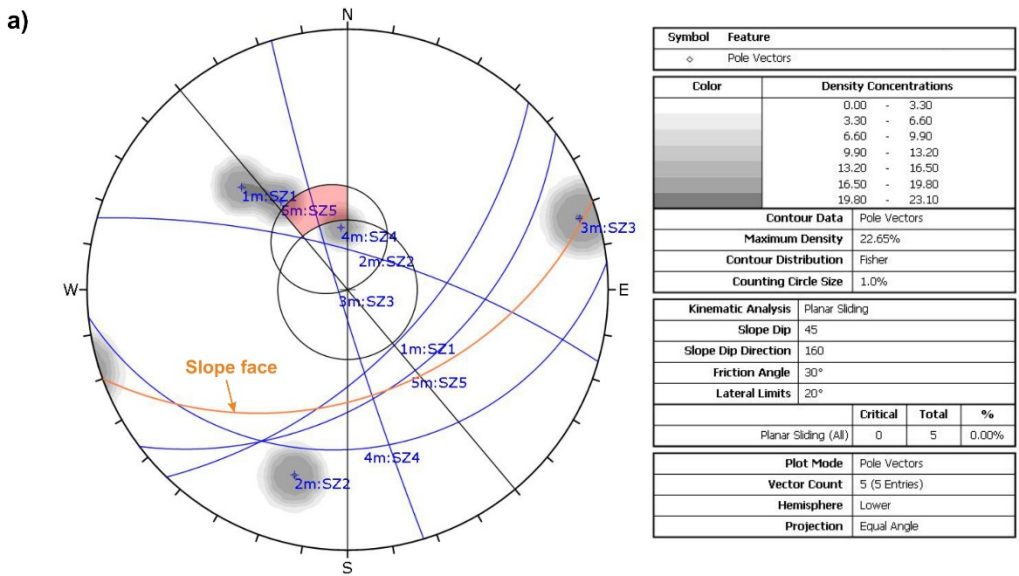


**Figure S3: Kinematic analysis of the unstable south face of the Zugspitze summit crest for a potential plane or wedge failure. (a) Plane failure can occur for those shear zones whose poles lie within the critical red window. This is valid for SZ4 and SZ5, and marginally for SZ1. The friction cone in the centre has an angle of 30°. The lateral limit of the critical window is set to 20°. (b) Wedge failure is possible for intersections of planes which lie within the critical red window. This is the case for intersections of SZ3/SZ5, and marginally for SZ3/SZ4 or SZ3/SZ1. Sliding along SZ4 can occur for wedges constituted of SZ1/SZ4 or SZ5/SZ4 (yellow area). The friction cone at the margin has an angle of 30°.**

165

170

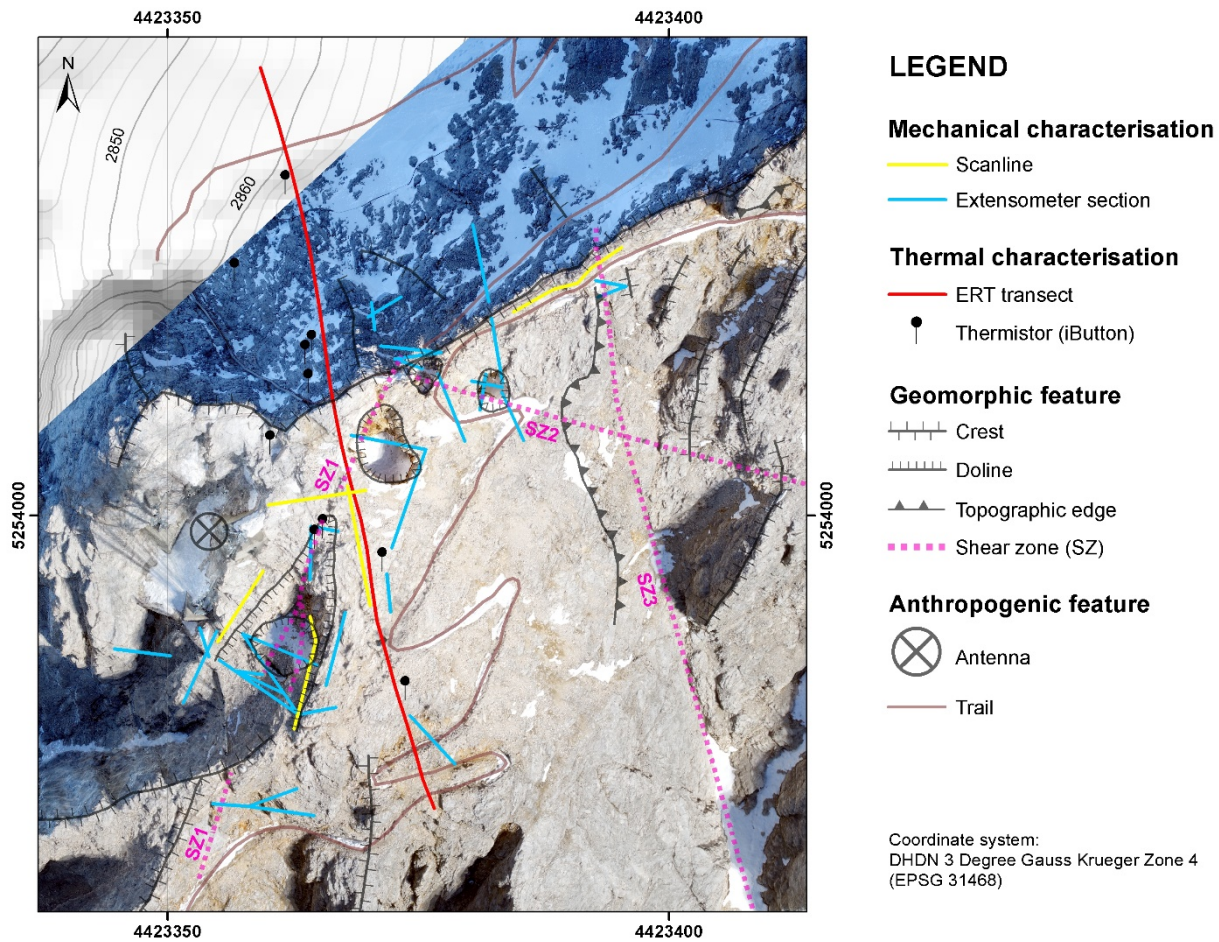
The results showed that pure plane failure can occur for those sections of SZ1, SZ4 or SZ5 for which the dip is lower than the inclination of the slope face (45°) and higher than the friction angle of the rock joints (30°) (Fig. S3a). Pure wedge failure is possible for intersections of SZ3/SZ5, and marginally for SZ3/SZ4 or SZ3/SZ1 (Fig. S3b).

175 Since pure plane or wedge failure are unlikely to be the controlling failure mechanism, we assume that the instability at the south face is related to a complex combination of both a plane and a wedge failure (Fig. S2, Fig. S3). In the upper part of the unstable rock mass, wedge failure may occur along SZ1/SZ3 including a tension crack SZ2, while local planar sliding along SZ1 supports the displacement. At lower slope sections, wedge failure may occur along SZ3 and a stepped plane constituted of SZ4 and SZ5, while planar sliding along SZ4 or SZ5 potentially enhances the failure process.

### 3 Fracture displacements ~~at the study site~~

180 We performed repeated recordings of crack displacements distributed over the most active parts of the rockslide at the Zugspitze summit crest to quantify mean displacement rates and assess seasonal patterns of movement. The upper part of the south-face was equipped with 32 sections for displacement measurements. Each section is delimited by two plugs fixed in the rock crossing one or more important joints or shear zones. Values were collected with a digital tape extensometer (Soil Instruments Ltd.) at the beginning (June/July) and at the end (September/October) of the accessible, snow-free summer season between 09/2013 and 07/2019. The tape extensometer measures with a maximum resolution of 0.01 mm. The locations of the  
185 sections are displayed in Fig. [1bS4](#).



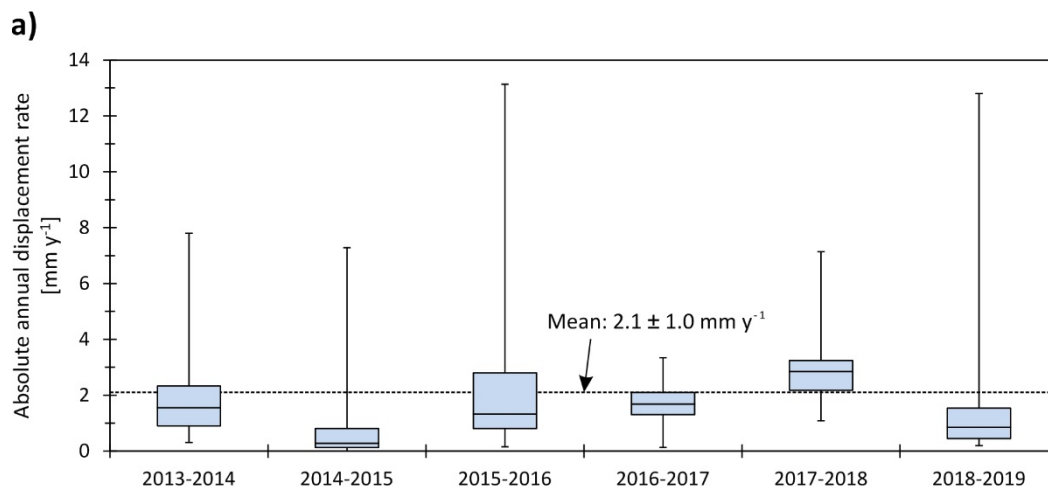


190 **Figure S4: Network of geophysical and geotechnical measurements at the Zugspitze summit ridge including reference to geomorphologic and anthropogenic features. The digital elevation model was obtained from the Bavarian Agency for Digitisation, High-Speed Internet and Surveying. The orthofoto was computed with Agisoft Photoscan v 1.4.5. derived by UAV-based photogrammetry.**

195 The annual mean absolute displacement for the period 09/2013–07/2019 measures  $2.1 \text{ mm y}^{-1}$  (Fig. S35a). To study the evolution of displacements over time, absolute annual fracture displacement rates were calculated from early summer to early summer of the subsequent year. Here, the medians of annual displacements range between  $0.3$  and  $4.8 \text{ mm y}^{-1}$  and do not point to either an acceleration or a deceleration between 2013 and 2019. Recording crack displacements twice a year, at the beginning and at the end of the summer season, allowed us to compare summer displacement rates with those of the remaining year (Fig. S35b): The monthly mean displacement rate reduces by a factor of 6.4 when changing from summer to the remaining seasons (summer:  $0.63 \text{ mm mo}^{-1}$ ; remaining year:  $0.10 \text{ mm mo}^{-1}$ ). This corresponds to a decrease by 84.4 %.

200





b)

	Fracture displacement in summer [mm mo <sup>-1</sup> ]				
	2015	2016	2017	2018	Total
Mean	1,22	0,21	0,85	0,25	0,63
Standard deviation	1,45	0,15	0,39	0,50	
Number of measured sections	30	30	31	30	

	in the remaining year [mm mo <sup>-1</sup> ]				Total
	2015/16	2016/17	2017/18	2018/19	
Mean	0,05	0,13	0,04	0,09	0,10
Standard deviation	0,04	0,07	0,04	0,15	
Number of measured sections	31	31	30	31	

Figure S35: Near-surface fracture displacements at the south-face of the Zugspitze summit crest between 09/2013 and 07/2019. (a) Boxplot of annual absolute displacement rates for the time period 2013-2019. (b) Monthly rates for summer (June to September) and the remaining year (October to May) since 2015.

205

#### 4 Measuring setup and data acquisition of electrical resistivities ~~in the laboratory and~~ at the study site

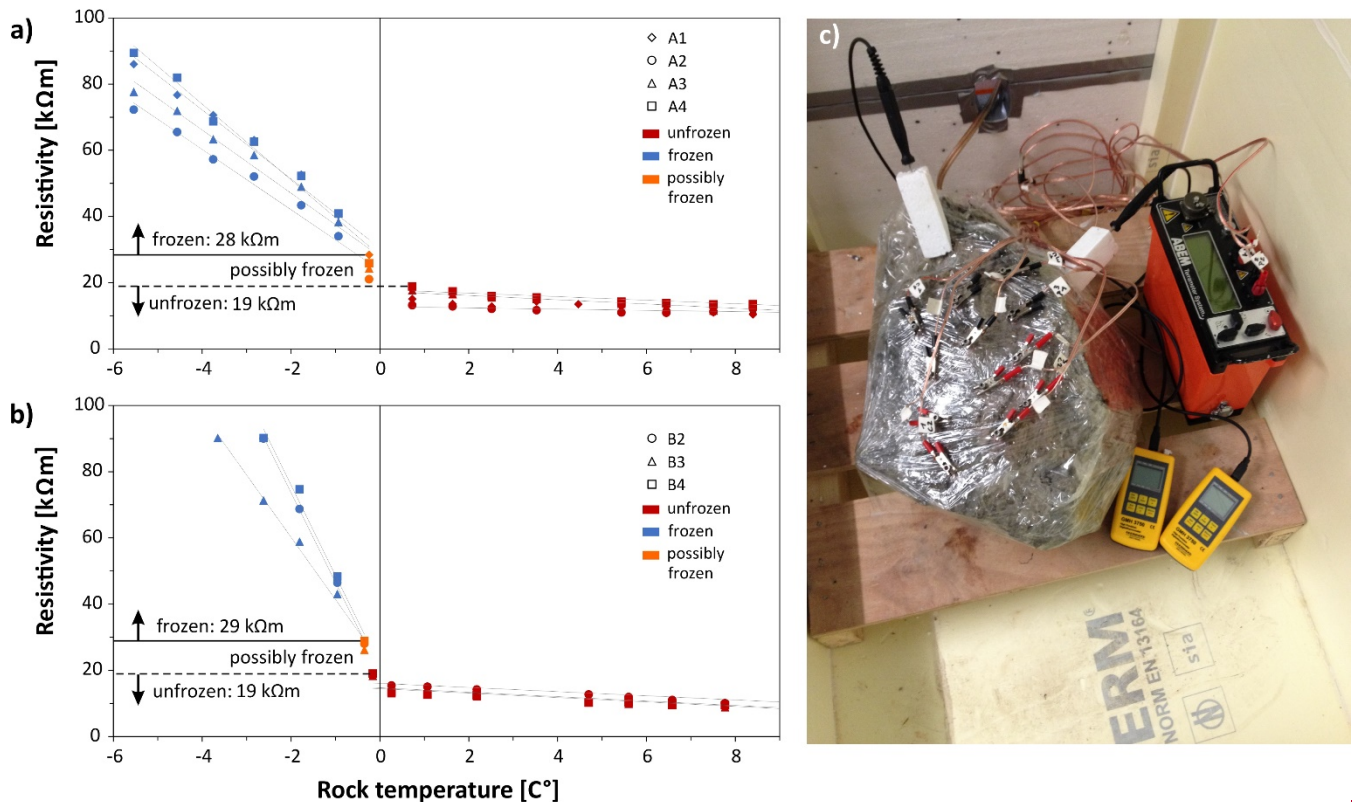
ERT was applied along a transect of approximately 100 m, crossing the ridge and covering its north- and south-face (Fig. 1aS4, Fig. 1b2b). In this way, we could assess more properly the effect of thermal differences induced by various exposures at the crest-topography. The transect for ERT consists of 41 electrodes (stainless steel nails) which were installed once and used for both surveys. The electrodes were separated from each other by a mean spacing of 2.5 m. To enhance electrode coupling, the steel nails were greased with an electrically conductive fluid and water was added to the contact between nails and ground just before the survey. Acquisition of geoelectrical data was performed with two distinct devices: an ABEM

210

215 Terrameter SAS 1000 and a Terrameter LS with maximum input/output voltages of  $\pm 400$  and  $\pm 600$  V, respectively, and corresponding injected currents of 1 and 0.1 mA, respectively. The applied input/output voltage and the current were standardised for all surveys and were 500 V and 1 mA, respectively. The applied electrode configurations for the ER surveys were Wenner (in 2014) and Wenner-Schlumberger (in 2015). ~~2D~~Two-dimensional data processing and inversions were performed with the commercial software package Res2Dinv. Data inversions were performed using robust inversion and model refinement with half the unit electrode spacing (Loke, 2019).

220 ~~The laboratory ER by Krautblatter et al. (2010) was supplemented by a further laboratory study with two samples of Zugspitze limestone collected at the study site. For this purpose, we followed the test procedure by Krautblatter et al. (2010). The rock samples (both with a size of 0.02 m<sup>3</sup>) were kept in a self-built, temperature-controlled cooling box for the duration of the tests. They were exposed to a single cooling and subsequent freezing trajectory from 10 down to -6 °C. Rock temperature was measured simultaneous to resistivity with two Pt100 sensors (Greisinger GMH3750, with a 0.03 °C precision) inserted in the rock samples (Fig. S6). Measurements were performed along 3-4 different Wenner arrays installed parallel to each other.~~

225



230 **Figure S6: Laboratory-tested electrical resistivity of frozen and unfrozen Wetterstein limestone collected at the study site. (a)-(b) Definition of frozen (blue symbols), unfrozen (red symbols) and possibly frozen (orange symbols) electrical resistivity based on the freezing trajectories of two rock samples. Measurements were performed along 3 or 4 different Wenner arrays (i.e., A1-A4 or B2-B4) installed parallel to each other. (c) Test setup in the laboratory cooling box.**

## 5 Near-surface rock temperature ~~at the study site~~

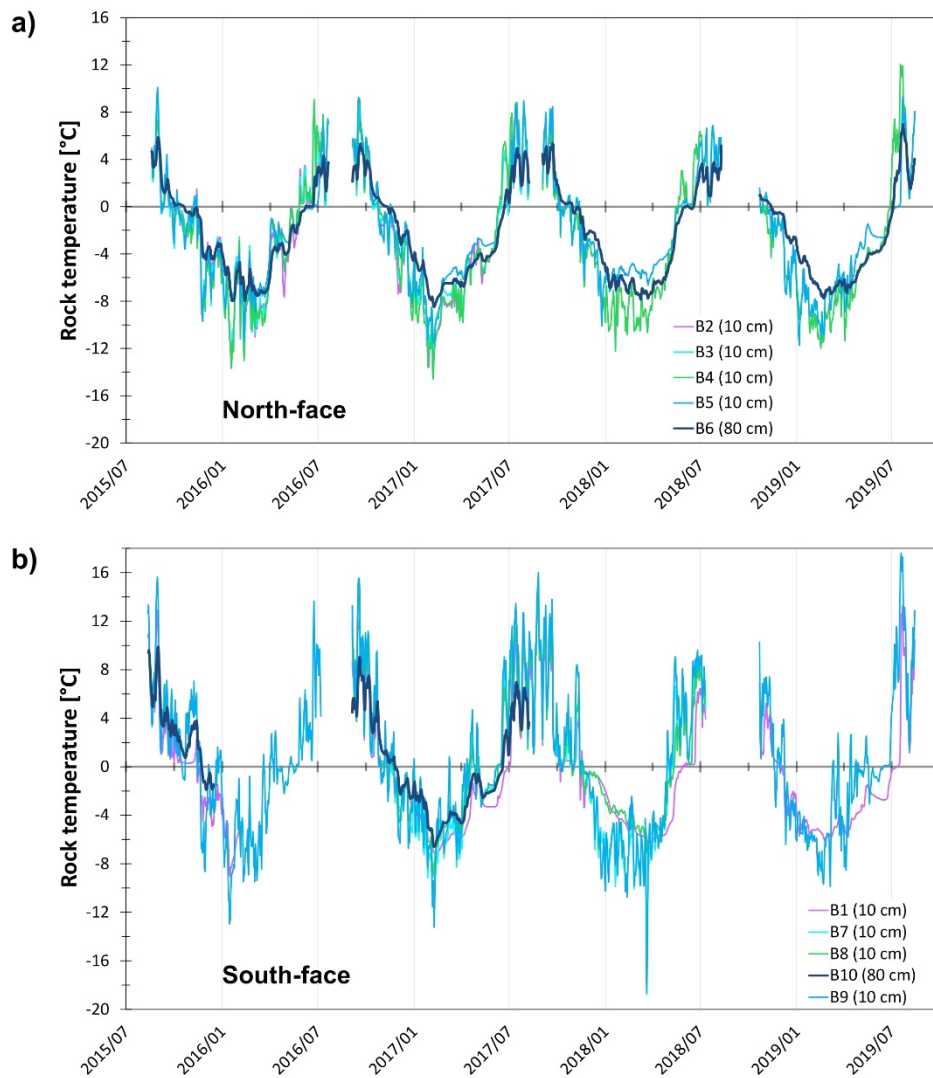
Rock temperature sensors (Maxim Integrated, iButton model DS1922L-F5) were instrumented in the direct surroundings of the geophysical survey lines in depths of 10 and 80 cm (locations are displayed in Fig. [S41b](#)). So far, iButtons have been applied successfully to measure ground surface or bedrock temperatures in alpine terrain (Gubler et al., 2011; Keuschnig, 2016). The preparation of the sensors and the installation technique in solid rock were taken from Keuschnig (2016). The sensors measured the rock temperature every two hours between August of 2015 to August of 2019 with an accuracy of  $\pm 0.5$  °C. Five iButtons were installed at the north-face and five iButtons at the south-face, whilst two of them were located within the shear zone SZ1 (Table S1).

~~The recordings of the thermistors demonstrate that the surficial rock layer (< 1 m) thaws during the summer months. This is valid for both slope-faces of the summit ridge (Fig. S4).~~

**Table S1: Metadata on the instrumented temperature sensors at the Zugspitze summit ridge. Locations are given in Fig. [S41b](#).**

iButton	Aspect [°]	Slope [°]	Depth [cm]	Characteristics
1	210 (S)	24	10	often snow, intense solar radiation
2	320 (N)	70	10	thin snow cover, shaded
3	320 (N)	70	10	thin snow cover, shaded
4	320 (N)	60	10	thin snow cover, shaded
5	320 (N)	52	10	thin snow cover, shaded
6	320 (N)	70	80	thin snow cover, shaded
7	160 (S)	32	10	often snow, intense solar radiation
8	140 (S)	55	10	at SZ1, often snow, intense solar radiation
9	160 (S)	58	10	often snow, intense solar radiation
10	140 (S)	55	75	at SZ1, often snow, intense solar radiation

~~The recordings of the thermistors demonstrate that the surficial rock layer (< 1 m) thaws during the summer months. This is valid for both slope faces of the summit ridge (Fig. S7).~~



250 **Figure S7S4:** Near-surface rock temperatures measured in a depth of 10-80 cm at the Zugspitze summit crest between 08/2015 and 08/2019: (a) north-face, (b) south-face.

## 6 Rock-mechanical laboratory tests

### 6.1 Intact rock

#### 255 6.1.1 Preparation of the rock samples

The rock samples for the laboratory tests were cored from Wetterstein limestone blocks with a mean side length of  $0.4 \pm 0.1$  m that were picked from the study site (Fig. 2) and the lower Zugspitzplatt (2590 m a.s.l.; Fig. 1a). Uniaxial compression and

Brazil tests were conducted in accordance with the recommendations of the Commission on Rock Testing of the German Geotechnical Society (Lepique, 2008; Mutschler, 2004). Ultrasonic tests were performed in accordance with the norm on Non-destructive testing of the European Committee for Standardization (DIN EN ISO 16810, 2014). The rock cores of  $51 \pm 0.1$  mm diameter were cut with a diamond saw into  $103 \pm 1$  mm thick cylinders for the uniaxial compression and ultrasonic tests and into  $25 \pm 1$  mm thick discs for the Brazil tests. The high structural isotropy of the Wetterstein limestone allowed us to ignore any specific drilling orientation dependent on bedding or foliation.

~~As we assume the rock mass of a real-world rock slope to be close to a saturated state. Therefore usually saturated, we tested the rock samples in a frozen saturated and unfrozen rock samples were tested saturated condition close to a saturated state. For this full saturation, rock samples they were kept in a water bath for at least 48 h (DIN EN ISO 13755, 2002). The samples were regarded as nearly saturated when successive mass determinations yielded values varying less than 0.1 %. The rock specimens were tested under saturated unfrozen and saturated frozen conditions. Frozen conditions were provided achieved by freezing saturated rock cores at  $-28$  °C in a cooling box for at least 48 h. For full saturation, rock samples were kept in a water bath for at least 48 h (DIN EN ISO 13755, 2002). The samples were regarded as nearly saturated when successive mass determinations yielded values varying less than 0.1 %.~~

~~A natural rock slope is expected to be nearly water-saturated for the following reasons: (i) While near surface rock saturation fluctuates highly due to meteorological influences like precipitation, wind or insulation, the rock moisture in depths greater than 15 cm remains unchanged; here, it ranges between approximately 75 and 90 % dependent on the rock type and its porosity (Rode et al., 2016; Sass, 2005). (ii) The successful application of ER surveying in permafrost bedrock in the presented study (Section 2.1.3) and in many others confirm that the investigated rock slopes are saturated, since this technique only works well in saturated rock: (a) In rocks with a high degree of water saturation, electric current can be propagated due to electrolytic conduction. The DC conductivity of porous or fractured subsurface matter highly depends on saturation of the pore space and conductivity of the pore fluid (Supper et al., 2014; Telford et al., 1990). (b) The detected large ranges in electrical resistivity indicate a high degree of water saturation, since only water-saturated rocks can show a significant difference in conductivity/electrical resistivity when switching from the unfrozen to the frozen state, or vice versa (e.g. Mellor, 1973). Accordingly, water-saturated rock samples are recommended to be used for the laboratory calibration of the electrical resistivity of frozen and unfrozen rock for ERT in rock walls (Krautblatter et al., 2010).~~

~~The rock specimens were tested under saturated unfrozen and saturated frozen conditions. Frozen conditions were provided by freezing saturated rock cores at  $-28$  °C in a cooling box for at least 48 h. For full saturation, rock samples were kept in a water bath for at least 48 h (DIN EN ISO 13755, 2002). The samples were regarded as nearly saturated when successive mass determinations yielded values varying less than 0.1 %. As we assume the rock mass of a real world rock slope to be usually saturated, the frozen and unfrozen rock samples were tested close to a saturated state. However, previous laboratory studies by Inada and Yokota (1984), Kodama et al. (2013), Mellor (1973) and others have demonstrated that the uniaxial compressive and the tensile strength of frozen and unfrozen intact rock depend on the saturation degree of the rock. According to the mentioned publications, a higher saturation degree in frozen samples can increase strength due to enhanced ice adhesion or a~~

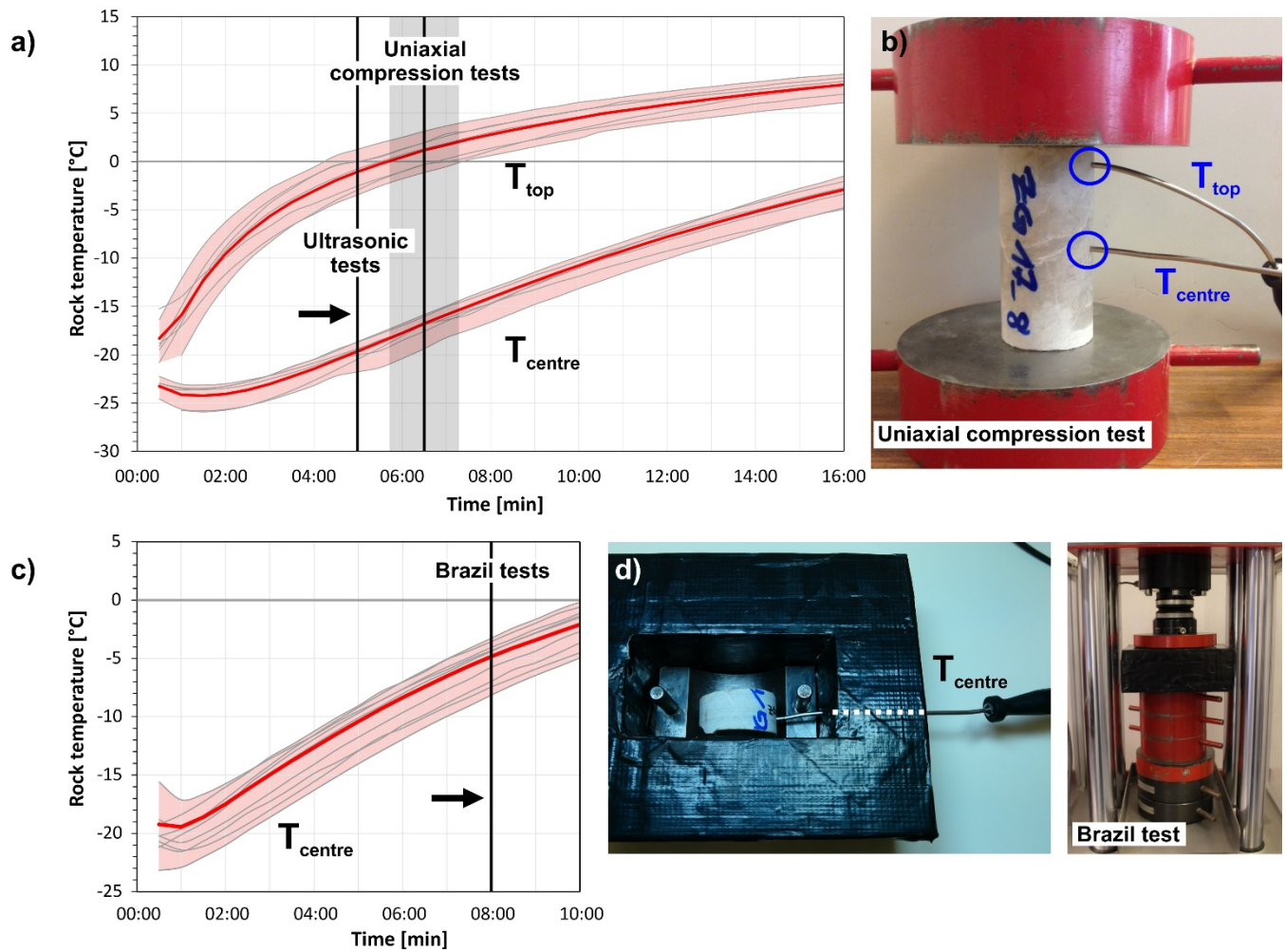
~~reduced stress concentration in ice-plugged pores within the rock. On the other hand, a higher saturation degree in frozen samples can reduce strength due to promoted micro-cracking caused by volume expansion of the ice. These phenomena may be more pronounced in rocks with high porosity, but less important for the tested limestone with a porosity of  $0.9 \pm 0.4\%$ .~~

## 295 6.1.2 Test setups

As the testing instruments were not located in a cooled room, the frozen rock samples warmed during the tests. However, for determination of frozen mechanical properties, the rock specimens had to remain frozen during the whole experiments. Thus, the rock discs during Brazil tests were isolated with a polystyrene box which did not affect the progress of the tests (Fig. S58d). Isolation of the rock cylinders could not be realised as the box would prevent the measurement of axial and diametric strain during uniaxial compression and the measurement of dilatational waves during ultrasonic testing.

300 Hence, we additionally simulated a series of pretests to carefully observe the warming behaviour of dummy rock samples during typical uniaxial compression and Brazilian tests. The warming of rock cylinders during ultrasonic testing was assumed to behave in the same way as in uniaxial compression. As a result, the pretests of the latter were taken as representative for warming during ultrasonic tests. Warming was monitored by Pt100 temperature sensors (Greisinger GMH3750, with a 0.03 °C precision) inserted in the centre and close to the end of the rock sample (Fig. S58b and Fig. S58d). A pretest consisted in fitting the dummy sample into the apparatus and monitor the progress of warming inside the rock specimens until they were thawed. A negligible load was applied to the samples to prevent the destruction of the thermistors or a potential weakening of the sample due to the drilled holes.





310

Figure S8S5: (a) Warming pattern for frozen dummy rock cylinders with two thermistors during simulated uniaxial compression testing. (b) Rock cylinder mounted between loading plates that are used in a typical uniaxial compression test. (c) Warming curves for frozen dummy rock discs with one central thermistor during simulated Brazil tests. (d) Isolation of a rock disc during pretests with temperature logging (left) and a typical Brazil test (right). Black lines = Maximum duration of mechanical tests. Black line with grey area = Mean duration of compression tests with standard deviation. Red thick line = Mean rock temperature during pretests. Red area = Range of variation of warming curves during pretests.

315

### 6.1.3 Testing conditions

Overall, we performed 28 uniaxial compression tests (14 unfrozen, 14 frozen), 60 Brazil tests (30 unfrozen, 30 frozen), 60 ultrasonic tests (30 unfrozen, 30 frozen) and 90 density tests (60 with the discs and 30 with the cylinders):

320



- Uniaxial compression tests were performed to provide data on the uniaxial compressive stress at failure. Tests were run with a ToniNorm compression testing machine (DIN EN ISO 7500-1, 2018). A constant strain of 0.6 mm / (m \* min) was applied to the samples provoking failure within 8 min.

- Brazil tests were conducted to collect data on the indirect tensile stress at failure which is the tensile stress normal to the uniaxially loaded areas of the specimen. A ToniNorm tension testing machine according to the (DIN EN ISO 7500-1, 2018) was used to apply a load at a constant rate of 70 N/s, leading to failure within 6 min.

- Ultrasonic tests were run to determine the velocity of the dilatational wave propagating through the specimen. The apparatus consisted of a signal generator USG40, a transmitter type UPG 250, a receiver type UPE and a preamplifier VV41 by Geotron Electronics. The rock samples were fixed between the piezoelectric transducer pair at the centres of the flat contact surfaces. Any water film at the contact surfaces of the rock cylinders was removed before testing with an absorbent cloth. Measurements were run with a frequency of 20kHz.

- The rock density  $\rho$  was defined due to weighing in an immersion bath following the standard procedure of the (DIN EN ISO 1097-6, 2005).

The test durations, provided by the black lines in Fig. S58a and Fig. S58c, also include the mounting of the samples into the apparatus: uniaxial compression tests had a mean duration of  $6.5 \pm 0.8$  min, while Brazil tests and ultrasonic tests did not exceed 8 and 5 min, respectively. Hereafter, rock temperatures in the centre of the samples lay below  $-5$  °C during Brazil tests, below  $-15$  °C during uniaxial compression tests and below  $-20$  °C during ultrasonic tests. As such, we could guarantee frozen conditions for the Brazil and the ultrasonic tests, while the major central part of the cylinders in the uniaxial compression tests were frozen, too. Unfrozen mechanical properties were studied at room temperature.

~~Uniaxial compression tests were performed to provide data on the uniaxial compressive stress at failure. Tests were run with a ToniNorm compression testing machine (DIN EN ISO 7500-1, 2018). A constant strain of 0.6 mm / (m \* min) was applied to the samples provoking failure within 8 min.~~

~~Brazil tests were conducted to collect data on the indirect tensile stress at failure which is the tensile stress normal to the uniaxially loaded areas of the specimen. A ToniNorm tension testing machine according to the (DIN EN ISO 7500-1, 2018) was used to apply a load at a constant rate of 70 N/s, leading to failure within 6 min.~~

~~Ultrasonic tests were run to determine the velocity of the dilatational wave propagating through the specimen. The apparatus consisted of a signal generator USG40, a transmitter type UPG 250, a receiver type UPE and a preamplifier VV41 by Geotron Electronics. The rock samples were fixed between the piezoelectric transducer pair at the centres of the flat contact surfaces. Any water film at the contact surfaces of the rock cylinders was removed before testing with an absorbent cloth. Measurements were run with a frequency of 20kHz.~~

~~The rock density  $\rho$  was defined due to weighing in an immersion bath following the standard procedure of the (DIN EN ISO 4097-6, 2005).~~

## 6.2 Rock joints

The residual friction angle  $\phi_r$  was estimated according to (Barton and Choubey, 1977), using the basic friction angle  $\phi_b$  as well as the Schmidt hammer rebound hardness  $R$  and  $r$  for unweathered, sawn surfaces and weathered surfaces, respectively.

### 6.2.1 Preparation of the rock samples

360 For the basic friction angle of the rock joints, we performed tilt tests with unweathered sawn rock surfaces of frozen and unfrozen Wetterstein limestone following the procedure suggested by Barton and Choubey (1977) and Barton (2013). For the Schmidt hammer rebound hardnesses  $R$  and  $r$ , we conducted a series of Schmidt hammer tests in the laboratory with dry unweathered sawn and wet weathered rock surfaces of frozen and unfrozen Wetterstein limestone. The tests were prepared and realised following the proposed procedure of the International Society for Rock Mechanics (ISRM; Ulusay, 2015) and  
365 Aydin et al. (2005).

The rock samples were cored from Wetterstein limestone blocks with a mean side length of  $0.4 \pm 0.1$  m that were picked from the study site (Fig. 12) or the lower Zugspitzplatt (2590 m a.s.l.). The rock cores were cut with a diamond saw into 10 cylinders for the tilt tests, while two of them were taken for testing the Schmidt hammer rebound hardness  $R$ . The samples for the tilt tests had a mean height of  $83.1 \pm 2.6$  mm and the samples for the Schmidt hammer tests on unweathered joint surfaces had a  
370 mean height of 84.1 mm. The corresponding mean diameters ranged between  $148.5 \pm 0.2$  and 148.6 mm, respectively. The wet weathered joint surfaces (for determining  $r$ ) were tested at a single Wetterstein limestone block with a volume of  $0.02 \text{ m}^3$ , collected from the Zugspitze summit ridge.

### 6.2.2 Test setups and procedures

Unfrozen conditions corresponded to ambient room temperature. Frozen conditions for the tilt tests and the Schmidt hammer tests on unweathered joint surfaces were achieved by storing the rock specimens in a cooling box at  $-28 \text{ }^\circ\text{C}$  for 48 h. The bigger  
375 block for the Schmidt hammer tests on wet weathered joint surfaces were stored for 48 h in a bigger, self-constructed and isolated cooling box at  $-10 \text{ }^\circ\text{C}$ . The samples were tested directly after taking them out of the cooling box. As the experiments did not exceed 2-4 min, we could guarantee the rock samples to be frozen during the tests. Isolation of the specimens during the tests was technically not feasible. Any ice layer that could have developed at the rock surfaces during freezing was carefully  
380 removed before testing to prevent a potential influence on the results.

According to the ISRM (Ulusay, 2015), samples for Schmidt hammer tests have to be firmly fixed to a heavy steel base or a firm and flat ground to avoid a potential loss of impact energy. The big rock block was too heavy to move during the tests. However, the smaller and lighter rock cylinders (for determining  $R$ ) were mounted with their flat ends between two load platens

of a ToniNorm uniaxial compression machine (with a maximum applicable load of 250 kN). After that, the samples were  
385 firmly fixed by applying an axial load of 60 N.

A Schmidt hammer of the N-type was used for testing the rebound hardness. For the unweathered surfaces, the impacts by the  
plunger tip of the hammer were applied to the rounded smooth sides of the cylinders. The impacts were distributed along the  
cylinder sides by rotating it on the flat ends in steps of 90°. The weathered surface of the bigger rock block was sampled on  
two faces of the specimen. We collected at least 20 impact readings per specimen and averaged the upper 50 %. Rebound  
390 values collected in down- or upward direction were normalised in accordance with the ISRM standard (Ulusay, 2015).

The weathered surface of the rock block was characterised by a higher roughness and small asperities which got partly  
destroyed by the hammer impacts. This led to a higher variation in the data.

## 7 Numerical stability analysis ~~for a simplified permafrost rock slope with rising temperature~~

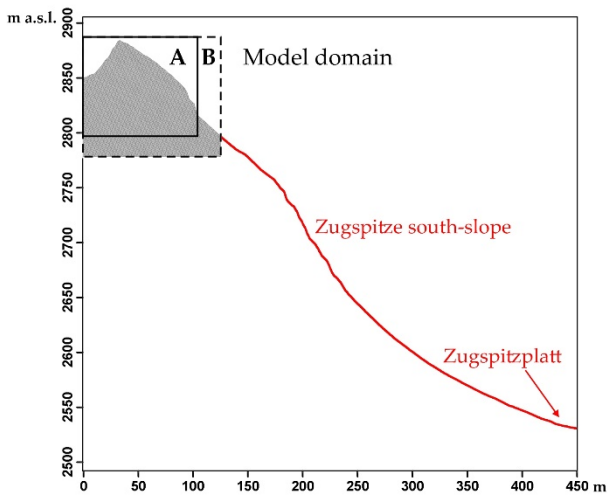
### 7.1 Further assumptions for the procedure of the numerical analysis

395 The general modelling procedure consists of four steps: the calculation of an initial equilibrium and three successive steps of  
potential destabilisation which include the progressive destruction of intact rock bridges, the warming and the thawing of a  
permafrost rock slope. The past destruction of cohesive intact rock bridges was simulated by a reduction of the apparent joint  
cohesion and friction angle in three steps which represents a progressive increase of the joint persistence from 30 to 90 %  
(Stages 1–4 in Table 6, Table 7). This procedure simulates “step-path” failure on the slope scale in a simplified way which is  
400 characterised by the interconnection of pre-existing, adjacent discontinuities through intact rock bridges (Eberhardt et al., 2004;  
Huang et al., 2015; Mejía Camones et al., 2013). The reduction in the shear strength involves processes of stress concentration,  
crack initiation, crack propagation and coalescence, slip weakening and the formation of a continuous failure plane or zone  
(Zhang et al., 2015), which were not numerically modelled as this would be beyond the scope of this study. The presented  
model of the Zugspitze ridge considers crack coalescence to occur by shear and tensile mode or a tensile-shear combination,  
405 which has been observed on the micro-scale by Zhang and Wong (2013). The resulting new connections can form coplanar or  
oblique to the pre-existing joints (Huang et al., 2015). At the scale of the Zugspitze ridge, we assume the joint sets K1, K3 and  
K4 to link in both coplanar and oblique form, leading to the formation of straight or stepped failure planes.

### 7.2 Additional sensitivity analyses of the numerical models

To analyse the influence of a higher disturbance factor  $D$  on the stability of the Zugspitze summit crest,  $D$  was changed to a  
410 maximum of 1. Accordingly, the mechanical parameters  $G$ ,  $K$ ,  $\sigma_{jm}$ ,  $k_n$  and  $k_s$  reduced by a mean of 56 %. While the model  
results showed higher displacements, the factor of safety remained unchanged (Fig. S6). Further, we extended the model  
domain by 20 m to the right/south and by 20 m downward to test if the model results are affected by a bigger model domain  
which ends in a flatter slope (Domain B in Fig. S6). Again, the model results demonstrated that the overall stability of the  
slope does not change, although the displacements are higher by a factor of 1 to 3.

415



		Principal modelling steps	Initial state	Progressive destruction of rock bridges				Stepwise warming from surface to core				
		Model stage number	1	2	3	4	5	6	7	8	9	
Max displ. [mm]	Model domain size	A (D = 0)	7,6	7,8	7,8	7,7	7,7	7,7	7,8	7,9	8,2	
	Disturbance factor	B	23,8	24,0	24,0	26,1	26,2	26,2	26,1	26,2	27,3	
		D = 1	18,2	19,5	19,5	19,4	19,4	19,5	17,9	18,9	19,1	
FoS	Model domain size	A (D = 0)	10,9			2,6	3,4				1,3	
	Disturbance factor	B	9,1		4,6	2,2	2,8				1,1	
		D = 1	10,7			2,6	3,4				1,3	

		Principal modelling steps	Stepwise thawing from surface to core					All unfrozen
		Model stage number	10	11	12	13	14	15
Max displ. [mm]	Model domain size	A (D = 0)	141,1	419,5	520,4	616,8	689,7	776,3
	Disturbance factor	B	107,3	316,7	671,0	1066,4	1192,0	1226,4
		D = 1	273,2	782,3	1085,0	1232,7	1327,0	1407,7
FoS	Model domain size	A (D = 0)	0,6	0,6				0,6
	Disturbance factor	B	0,5	0,6				0,7
		D = 1	0,6	0,7				0,7

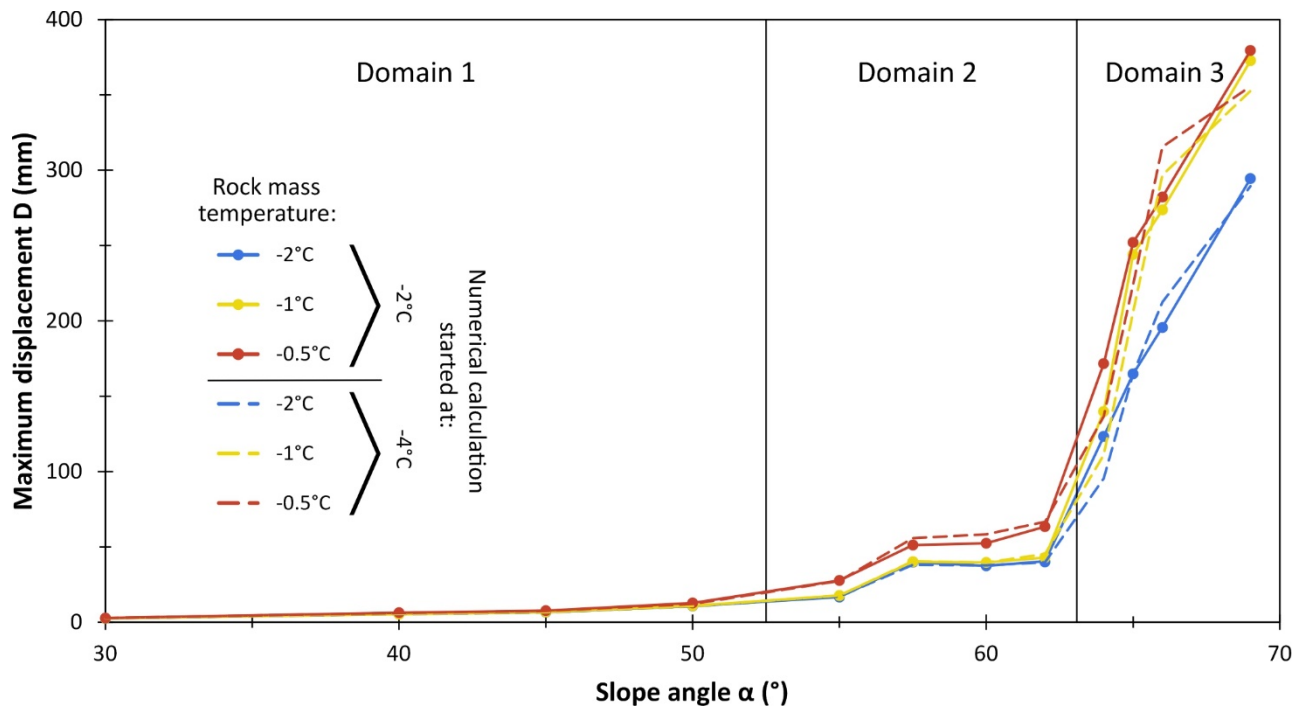
**Figure S6: Influence of a bigger model domain and a higher disturbance factor D on the slope stability. Model domain A and D = 0 were used for the original Zugspitze model (Section 2). The topography of the Zugspitze (red line) was extracted from a digital elevation model in ArcGIS.**

420

All numerical stability analyses for progressive warming were started with a frozen rock slope at a temperature of  $-4\text{ }^{\circ}\text{C}$ . The stability calculations of the universal model were additionally run with a start temperature of  $-2\text{ }^{\circ}\text{C}$  to be able to estimate the effect of a higher start temperature on the model results as material parameters with a lower strength have been assigned for the calculation of the initial equilibrium.

425

However, the additional model runs led to similar displacement magnitudes as for a modelling start at  $-4\text{ }^{\circ}\text{C}$  (Fig. S79): the slope-dependent pattern is generally the same with two onsets of initiating instability at slope gradients of above  $50$  or  $55^{\circ}$  (transition to Domain 2) and a slope gradient above  $62^{\circ}$  (transition to Domain 3).



430 **Figure S9S7:** Maximum block and zone model displacements versus slope gradient for a permafrost rock slope at -2, -1 and -0.5 °C. Solid lines with circles represent numerical results of calculations started at -2 °C, while dashed lines represent numerical results of calculations started at -4 °C (according to Fig. 8). The three domains relate to a distinct displacement behaviour and are in accordance with the domains presented in Fig. 8a.

435 The progressive warming steps for the universal rock slope were remodeled with twice the amount of cycles to assess the effect of longer numerical computation on the mechanical response of the system. Overall, the slope-dependent pattern remains generally the same with two onsets of initiating slope instability at 50 and at 62° (Fig. S8+0). For warming steps between -4 and -2 °C the rock slope responded similar to the previous calculations with 3000 cycles (dashed lines). However, a warming to -1 or -0.5 °C in rock slopes with an inclination of higher than 60° resulted in displacements 10–111 % higher than in the  
 440 model runs with 3000 cycles. However, the displacements remained within the same order of magnitude.

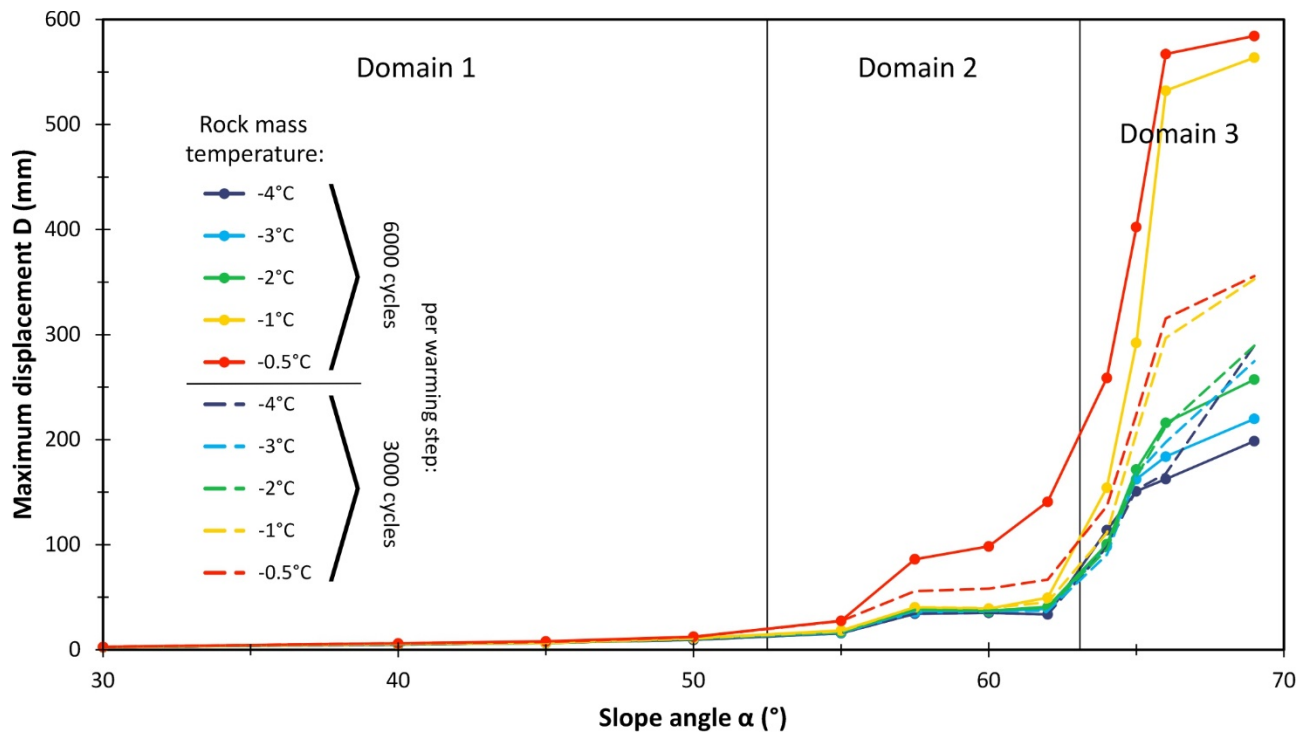


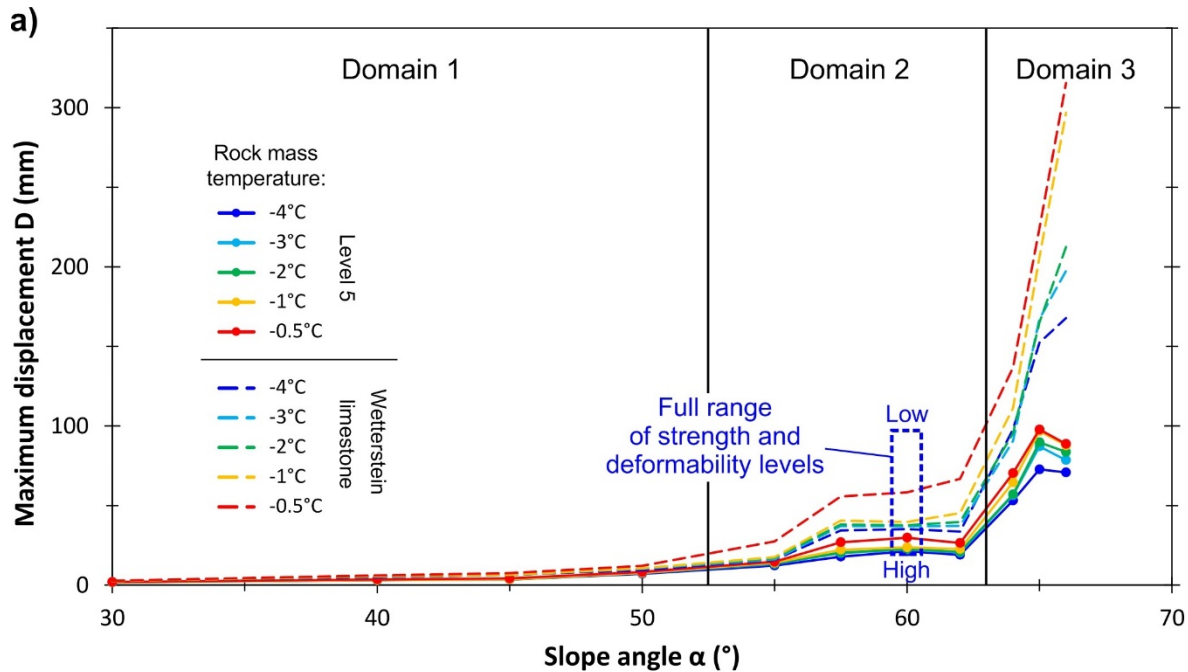
Figure S810: Maximum displacements against slope angle for a permafrost rock slope at temperatures between -4 and -0.5 °C. Dashed lines represent warming steps with 3000 cycles (according to Fig. 8), while solid lines with circles represent warming steps with the twofold amount of numerical cycles (6000). The three domains relate to a distinct displacement behaviour and are in accordance with the domains presented in Fig. 8a.

The results of the sensitivity analysis with input data from the Zugspitze summit ridge (Sect. 4.2) are valid for warming permafrost rock slopes which consist of limestone, with strength and deformability similar to the Wetterstein limestone tested in this study. A transfer to permafrost rock slopes with a different lithology requires more modelling, as the mechanical parameters of the rock mass vary among different rock types and may lead to different model results. To get an impression of this effect, we performed a couple of model test runs with varying values of the mechanical rock mass properties ranging from very low to unrealistically high. However, the selected range of the implemented mechanical properties also covers typical values of a wide range of different rock types (Clauser and Huenges, 1995; Kulatilake et al., 1992; Schön, 2015). We defined four fictitious levels of rock mass strength and deformability which are lower than the one of the Wetterstein limestone used for the simplified model (Sect. 4.2), and six fictitious levels which are higher (Fig. S911b). Modelling was performed for a rock slope with an inclination of 60° and a mean temperature of -4 °C. In a second step, we examined the pattern of displacements over the full range of slope gradients (30-66°) and temperatures (-0.5 to -4 °C) of the simplified model using a further specific level of high strength (Level 5) for a new set of model runs (Fig. S911a).

The results of the analysis showed that the displacements mostly remained within the same order of magnitude (Fig. S9a). This is valid for the model runs with (i) varying strength and deformability at a slope angle of 60° and a temperature of -4 °C (results



lie within the dashed blue box), and (ii) the specific strength and deformability level 5 over the entire range of slope angles and temperatures of the simplified model.



**b)**

	Strength and deformability level of the rock mass		Mechanical parameter				
	$\rho$ [g/cm <sup>3</sup> ]	$K_m$ [GPa]	$G_m$ [GPa]	$c_m$ [MPa]	$\sigma_{tm}$ [MPa]	$\phi_m$ [°]	
Low	-4	2,4	2,5	1,25	0,5	0,125	20
	-3	2,5	5	2,5	1	0,25	30
	-2	2,6	10	5	2	0,5	36
	-1	2,7	15	7,5	3	0,75	42
	0 (Wetterstein limestone: model)	2,7	20,6	9,52	4	0,9	44
	1	2,7	30	14	6	1,5	46
	2	2,7	41	19	8	2	46
	3	2,8	82	38	16	4	49
	4	2,9	164	76	32	8	52
	5 (used for model runs at temperatures from -4 to -0.5°C and slope angles from 30 to 66°)	2,7	200	90	40	9	55
	6	3,0	328	152	64	16	55
High	7	3,1	656	304	128	32	59

465

**Figure S911:** (a) Maximum block and zone model displacements versus slope angle for different fictitious levels of rock mass strength and deformability and for temperatures between -4 and -0.5 °C. Dashed lines represent calculations with Wetterstein limestone (according to Fig. 8), while solid lines with circles represent calculations with a rock type that has a strength and deformability one order of magnitude higher. The dashed blue box defines the range of displacements for all rock mass levels presented in (b), at -4 °C and for a slope gradient of 60°. (b) Mechanical parameters for the distinct rock masses with varying strength and deformability.

470

The results of the analysis showed that the displacements mostly remained within the same order of magnitude (Fig. S11a). This is valid for the model runs with (i) varying strength and deformability at a slope angle of 60° and a temperature of 4 °C (results lie within the dashed blue box), and (ii) the specific strength and deformability level 5 over the entire range of slope angles and temperatures of the simplified model.

475

## References

- Aydin, A., and Basu, A.: The Schmidt hammer in rock material characterization, *Eng. Geol.*, 81, 1–14, 2005.
- Barton, N. R.: Shear strength criteria for rock, rock joints, rockfill and rock masses: Problems and some solutions, *J. Rock Mech. Geotech. Eng.*, 5, 249–261, <https://doi.org/10.1016/j.jrmge.2013.05.008>, 2013.
- 480 Barton, N. R. and Choubey, V.: The shear strength of rock joints in theory and practice, *Rock Mech.*, 10, 1–54, 1977.
- Clauser, C. and Huenges, E.: Thermal conductivity of rocks and minerals, in: *Rock Physics & Phase Relations: A Handbook of Physical Constants*, American Geophysical Union, Washington, D. C., 105–126, 1995.
- DIN EN ISO 1097-6: Tests for mechanical and physical properties of aggregates - Part 6: Determination of particle density and water absorption; German version EN 1097-6:2000, 91.100.15, Beuth Verlag GmbH, Berlin, 2005.
- 485 DIN EN ISO 13755: Natural stone test methods - Determination of water absorption at atmospheric pressure; German version EN 13755: 2001, 73.020, Beuth Verlag GmbH, Berlin, 2002.
- DIN EN ISO 16810: Non-destructive testing - Ultrasonic testing - General principles (ISO 16810: 2012); German version EN ISO 16810: 2014, 19.100, Beuth Verlag GmbH, Berlin, 2014.
- 490 DIN EN ISO 7500-1: Metallic materials - Calibration and verification of static uniaxial testing machines - Part 1: Tension/compression testing machines - Calibration and verification of the force-measuring system, Beuth Verlag GmbH, Berlin, 2018.
- Eberhardt, E., Stead, D. and Coggan, J. S.: Numerical analysis of initiation and progressive failure in natural rock slopes—the 1991 Randa rockslide. *Int. J. Rock Mech. Min.*, 41, 69–87, [https://doi.org/10.1016/S1365-1609\(03\)00076-5](https://doi.org/10.1016/S1365-1609(03)00076-5), 2004.
- 495 Gubler, S., Fiddes, J., Keller, M. and Gruber, S.: Scale-dependent measurement and analysis of ground surface temperature variability in alpine terrain, *The Cryosphere*, 5, 431–443, <https://doi.org/10.5194/tc-5-431-2011>, 2011.
- Huang, D., Cen, D., Ma, G. and Huang, R.: Step-path failure of rock slopes with intermittent joints, *Landslides*, 12, 911–926, <https://doi.org/10.1007/s10346-014-0517-6>, 2015.
- Inada, Y. and Yokota, K.: Some studies of low temperature rock strength, *Int. J. Rock Mech. Min.*, 21, 145–153, [https://doi.org/10.1016/0148-9062\(84\)91532-8](https://doi.org/10.1016/0148-9062(84)91532-8), 1984.
- 500 Keuschnig, M.: Long-term monitoring of permafrost-affected rock walls. Towards an automatic, continuous electrical resistivity tomography (AERT) monitoring for early warning systems, Dissertation, Technical University of Munich, Munich, 2016.

- 505 [Kodama, J., Goto, T., Fujii, Y. and Hagan P.: The effects of water content, temperature and loading rate on strength and failure process of frozen rocks, \*Int. J. Rock Mech. Min.\*, 62, 1–13, 2013.](#)
- Krautblatter, M., Verleysdonk, S., Flores-Orozco, A. and Kemna, A.: Temperature-calibrated imaging of seasonal changes in permafrost rock walls by quantitative electrical resistivity tomography (Zugspitze, German/Austrian Alps), *J. Geophys. Res. - Earth Surface*, 115, 1–15, 2010.
- 510 Kulatilake, P. H. S. W., Ucpirti, H., Wang, S., Radberg, G. and Stephansson, O.: Use of the distinct element method to perform stress analysis in rock with non-persistent joints and to study the effect of joint geometry parameters on the strength and deformability of rock masses, *Rock Mech. Rock Eng.*, 25, 253–274, <https://doi.org/10.1007/BF01041807>, 1992.
- Lepique, M.: Empfehlung Nr. 10 des Arbeitskreises 3.3 “Versuchstechnik Fels” der Deutschen Gesellschaft für Geotechnik e. V. Indirekter Zugversuch an Gesteinsproben – Spaltzugversuch, *Bautechnik*, 85, 623–627, <https://doi.org/10.1002/bate.200810048>, 2008.
- 515 Loke, M. H.: Res2Dinv. Geoelectrical Imaging 2D & 3D, Geotomo Software Sdn Bhd, 2019.
- [Mejía Camones, L. A., Vargas, E. d. A., Figueiredo, R. P. de and Velloso, R. Q.: Application of the discrete element method for modeling of rock crack propagation and coalescence in the step-path failure mechanism, \*Eng. Geol.\*, 153, 80–94, <https://doi.org/10.1016/j.enggeo.2012.11.013>, 2013.](#)
- 520 Mellor, M.: Mechanical properties of rocks at low temperatures, 2nd International Conference on Permafrost, Yakutsk, Siberia, 13-28 July 1973, 1973.
- Mutschler, T.: Neufassung der Empfehlung Nr. 1 des Arbeitskreises “Versuchstechnik Fels” der Deutschen Gesellschaft für Geotechnik e. V. Einaxiale Druckversuche an zylindrischen Gesteinsprüfkörpern, *Bautechnik*, 81, 825–834, <https://doi.org/10.1002/bate.200490194>, 2004.
- 525 [Rode, M., Schnepfleitner, H. and Sass, O.: Simulation of moisture content in alpine rockwalls during freeze–thaw events, \*Earth Surf. Proc. Land.\*, 41, 13, 1937–1950, <https://doi.org/10.1002/esp.3961>, 2016.](#)
- Schön, J. H.: Physical properties of rocks. Fundamentals and principles of petrophysics, Elsevier, 2015.
- [Sass, O.: Rock moisture measurements. Techniques, results, and implications for weathering, \*Earth Surf. Proc. Land.\*, 30, 3, 359–374, <https://doi.org/10.1002/esp.1214>, 2005.](#)
- 530 [Supper, R., Ottowitz, D., Jochum, B., Römer, A., Pfeiler, S., Kauer, S., Keuschnig, M. and Ita, A.: Geoelectrical monitoring of frozen ground and permafrost in alpine areas. Field studies and considerations towards an improved measuring technology, \*Near Surface Geophysics\*, 12, 93–115, <https://doi.org/10.3997/1873-0604.2013057>, 2014.](#)
- [Telford, W. M., Geldart, L. P. and Sheriff, R. E.: Applied Geophysics, Second Edition, Cambridge University Press, Cambridge, 1990.](#)
- 535 Tse, R. and Cruden, D. M.: Estimating joint roughness coefficients, *Int. J. Rock Mech. Min.*, 16, 303–307, [https://doi.org/10.1016/0148-9062\(79\)90241-9](https://doi.org/10.1016/0148-9062(79)90241-9), 1979.
- Ulusay, R.: The ISRM Suggested Methods for Rock Characterization, Testing and Monitoring: 2007-2014, Springer International Publishing, 2015.

Yang, Z. Y., Lo, S. C. and Di, C. C.: Reassessing the Joint Roughness Coefficient (JRC) Estimation Using Z2, *Rock Mech. Rock Eng.*, 34, 243–251, <https://doi.org/10.1007/s006030170012>, 2001.

540 [Zhang, X.-P. and Wong, L. Ngai Yuen: Crack Initiation, Propagation and Coalescence in Rock-Like Material Containing Two Flaws. A Numerical Study Based on Bonded-Particle Model Approach, \*Rock Mech. Rock Eng.\*, 46, 1001–1021, <https://doi.org/10.1007/s00603-012-0323-1>, 2013.](#)

545 [Zhang, K., Cao, P., Meng, J., Li, K. and Fan, W.: Modeling the Progressive Failure of Jointed Rock Slope Using Fracture Mechanics and the Strength Reduction Method, \*Rock Mech. Rock Eng.\*, 48, 771–785, <https://doi.org/10.1007/s00603-014-0605-x>, 2015.](#)